LA-UR-16-25834
Approved for public release; distribution is unlimited.

Title: Experimental studies of engineering barrier systems conducted at Los Alamos National Laboratory (FY16)

Author(s): Caporuscio, Florie Andre
Norskog, Katherine Elizabeth
Maner, James
Palaich, Sarah
Cheshire, Michael

Intended for: Report

Issued: 2016-09-12 (rev.1)

Experimental studies of Engineered Barrier Systems conducted at Los Alamos National Laboratory (FY16)

Fuel Cycle Technology

Prepared for
U.S. Department of Energy
Used Fuel Campaign
Caporuscio, F.A.
Norskog, K.E.
Maner, J.
Palaich, S.
Cheshire, C.
Los Alamos National Laboratory

July 29, 2016
FCRD-UFD-2016-000620
'LA-UR-16-25834'

SUMMARY

Over the past five years the Used Fuel Campaign has investigated Engineered Barrier Systems (EBS) at higher heat loads (up to 300℃) and pressure (150 bar). This past year experimental work was hindered due to a revamping of the hydrothermal lab. Regardless, two experiments were run this past year, EBS-18 and EBS-19. EBS-18 was run using Low Carbon Steel (LCS) and opalinus clay in addition to the bentonite and opalinus brine. Many of the past results were confirmed in EBS-18 such as the restriction of illite formation due to the bulk chemistry, pyrite degradation, and zeolite formation dependent on the bentonite and opalinus clay. The LCS show vast amounts of pit corrosion over 100µm of corrosion in six weeks, leading a corrosion rate of 1083 µm/year. In addition, a mineral goethite, an iron bearing hydroxide, formed in the pits of the LCS. Preliminary results from EBS-19 water chemistry are included but SEM imaging, micro probe and XRD are still needed for further results. Copper corrosion was investigated further and over 850 measurements were taken. It was concluded that pitting and pyrite degradation drastically increase the corrosion rate from 0.12 to 0.39 µm/day. However, the growth of a layer of the mineral chalcocite is thought to subdue the corrosion rate to 0.024 µm/day as observed in the EBS-13 a sixth month experiment. This document presents the findings of this past year.

CONTENTS

APPENDIX

FIGURES

TABLES

ACRONYMS

EBS – Engineered Barrier Systems
EDX – energy dispersive X-ray
EH potential – oxidation reduction potential
EMP - electron microprobe
FY – fiscal year
IAEA – International Atomic Energy Association
IC - ion chromatography
I-S - illite-smectite
LCS – Low Carbon Steel
MPa – Mega Pascal
QXRD- Quantitative X-ray diffraction
SEM - scanning electron microscope
SS – Stainless Steel
TEM – transmission electron microscope
XRD - X-ray diffraction
XRF - X-ray florescence

TITLE

1. INTRODUCTION

The U.S. Department of Energy has designed the Used Fuel Disposition Campaign to investigate the design and safety function of generic nuclear geologic repositories in a variety of geologic settings. The evaluation of engineered barrier system (EBS) concepts and interaction with the wall rock (i.e., natural barriers), waste canisters, or other EBS interfaces are important to the long term performance and safety of geologic repositories (Nutt et al., 2011, Jove-Colon et al., 2011). The European community, especially the French, have investigated bentonite stability in contact with steel under a variety of experimental conditions in an attempt to replicate repository conditions (Pusch 1979; Madsen 1998; Meunier et al. 1998; Guillaume et al. 2003; Wersin et al. 2007; Mosser-Ruck et al. 2010; Ferrage et al. 2011). The majority of their research was focused on lower temperature environments and atmospheric pressures. Our experimental program for FY16 aims to characterize how EBS components react and change in the presence of Opalinus Clay at reasonable high temperature (300 ^{o}C, 150 Bar) in-situ repository conditions.

1.1 BACKGROUND

One of the more accepted ideas for high-level nuclear waste disposal is to emplace the steel waste canister in a geological repository with a bentonite barrier between the canister and host rock (Pusch 1979; Meunier et al. 1998). Bentonite is used to provide 1) a physical barrier to prevent fluid seeping in from natural surroundings and interacting with the waste package, 2) a chemical barrier by attenuating actinide migration if a release occurs. Furthermore, the bentonite's swelling capacity has the capability of self-sealing if cracks develop within the bentonite due to shrink-swell phenomena. However, there remain large uncertainties regarding the long-term stability of bentonite at potential repository conditions, particularly, under prolonged periods of high thermal loads. There have been numerous investigations on the stability of bentonites under various repository conditions and in contact with various metals replicating possible canister compositions (Pusch 1979; Madsen 1998; Meunier et al. 1998; Guillaume et al. 2003; Wersin et al. 2007; Mosser-Ruck et al. 2010; Ferrage et al. 2011).

This report summarizes the various authigenic minerals occurring within hydrothermal experiments replicating a high temperature repository environment. The emphasis is on; 1)

Opalinus wall rock interactions with EBS backfill, 2) copper alteration and corrosion rates, and 3) steel/ bentonite interface phase reactions. The intent of Section 1 will examine various reactions that include unprocessed Wyoming bentonite, the clay/metal interface, and the metal/clay/host rock components. Much of the characterization and discussion on the early EBS (1-12) results have been published in Cheshire et al. (2013; 2014). Characterization of both the pre-run materials and post experiment phases of experiments EBS-1 through -17 were discussed in Caporuscio, et al. (2015) to better describe the processes that progress during the hydrothermal reactions. In addition to expanded analyses of the earlier reactions, experiments on host-rock (Opalinus Clay) interaction were conducted to further our understanding of this complex system. Those experimental starting materials are shown in Table 1 The initial Opalinus clay synthetic groundwater depicted in Table 2.

Table 1 Initial components and reaction conditions for EBS experiments in the presence of Opalinus Clay.

Experiment	Clay, g	Brine, g	EBS Component	Run temp, °C	Run time
OPALINUS CLAY EXPERIMENTS					
EBS-14	14.86	128.1	**Opalinus Clay**	300	6 weeks
EBS-15	14.72	158.5	Opal - 316SS	300	6 weeks
EBS-17	14.44	155.2	Opal – Cu	300	6 weeks
EBS-18	12.77	117.0	Opal – LCS	300	6 weeks
EBS-19	14.82	120.0	Opal – 304SS	300	6 weeks

Table 2: Synthetic groundwater chemistry used in the Opalinus Clay experiments. All values were measured at 25 C (n.m. = not measured)

	Type Solution	**Actual Solution**
Species	mg/L	mg/L
Ca^{2+}	421	426
Cl^{-}	5672	6470
CO_3^{2-}	162	n.m.
K^{+}	221	225

Na^+	3885	3846
Si	5	1
SO_4^{2-}	2305	998
Sr^{2+}	27	0.16
TDS	11502	12153
pH	7.24	7.50
Experiment Used		EBS 14, 15, 17

Section 2 will be a summary of copper alteration and reaction rates, as first described in Caporuscio et al. (2015). Section 3 which describes the mineral interface between bentonite backfill and steel was also summarized by Caporuscio et al. (2015) and will be expanded to include a description of pit corrosion occurring on low carbon steel (EBS-18).

1.2 METHODS

Analytical methods (Experimental Setup, Mineral characterization, and aqueous geochemical analyses) remain unchanged from Caporuscio et al. (2014). They are listed in Appendix A for convenience.

Post-reaction copper foils were mounted in epoxy then polished exposing the cross-sectioned surfaces. These foil mounts were then imaged using two different methods; SEM and reflected light microscopy. For each EBS run 17 to 25 images were taken for each method. These image locations were mapped and chosen to give a random distribution of the corrosion in the foils. All images were saved and analyzed in Photoshop. Each image had 7-20 data points extracted from it. The thickness of the chalcocite layer and the depth of the corrosion pitting were measured and then labeled for future analysis. Corrosion rates were determined by dividing the average corrosion pit depth by the number of days in the run.

2. RESULTS

2.1 EBS 18 experiment

This section focuses on experiment EBS 18 (bentonite –Opalinus Clay- low carbon steel) has detailed results in Appendix B (water chemistry) , Appendix C (XRD analysis), Appendix D (electron microprobe data), and Appendix E – (SEM images).

The aqueous geochemistry results of Appendix B have the following elements of note. Both Ca and Fe go into solution beginning at the 3 week mark (half way through the experiment). The Ca stays in solution, however Fe precipitates upon quenching. Potassium (K) and Na go into solution earlier in the experiment, and both elements begin to precipitate at the two week mark (analcime growth). The trend of SiO_2 is more ambiguous, where filtered and unfiltered cations do not trend together. There is early solution of SiO_2, however SiO_2 then forms solids (Quartz growth) beginning at the second week. Note that there is a dramatic increase in sulfate anions (pyrite breakdown) from the second week till the end of the experiment.

Analysis of the reaction products by QXRD (Appendix C) are not well constrained. Furthermore the results are in part at odds with electron microprobe analyses and SEM EDX analyses. Although clinoptilolite and feldspar match other analytical method characterization, the muscovite, ferrosilite and chlorite determinations are suspect. Samples are presently being rerun by a facility that specializes in clay mineralogy.

Appendix D shows the results of microprobe analyses. Clinoptilolite and analcime-wairakite zeolites are characterized. Abundant authigenic quartz was observed but analyses were not conducted. The rest of the microprobe analyses were performed on the steel / bentonite interface. Interior to the pit corrosion (Appendix E, images E.7 and E.8) the mineral formed is goethite, directly at the steel clay boundary are discontinuous sulfide grains (unable to analyze due to small size), and finally proximal to the steel layer is a layer of Fe-saponite. Images of the saponite are in Appendix E.

SEM / EMS backscattered images depicted in Appendix E were characterized by EDX for mineral identification. Images E.1 and E.2 portray analcime-wairakite euhedral isometric crystals. Clinoptilolite is shown in images E.3 and E.4. Radial growth plagioclase is seen in image E.5. Fe-saponite / low carbon steel interface is depicted in image E.6. Pit corrosion of the low carbon steel in shown in images E.7 and E.8.

2.2 Copper corrosion.

2.2.1 Copper reaction with bentonite

The primary corrosion product for all experiments was chalcocite (Cu_2S) with minor covellite (CuS) appearing in some runs (EBS-17) (Appendix C, C.2.). Chalcocite formed a

hexagonal morphology ranging from discrete plates to completely coalesced patches on the copper surface (Appendix E.9. A & C). Chalcocite crystallized on the copper surfaces due to available H_2S from the decomposition of pyrite in the hydrothermal environment. It is evident that the formation of these surface bound minerals was from the direct crystallization from solution in the localized environments surrounding the metal plates.

There were minor amounts of an unknown fibrous material associated with the copper surface (Appendix E.9.B.). Corrosion seemed to take place with an initial dissolution of the copper developing dissolution features on the copper surface (Appendix E.9.A.).

2.2.2 Copper corrosion

The thickness of the chalcocite layer and the depth of the corrosion pits varied with both temperature profile and experiment duration. In most of the experiments the chalcocite forms a thick layer over a corroded/pitted layer. This layer is visible both in the SEM images of Cu corrosion (Appendix E, E.10) and the reflected light images (Appendix E, E.11). A notable exception to this is the Opalinus Clay run, EBS-17, where the chalcocite layer was found to be either absent or extremely thick. For the ramped temperature experiment, EBS-4, the average chalcocite thickness was 3.0(1) μm. In the isothermal experiments in both bentonite (EBS-11) and Opalinus Clay (EBS-17), the layer was thicker, 8.2(4) μm and 5.6(4) μm respectively. The chalcocite layer was thinner in the six-month long-term cooling run (EBS-16) with a depth of only 2.6(1) μm.

Chalcocite layer thickness generally correlated with the amount of pit corrosion the Cu foil had undergone, but also depended on the sulfur content of the system. The initial overall thicknesses of the copper foils was ~ 63 μm. For EBS-16 and EBS-17, the width of the corrosion pitting was also measured to give an approximate aspect ratio for the corrosion pits. Both the

thickness of the chalcocite and the depth of the pits formed approximately normal distributions for all EBS runs, giving confidence that a random distribution was measured. The only run differing from this pattern was EBS-17, which exhibited two different corrosion environments. One averaged a corrosion pit depth of 9 μm, which is in alignment with the copper corrosion measurements on other EBS runs. The other behavior resulted in significant pitting depths up to and above 25 μm. For the four experiments a total of 849 measurements were made, 414 of the chalcocite layer and 445 of the pit depths. The short-term isothermal experiments in both bentonite and Opalinus Clay yielded similar average pit corrosion depths, 13.5(6) μm and 13.1(6) μm respectively. The ramped experiment (EBS-4) incurred less corrosion, having an average pit depth of only 5.7(2) μm. However, the six-month experiment (EBS-16) copper foils developed only 4.3(1) μm corrosion depths, which is similar to that of EBS-4, but sustained over a much longer period of time. Pitting corrosion was restricted to the exterior surfaces of the rolled copper foil. The surfaces within the rolled copper foil were protected from the brine and thus did not suffer significantly from either chloride or sulfide attack.

Corrosion rates (Appendix F, Table F.1) were determined by dividing the average corrosion pit depth by the number of days in the run. Corrosion rates from the two isothermal experiments on bentonite and Opalinus Clay are within experimental error of each other and displays the highest corrosion rates measured. Copper foils from the Opalinus Clay experiments exhibited several regions of extreme corrosion (Appendix E, E.10 D and Appendix E, E.11 D). These parts of the copper foil were corroded > 50% and show deep channeling in the Cu foil. The corrosion rate for the five week ramped experiment (EBS-4) was half that of the isothermal experiments, 0.16(6) μm/day for the ramped versus ~ 0.31 μm/day for the isothermal experiments. The six-month long-term cooling experiment had a much smaller average corrosion

rate of 0.024(8) μm/day. This is consistent with the reduced corrosion found in the long-term experiment.

The nature of corrosion pitting in the copper foils was similar for all experiments. The average aspect ratio of the width to the depth of the corrosion pits found in the experiment with the least corrosion, the six-month extended cooling run, was 1.4(9). The run with the most corrosion, the six week Opalinus Clay run, had a nearly identical aspect ratio of 1.3(8). The similarity of these aspect ratios indicates that although more rapid corrosion is occurring during the six-week experiment, the pit shapes are unaffected by rate and retains the same nature regardless of the amount of corrosion the copper foil has undergone. A wide variety of corrosion pit structures exist, but extremely deep corrosion pits are just as common as shallow wide ones.

2.3 Steel /bentonite interface mineralogy

304 SS. 304SS underwent uniform interface reaction during the 300°C experiments. Post-reaction 304 SS formed a layer of smectite and chlorite covering the surface of the steel plate (Appendix E., E.12. A & B). However, smectite was the only phyllosilicate associated with the reaction site products in the six week, 300°C reaction (Appendix E., E.12. C & D). The primary type smectite associated with the steel surface appears to be an Fe-saponite. Smectite expands upon ethylene glycol saturation to 16.8 Å (with 002 at 8.35 Å) suggesting no significant amount of mixed-layering is present. Pentlandite ((Cu, Ni, Fe)-sulfide) appears to have formed sparingly in both 304 SS experiments along with an unknown fibrous material (Appendix E., E.12. A & B). The smectite and chlorite morphologies tend to be fairly consistent producing a bladed to micaceous habit with a rose-like texture (Appendix E., E.12). The initial montmorillonite has a distinctly different morphology (foily; Appendix E., E.12C) suggesting smectite associated with

the 304SS is newly formed. The interface reaction products have thicknesses ranging from 9 to 44 μm with crystallites occurring perpendicular to 304SS substrate (Appendix E., E.12. D). There was no significant change in the interface layer thicknesses with increased reaction time at 300°C. Chemical analyses of post-reaction 304SS and the smectite mantle indicates there was a slight Fe transfer from the 304SS forming a Cr-enriched steel outer layer and a Fe-rich smectite and chlorite coating (Appendix E., E.13). The reaction products do include varying degrees of Cr and Ni substitutions. Accurate chemical formula for the interface reaction products are not possible due to the intimate mixing of multiple phases. The average bulk chemistry of the corrosion layer is provided in Appendix F.2. Fe-rich phyllosilicates that formed on steel plates in the ramped experiments have two 06ℓ diffraction bands 1.536 and 1.523 Å (9.138 and 9.216 Å b-parameters), corresponding to trioctahedral chlorite and smectite (Appendix C, C.2.). It is uncertain which minerals species correspond to the b-parameters as there is overlap in the unit-cell parameters between the Mg, Fe-saponites (9.120 (Mg^{2+}) to 9.30 (Fe^{2+}) Å) and chlorite (9.228 to 9.294 Å) species (Kohyama et al. 1973; Moore and Reynolds 1997). The Fe-smectite produced in the six week, 300°C experiment has a 1.547 Å (9.282 Å b-parameters) 06ℓ diffraction band, consistent with Fe-saponite (Kohyama et al. 1973).

316SS. 316 SS underwent exfoliation corrosion during the ramped and isothermal, 300°C experiments. Post-reaction 316 SS formed smectite dominated interface reaction products with some chlorite covering the surface of the steel plate (Appendix E, E.14. A & B). However, smectite was the only phyllosilicate associated with interface reaction products in the six week, 300°C reaction (Appendix E, E.14. C& D). The primary type smectite associated with the steel surface appears to be an Fe-saponite. Smectite expands to 16.8 Å (with 002 at 8.44 Å) upon

ethylene glycol saturation suggesting no significant amount of mixed-layering is present. However, the six weeks, 300°C smectite product expands to 16.3 Å (002 at 8.25 Å) upon ethylene glycol saturation indicating a possible decrease in swelling capacity. A pentlandite-like ((Cu, Ni, Fe)-sulfide) material appears to have also been formed in both 316SS experiments along with what appears to be fibrous sulfides (Appendix E, E.14.D). The smectite and chlorite morphologies tend to be fairly consistent producing a bladed to micaceous habit with a rose-like texture (Appendix E, E.14). The interface reaction products have thicknesses ranging from 20 to 40 μm with crystallites occurring perpendicular to 316SS substrate (Appendix E, E.15 and E.16). There was no significant change in the interface reaction layer thicknesses with increased reaction time at 300°C. Chemical analyses of post-reaction 316SS and mantling products indicates there was significant Fe leaching from the 316SS forming a Cr-enriched steel outer layer up to 4 μm thick. The Cr-enriched layer also underwent oxidation and sulfidation producing a noticeable alteration zone (Appendix E, E.15). Smectite and chlorite coatings were enriched in iron most likely from the iron leached from the 316SS (Appendix E, E.16). Fe-rich phyllosilicates that formed on steel plates in the ramped experiments have 06ℓ diffraction bands 1.535 (9.210 Å b-parameters), corresponding to a trioctahedral phyllosilicate (Appendix C, C.4.; Kohyama et al. 1973; Moore and Reynolds 1997). It is uncertain which minerals species correspond to the b-parameters, however the b-parameter is probably related to an Fe-saponite due to a smectite dominance in the corrosion products. The Fe-smectite produced in the six week, 300°C experiment has a fairly broad 1.54 Å (9.24 Å b-parameters) 06ℓ diffraction band, consistent with Fe-saponite (Kohyama et al. 1973).

Low-carbon steel. Low-carbon steel underwent pitting corrosion during the ramped and isothermal, 300°C experiments. Post-reaction low-carbon steel developed a smectite coating the

steel plate surfaces (Appendix E., E17). Unlike the 304SS and 316SS, there was no evidence of any chlorite phases present in the interface reaction product of the low-carbon steel. The primary type smectite associated with the steel surface appears to be an Fe-saponite. Smectite expands to 16.6 Å (with 002 at 8.32 Å) upon ethylene glycol saturation suggesting no significant amount of mixed-layering is present. Also, pyrrhotite ($Fe_{1-x}S$) platelets formed concurrently with the smectite phases as determined their spatial distribution (Appendix E., E17C). Smectite morphology is varied between a honeycombed texture and rose-like texture with a bladed to micaceous habit (Appendix E., E17 B & D). In addition to the small scaled textures, there is an overlying botryoidal texture with the interface reaction products (Appendix E., E17 C). These interface reaction products have thicknesses ranging from 13 to 56 μm with additional ~ 7 μm corrosion pits. The bladed to micaceous crystallites tend to occur with the longer dimensions perpendicular to the steel substrate (Appendix E., E17 and E18). Chemical analyses of post-reaction low-carbon steel and interface reaction products indicate no chemical fractionation associated with the phase transformation process. Accurate chemical formula for the interface reaction products are not possible due to the intimate mixing of multiple phases. The average bulk chemistry of the interface reaction layer is provided in Appendix F, Table F.3. There does appear to be oxidation and sulfidation associated with the surface (Appendix E., E18). Smectite is enriched in iron most likely due to the iron dissolved from the steel (Appendix E., E18). The Fe-rich smectite has 06ℓ diffraction bands of 1.547 Å (9.264 Å b-parameters), corresponding to a trioctahedral smectite (Appendix C., C.5); Kohyama et al. 1973; Moore and Reynolds 1997).

3 Discussion

3.1 EBS 18 experiment

Cheshire et.al. (2014) wrote a comprehensive work on silicate phase transformations and Caporuscio et.al. (2015) summarized the previous experiments produced for the Argillite EBS experimental research program. Therefore, discussions will be limited to the EBS 18 experiment produced this year. As noted, equipment issues had put the laboratory in stand down mode for over one year, reducing the number of experiments produced. This experiment (EBS-18) sat pressurized at 140 bar and room temperature for 9 months waiting for the equipment issues to be resolved.

To summarize, EBS-18 was run isothermally at 300 ^{o}C for 6 weeks at 150 bar pressure. The components are bentonite clay, Opalinus Clay, Opalinus Clay synthetic groundwater, low carbon steel coupons, and Fe/Mt solid buffer. The phyllosilicates produced in this experiment are equivalent to previous isothermal 300 ^{o}C experiments. The starting montmorillonite converted to smectite (Figure E.3), while the clay material in contact with the steel coupons altered to Fe saponite (Figure E.6). The zeolite phases produced in this experiment include both clinoptilolite (Figure E.3 and E.4.) and an analcime$_{37}$-wairakite$_{63}$ isometric zeolite Figures E.1. and E.2.). When plotted on Si/Al vs percent analcime diagram (see below), certain trends become obvious. There is a clear solid solution series from EBS 14 to EBS 16, with silica increasing slightly toward the analcime end-member. All samples on the trend line were isothermal experiments at 300 ^{o}C. EBS-12 and EBS 18 fall slightly above this line. Sample EBS 12 was slightly under saturated in brine, and sample EBS 18 was held at high pressure for 9 months, as discussed above. This co-existence of both clinoptilolite and “wairakite” within EBS 18 may also be due to long term pressurization of the reactant material. It is believed that the clinoptilolite was allowed

to recrystallize from the original small grains and also incorporate the remnant glass shards into the clinoptilolite. In addition the analcime solid solution samples that cluster with a Si/Al ratio between 4.5 and 5.0 were either the ramped temperature experiment (held at 300 ^{o}C for only a short time) or was the starting material (MR Bentonite) from Colony, Wyoming.

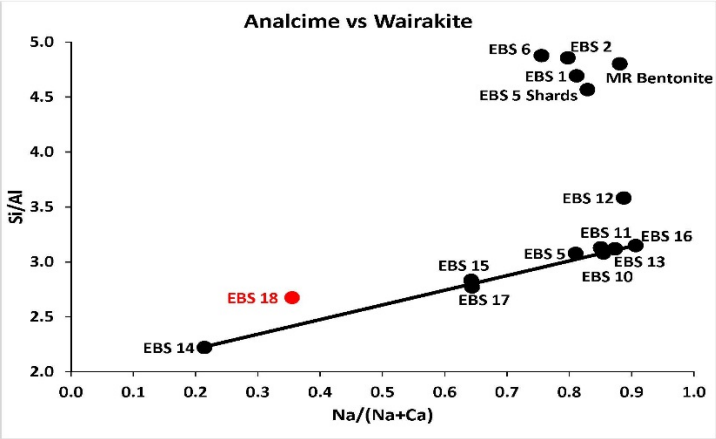

Figure 1: Graph of Si/Al ratio versus Zeolite composition. Trends are dependent on bulk composition and temperature profile

There is also abundant authigenic growth of quartz and plagioclase (Figure E.5.) in the run products of EBS-18.This mineral assemblage (wairakite + plagioclase + quartz + water) was characterized Liuo (1970) for the synthesis of ordered wairakite.

3.2 Copper corrosion

3.2.1 Copper interactions

Copper corrosion in a sulfide-bearing, compacted bentonite environment has been suggested to be a function of both sulfate reducing bacteria growth conditions (e.g., available carbon, sulfate concentrations, and electron donors) and geochemical parameters effecting sulfide diffusion (e.g., bentonite density, fluid content, and ferrous iron concentrations) to the

copper surfaces (Pederson 2010). Overall reactions associated with sulfide-induced copper corrosion involving chalcocite (Cu_2S) formation can be written as,

$$2Cu° + H_2S \rightarrow Cu_2S_{(s)} + 2e^- + 2H^+ \qquad (1a)$$

$$2Cu° + HS^- \rightarrow Cu_2S_{(s)} + 2e^- + H^+ \qquad (1b)$$

$$2Cu° + S^{--} \rightarrow Cu_2S_{(s)} + 2e^- \qquad (1c)$$

One reason for listing these three reactions is to denote the importance of H_2S, HS^-, and S^{--} on activating copper corrosion and the appearance of chalcocite ($Cu_2S_{(s)}$) as the product sulfide solid (Macdonald and Sharifi-Asl, 2011). Under anoxic and high temperature repository conditions, chloride and sulfide corrosion will be the primary (non-radiolytic) mechanism affecting copper waste canisters (King et.al, 2010). Biotic sulfate reduction mechanisms probably will be minimal at high-temperature conditions; therefore the dominant sulfide source is likely from sulfide minerals associated with the original bentonite barrier material or the wall rock. The electrochemical mechanisms of copper corrosion in the case of interactions with sulfide- and chloride-bearing solutions under anaerobic conditions have been advanced by Chen et al. (2010, 2011a); Chen et al. (2011b); King (2010); King and Lilja (2011); King et al. (2013). Macdonald and Sharifi-Asl (2011) provides a comprehensive thermodynamic description of copper stability under various conditions including temperature effects. It is expected that in the presence of Cl-bearing pore solutions or brines, the predominant Cu aqueous complex under nominally anoxic conditions in the presence of bentonite clay and copper metal is $CuCl_2^-$ (King et al., 2013; Schwartz, 2008). The appearance of chalcocite in copper corrosion experiments quantifying the formation of sulfide films has stimulated investigations to understand the effects of such film on the copper surface such as the influence on corrosion rates and mechanisms, and the level of

protectiveness (Chen et al., 2011a). According to Chen et al. (2010, 2011a), the suggested reaction leading to the formation of chalcocite in Cu-Cl solutions can be expressed as:

$$CuCl_2^- + HS^- \rightarrow Cu_2S_{(s)} + 4Cl^- + H^+ \qquad (2)$$

The stepwise mechanism proposed by these authors involves adsorption of the $Cu(HS)_{ads}$ species and its subsequent decomposition to $CuCl_2^-$ and HS^- leading to $Cu_2S_{(s)}$ precipitation as described by reaction (2). However, other mechanisms based on the interaction with Cu-Cl solutions can potentially explain $Cu_2S_{(s)}$ film growth in the presence of Cu^+ and HS^- (e.g., $2Cu^+ + 2HS^- = Cu_2S_{(s)} + H_2S$). Chen et al. (2010) proposed a mechanism for $Cu_2S_{(s)}$ film growth with low porosity during the corrosion process. Although Chen et al. (2010) study suggest that growth of a porous $Cu_2S_{(s)}$ film can be described as diffusion-limited, the heterogeneous nature of the bentonite clay cover on the copper surface (in addition to porous $Cu_2S_{(s)}$) could allow for sufficient porosity for the transport of HS^- and copper aqueous species interacting with both $Cu_2S_{(s)}$ and copper metal interfaces. This observation is indicated by the growth habit of $Cu_2S_{(s)}$ between clay crystals identified in the current experimental work. Mitigating sulfide-induced corrosion might be achieved by maintaining a high bentonite density thereby restricting sulfide diffusion (Pederson 2010). However, given the dynamic nature of bentonite swelling, its porous nature, and moisture transport in the clay EBS such mitigation could be difficult to achieve.

The equilibria between copper metal, $Cu_2S_{(s)}$, and $CuCl_2^-$ can be represented by the following reactions:

$$Cu° + H_2S + CuCl_2^- = Cu_2S_{(s)} + 2Cl^- + H_2 \qquad (3a)$$

$$Cu° + HS^- + CuCl_2^- + ½H_2 = Cu_2S_{(s)} + H_2S + 2Cl^- \qquad (3b)$$

The Eh potential for the invariant point equilibria between copper metal, $Cu_2S_{(s)}$, and $CuCl_2^-$ at 200 and 300 °C are depicted as Pourbaix diagrams in Figure E.19 (a,b). As shown in these diagrams, the Eh potentials are relatively low at the three-phase invariant point, which decreases with increasing temperature. Moreover, the computed equilibrium pH at this invariant point shifts toward near-neutral values with increasing temperature. These diagrams were generated using the CHNOSZ software package (Dick, 2008) and associated thermodynamic database. The diagram was generated assuming activities of SO_4^{--}, Cl^-, and Cu^+ of 1.0×10^{-6}, 0.2, and 1.0×10^{-6}, respectively. The aqueous species activities were constrained by the solute concentrations used in these experiments. Thermodynamic data for $Cu_2S_{(s)}$ in CHNOSZ is sourced to Helgeson et al. (1978).

One question regarding copper surface alteration is whether surface passivation occurs when considering in the long-term barrier material performance of a repository system. There was no substantial change in the mineral thicknesses or surface coverage on copper between the ramped and isothermal, 300°C experiments. The studies by Chen et al. (2010, 2011a) indicate similar mineral surface growth at lower temperatures. Mineral growth restrictions during experiments could possibly be from copper passivation, but can also be explained by depletion in the corrosive species or surface transport. In the case of copper, as sulfide is depleted from the system chloride (in an anoxic environment) becomes the primary corrosive agent, subsequently altering the corrosion rate (King et al. 1992; Carlsson 2008). However, further work needs to be conducted to determine if surface passivation does develop in this system or rather a change in the chemical environment has altered the corrosion rates.

3.2.2Corrosion rates

A multitude of studies have investigated copper corrosion rates. Many of these previous experiments focused on the corrosion of Cu in the air or seawater in application to industrial and naval uses (Kass 1990; Nunez et al. 2005; Sandberg et al. 2006). Copper corrosion has been studied with respect to sulfur and chlorine content in the context of both nuclear repositories and other saline industrial applications (Escobar et al. 1999; Abghari 2013; Bojnov and Makela 2003; Taniguchi and Kawasaki 2008; Chen et al. 2010, 2011a; Kumpulainen et al. 2011). Since long-term experiments on the scale of nuclear repository lifetimes are not possible, archeological findings on the wear of copper artifacts give the best long-term corrosion rates available (Demchenko et al. 2004; Hallberg 1988). The long-term corrosion rates found from these artifacts range from 0.01 to 1.51 μm/yr. The atmospheric and marine corrosion rates are even smaller than this, ranging from 0.0012 to 0.8 μm/yr. in marine water and atmosphere respectively (Nunez et al. 2005). While these rates provide a basic guideline for the corrosion of copper in the nuclear repository, these experiments are not specialized enough to give specific insight into the lifetime of the Cu canister in an EBS.

A handful of experiments have delved into the specific conditions found in repository environments: bentonite clay pack, saline groundwater and elevated temperatures/pressures. Kim et al. (2007) investigated copper corrosion in wet bentonite with synthetic and natural groundwater for 170 to 1231 days at 70°C. These long-term bentonite and saline brine experiments yielded corrosion rates an order of magnitude or more (0.18-0.87 μm/yr.) below those found during the EBS runs in this study (8.8-116 μm/yr.). Kumpulainen et al. (2011) mixed MX-80 bentonite with 0.5 M NaCl solution for 8.2 years yielding a lower corrosion rate (0.035 μm/yr.) compared to the rates from Kim et al. (2007) and much smaller than rates determined from this study. While both Kim and Kumpulainen's experiments used materials found in an EBS,

they did not implement environmental controls such as high temperature and MPa-scale pressures.

Rosborg et al. (2005; 2011) investigated copper bentonite combinations with saline ground water. Their studies yielded corrosion rates between 2.3-20 μm/yr. for one 4.25 years experiment (range is due to measurement technique), which is in agreement with the long-term rate (EBS-16) found in this study. Rosborg et al. (2011) showed that bentonite mixed with oxic saline groundwater for 3 and 4.2 years, yielded copper corrosion rates of 0.4 and 1.6 μm/yr., respectively. These rates are lower compared to the corrosion rates from the current study, but are of the same magnitude as the long-term (180 days) rate found in EBS-16. Taniguchi and Kawasaki (2008) studied mixtures of bentonite and sand with varying NaS_2 concentration at 80°C. As a control they also included a study of copper corrosion in a simple solution with varying NaS_2 concentration. They found corrosion rates increased with increasing NaS_2 concentrations, 15 μm/yr. at 0.1 M NaS_2 and 0.55 μm/yr. at 0.001 M NaS_2. These results validate that sulfur concentrations play a major part in the corrosion process and that relatively high corrosion rates found in this study are likely influenced by the sulfur content of the brine and packing material during the run.

3.2.3 Factors Influencing Corrosion

Several environmental and compositional factors contribute to the higher corrosion rates found in this study. First of all, previous experimental data was collected at significantly lower temperatures than those used in this study. Full EBS experimental data including P,T,t conditions, and chemistry data can be found in Caporuscio, et.al. (2015). For example, EBS-4 started at 25°C and increased to 300°C (573 K) before cooling. The other copper EBS runs all reached 300°C at the outset of the experiment. The highest temperature recorded in similar

experiments is 80°C (353 K) used by Taniguchi and Kawasaki (2008) followed by 70°C (343 K) used by Kim et al. (2007). The experiments of Rosborg et al. (2005; 2011) did not use elevated temperatures. Elevated temperatures increase corrosion rates, especially at neutral to lower pH (Antonijevic and Petrovic 2008; Boulay and Edwards 2001). High temperatures used in this study were chosen to closely simulate a high heat load nuclear repository. The 299°C temperature estimate for a nuclear repository given by Greenberg and Wen (2013) indicate high temperatures better simulate the corrosion activity in a new repository. Other, slower, corrosion rates will only come into play as the heat dissipates over 100 year timescales. Thus, higher corrosion rates found for all EBS test cases are a representation of maximum potential corrosion in the repository scenario we developed, early failure at high temperature / high aqueous water influx due to hydrostatic pressure.

The high corrosion rates measured during this study are also influenced by pressure. The pressure during experimental runs was 15-16 MPa for all EBS runs. Few experimental studies have dealt with corrosion rates at pressures in the MPa range. A study by Betova et al. (2003) investigated the effect of saline groundwater compositions on copper corrosion with no clay included. These experiments were run at 14 MPa and 80^{o}C, which is a good estimate for pressure within a repository if not the temperature. Nuclear waste repositories will likely be 400 to 700 m deep and have to withstand an evenly distributed load of 7 MPa hydrostatic pressure from groundwater and a 7 MPa pressure from swelling of the bentonite (King et al. 2002). Betova et al. (2003) measured corrosion rates of 5.5-17 μm/yr. over six days. These rates are within an order of magnitude in agreement with the results from this study and indicate that elevated pressure may have more of an effect than previously estimated by King et al. (2002), who assumed the pressure effect to be ~ 10% based on theoretical estimates of equilibrium constants

at pressure. Further experimental studies at pressure are needed to elucidate the effect of pressure on Cu corrosion.

The clay and brine composition also make a significant difference in corrosion rate. The brines used in the EBS 4, 11, 16 and 17 runs are listed in Table 1. The composition of the brine for the three bentonite runs (EBS 4, 11 and 16) was similar. The EBS-4 brine contained the highest concentration of Cl- while the EBS-16 brine contained the highest concentration of sulfate. Despite the relatively sulfur and chloride rich compositions, both EBS-4 and EBS-16 underwent less corrosion than EBS-11. This effect is likely due to the differences in temperature profile and is not a sign of different corrosion behavior. The brine used in the Opalinus Clay experiment (EBS-17) was especially high in both chloride and sulfur, an order of magnitude higher in concentration. Several previous studies have concluded that increasing Cl and sulfur content increases the copper corrosion rate (Taniguchi and Kawasaki 2008; Abghari et al. 2013).

The increased corrosion in EBS-17, which shows corrosion tracks penetrating over half of the copper foil in some areas, is due to compositional differences in both brine and in clay. Added to the significant amount of Cl^- and SO_4^{--} in the brine, these compositional differences explain the abundant corrosion of EBS-17. The corrosion of the outer copper foil of EBS-17 was uneven, leading to the interpretation that surface activation reactions by either chloride or sulfur species were inhibited or kinetically-hindered growth of $Cu_2S_{(s)}$ persisted locally throughout the foil's surface.

A final consideration for the corrosion rates measured is the duration of the experiments. A barrier system in a nuclear repository will be required to sustain for 10^5 to 10^6 years, but obviously no experiments can be run at those timescales. Extrapolation must then be used from

measurements made on more human timescales in the laboratory. What timescale is best used becomes the essential question. Three experiment durations were used in this study: 5 weeks, 6 weeks and 6 months. The three 5-6 week experiments (EBS 4, 11 and 17) all yield corrosion rates between 0.16(6) - 0.32(15) μm/day. EBS-16, however, has a much lower corrosion rate, only 0.024(8) μm/day or 8.8(3) μm/year. A similar decrease in corrosion rate, although less dramatic, was observed by Kim et al. (2007). The wet bentonite with synthetic groundwater experiment lasting 188 days at 70°C had a corrosion rate of 0.87 μm/year while the experiment lasting 844 days yielded a corrosion rate of 0.18 μm/year, an 80% reduction in rate. These results indicate that the duration of the experiment does matter and that long-term experiments are necessary to provide the best corrosion rates for extrapolation to long timescales. In addition, the reduced corrosion rate with time suggests the chalcocite layer formation does create a passivation layer that may be effective at repository timescales.

3.3 Steel /bentonite interface mineralogy

Results from these experiments have shown the more dynamic environment associated with this system is at the bentonite-metal interface. Fe-rich phyllosilicates (i.e., trioctahedral, Fe-rich saponite and chlorite) are crystallized on steel surfaces forming a reactive substrate with a high surface area compared to the original steel surfaces. It is evident that the formation of these surface bound minerals is from the direct crystallization from solution in the localized environments surrounding the metal plates. However, it is uncertain to what extent these authigenic minerals will have an effect on the repository system.

Synthetic Fe-saponites have been crystallized in dilute solutions and gels of silica, Fe-, Al-chlorides at temperatures up to 850°C and pH of 8.5 – 9.5 (Kloprogge et al. 1999). This is consistent with a partial dissolution of the steel plates contributing ferrous iron into a fluid phase

with silica and aluminum, thereby facilitating Fe-saponite (smectite) crystallization with the steel surfaces acting as a growth substrate. Further, Fe-saponite alteration into chlorite has been suggested (Mosser-Ruck et al., 2010) in the presence of ferrous iron at temperatures approaching 300°C and near-neutral pH. The stainless steel interaction with bentonite via congruent dissolution/oxidation can be detailed by the following reactions.

Stainless steel dissolution

$Fe_{1.22}Cr_{0.37}Ni_{0.22} \rightarrow 1.22Fe^{2+} + 0.37Cr^{3+} + 0.22Ni^{2+} + 3.99e^-$

Smectite evolution

$Fe^{2+} + Ni^{2+} + Cr^{3+} + H_2S_{(aq)} + (Na,K,Ca)_{0.33}(Al_{1.67},Fe^{3+}_{0.20},Mg_{0.13})Si_4O_{10}(OH)_2 \rightarrow (Fe,Ni,Cr)_9S_8 +$

Smectite `pentlandite

$(Na,K,Ca)_{0.33}Fe_3(Si_{3.67},Al_{0.33})O_{10}(OH)_2$

Fe Saponite

Low carbon steel interaction with clay at low temperature has been investigated by Necib et. al. (2016). They determined two corrosion rates, an active (up to 200 µm/yr.) and a passive (<30 µm/yr.) behavior. They attribute the high corrosion rate to an acidic pH transient (down to 4.5 pH) common to their experiments when pyrite breaks down. Their experiments were run at 85 ^oC and 1 atm. Although the reactants in our samples were similar, the P, T conditions were radically different. Measurement of the deepest corrosion pit for experiment EBS 18 was 125 µm (Figure E.8), which would correlate to 1083 µm/yr. This 5 fold increase in corrosion rate for experiment EBS 18 may be due in part to the elevated P, T (150 bar, 300 ^oC) conditions of our experiment. The other item of note is that the corrosion material inside the pit is goethite [Fe^{+3} O(OH)], an iron oxide phase indicative of highly oxidizing conditions. Perhaps this stage of corrosion is the result of microenvironments where water breaks down (hydrolysis) at the coupon surface and

allows for oxidizing domains in a generally reducing environment. A second possibility is that the low carbon steel coupon began oxidizing while sitting at a pressure of 140 bar for 9 months before temperature was applied. The mechanism of pit corrosion in low carbon steel, along with corrosion rates for the three steel types (304, 326, LCS) would be a very strong focus area for continued study in EBS research.

4 Conclusions

This document summarizes the EBS18 experiment and gives preliminary water chemistry data for EBS 19. There is also a summary of 1) the research conducted on copper corrosion that includes corrosion rates and 2) a partial review of steel bentonite interface reactions and pit corrosion reactions in the low carbon steel coupons of EBS 18.Concepts Developed so far Include:

1) Illitization of smectites may be restricted due to the bulk chemistry of the overall system,
2) Pyrite within bentonite that may be used as backfill reacts readily in groundwater and the resulting H_2S(aq,g) reacts in a minor fashion with steel and aggressively with copper,
3) The interface between bentonite and steel develops a well characterized new mineral phase, Fe-saponite (especially at 300°C), that grows perpendicular to the steel surface,
4) Another Fe layered phyllosilicate, stilpnomelane, grows in the presence on native iron (one of our solid buffer materials), which alludes to the idea that oxygen fugacity may be quite variable, depending on scale,
5) Zeolites transform as temperature increases. Mine run bentonite contains clinoptilolite, and transforms to analcime at higher temperature, releasing both SiO_2 and water. Opalinus Clay upon heating develops wairakite along cracks and edges. The location of these new growth zeolites is due to the impermeable nature of the shale. Mixtures of Opalinus Clay and Colony bentonite produce an intermediate composition Analcime-Wairakite solid solution phase, indicating ease of cation exchange for this zeolite. The experiment EBS 18 exhibited both clinoptilolite and analcime as stable phases.
6) Pit corrosion is the driving force in copper degradation. The copper reacts with H_2S (aq,g) to produce chalcocite and covellite. At latter times in the reaction pathway Cl may combine with copper to produce atacamite.
7) Systematic measurements (N>850) of copper corrosion cross sections have determined corrosion reaction rates at experimental temperatures and pressures. At 6 week duration, corrosion rates ranged from 0.12 to 0.39 micron/day, depending on heating profiles and bulk composition. However, in the 6 month experiment, the corrosion rate dropped by an order of

magnitude, to 0.024 micron/day. We believe that complete coverage by the reaction product chalcocite pacifies the corrosion reaction.
8) Pit corrosion of low carbon steel was common in EBS 18 experiment, and resulted in a corrosion rate of 1083 µm/yr. Mineral products within the pits consisted primarily of goethite, indicative of a highly oxidizing micro environment.

Research needs to be emphasized in the following areas for FY17:

- Corrosion of steels must be the focus of the upcoming year
- Performed detailed geochemical modeling of FY13-FY16 experimental reactions
- International FEBEX-DP – hydrothermal treatment of FEBEX samples expanding the thermal range in addition to routine mineral/geochemical interrogations.
- Perform transmission electron microscope (TEM) investigation looking at very local chemical changes within a pit corrosion metal surface.

5 ACKNOWLEDGEMENTS

We would like to thank Emily Kluk for XRF analyses. Scanning electron microscopy facilities were provided by Materials Science and Technology group at Los Alamos National Laboratory. Dr. George Morgan at the University of Oklahoma was instrumental in the obtaining of EMP analyses. XRD analyses were performed by Dr. Virgil Lueth at N.M. Tech. Funding was through the Department of Energy's Used Fuel Disposition Campaign

6 REFERENCES

Abghari, B., 2013. Corrosion of Copper in Concentrated Aqueous Chloride under Anaeobic Conditions. Master's Thesis, University of Toronto, Department of Chemical Engineering and Applied Chemistry

Antonijevic, M.M. and Petrovic, M.B., 2008. Copper Corrosion Inhibitors. A review. Int. J. Electrochem. Sci., 3, 1-28

Betova, I., Beverskog, B., Bojinov, M., Kinnunen, P., Makela, K., Pettersson, S.-O., Saario, T., 2003. Corrosion of Copper in Simulated Nuclear Waste Repository Conditions. Electrochem. Solid-State Lett. 6, B19-B22

Bojinov, M., Makela, K., 2003. Corrosion of Copper in Anoxic 1M NaCl Solution. POSIVA OY, Olkiluoto, Finland

Boulay, N., Edwards, M., 2001. Role of temperature, chlorine, and organic matter in copper corrosion by-product release in soft water. Water Res., 35, 683-690

Caporuscio, F.A., Cheshire, M.C., Rearick, M.S., and Jove-Colon, C. (2014). - LANL Argillite EBS Experimental Program 2014. FCRD-USED-2014-000491.

Caporuscio, F.A., Cheshire, M.C., Palaich, S., Norskog, K., Jove-Colon, C., (2015) Argillite Disposal R&D-LANL 2015. Summary of baseline experiments for generic repository engineered barriers. Los Alamos National Laboratory FY 2015 – Deliverable UFD Work package # FCRD-UFD-2015-000356, LA-UR-15-26110

Carlsson, T., 2008. Interactions between copper corrosion products and MX-80 bentonite. Svensk Kärnbränslehantering Working Report. TR-08-46, 24

Chen, J., Qin, Z., Shoesmith, D., 2010. Kinetics of corrosion film growth on copper in neutral chloride solutions containing small concentrations of sulfide: J. Electrochem. Soc. 157, no. 10, C338-C345.

Chen, J., Qin, Z., Shoesmith, D., 2011a. Long-term corrosion of copper in a dilute anaerobic sulfide solution: Electrochim. Acta. 56, no. 23, 7854-7861.

Chen, J., Qin, Z., Shoesmith, D., 2011b. Rate controlling reactions for copper corrosion in anaerobic aqueous sulphide solutions: Corros. Eng. Sci Tech. 46, no. 2,138-141.

Cheshire, M.C., Caporuscio, F.A., Jové-Colón, C., and McCarney, M.K. (2013) Alteration of clinoptilolite into high-silica analcime within a bentonite barrier system under used nuclear fuel repository conditions. Proceeding from the 14th International High-Level Radioactive Waste Management Conference, 410-415.

Cheshire, M.C., Caporuscio, F.A., Jove-Colon, C., and McCarney, M.K. (2014) Bentonite Clay Evolution at Elevated Pressures and Temperatures: An experimental study for generic nuclear repositories. American Mineralogist, V99, pp1662-1675

Chipera, S.J. and Bish, D.L. (2002) FULLPAT: a full-pattern quantitative analysis program for X-ray powder diffraction using measured and calculated patterns. Journal of Applied Crystallography, 35, 744–749.

Chung, F.H. (1974) Quantitative interpretations of X-ray diffraction patterns of mixtures. I. Matrix flushing method for quantitative multicomponent analysis. Journal of Applied Crystallography, 7, 519-525.

Coombs, D.S. (1955) X-ray observations on wairakite and non-cubic analcime. Mineralogical Magazine, 30, 699-708.

Crerar, D.A., Susak, N.J., Borcsik, M., and Schwartz, S. (1978) Solubility of the buffer assemblage pyrite + pyrrhotite + magnetite in NaCl solution from 200 to 350°C. Geochimica et Cosmochimica Acta, 42, 1427-1437.

Demchenko, L.V., Zlobenko, B.P., Manichev, V.I., Kadoshnikov, V.V., Spasova, L.V., 2004. Corrosion of Archeological Artefacts from the Olviya Site in Ukraine. Mat. Res. Soc. Symp. Proc. 807, 1-6.

Dick, J. M., 2008, Calculation of the relative metastabilities of proteins using the CHNOSZ software package: Geochem. Trans. 9, 10.

Eberl, D.D., Velde, B., and McCormick, T. (1993) Synthesis of illite-smectite from smectite at Earth surface temperatures and high pH. Clay Minerals, 28, 49-60.

Escobar, I. S., Silva, E., Silva, C., Ubal, A., 1999. Proc. Fourth Inter. Conf. Copper 99-Cobre99, 1, 371

Ferrage, E., Vidal, O., Mosser-Ruck, R., Cathelineau, M., and Cuadros, J. (2011) A reinvestigation of smectite illitization in experimental hydrothermal conditions: Results from X-ray diffraction and transmission electron microscopy. American Mineralogist, 96, 207-223.

Greenburg, H.R. and Wen, J. (2013) Repository layout and host rock thermal gradient trade study for large waste packages in clay/shale: Using the DSEF thermal analytical model. LLNL-TR-639869-DRAFT, pp. 38.

Guillaume, D., Neaman, A., Cathelineau, M., Mosser-Ruck, R., Peiffert, C., Abdelmoula, M., Dubessy, J., Villieras, F., Baronnet, A., and Michau, N., (2003) Experimental synthesis of chlorite from smectite at 300 °C in the presence of metallic Fe. Clay Minerals, 38, 281-302.

Hallberg, R.O., Ostlund, P., Wadsten, T., 1988. Inferences from a corrosion study of a bronze cannon, applied to high level nuclear waste disposal. Appl. Geochem. 3, 273-280.

Helgeson, H. C., Delany, J. M., Nesbitt, H. W., and Bird, D. K., 1978, Summary and Critique of the Thermodynamic Properties of Rock-Forming Minerals: Am. J. Sci. 278. 1-229

Jové-Colón, C. F., Caporuscio, F. A., Levy, S. S., Sutton, M., Blink, J., Greenberg, H. R., Fratoni, M., Halsey, W. G., Wolery, T. J., Rutqvist, J., et al. (2011) Disposal Systems Evaluations and Tool Development - Engineered Barrier System (EBS) Evaluation (Fuel Cycle Research and Development). Sandia National Laboratory, FCRD-USED-2011-000132, 1-192.

Kass, J., 1990. Evaluation of copper, aluminum bronze, and copper-nickel container material for the Yucca Mountain Project. Proc. Corr. Nucl. Fuel Waste Containers. IAEA. RN:23004457. 87-107.

Kim, S.S., Chun, K.S., Kang, K.C., Baik, M.H., Kwon, S.H., Choi, J.W., 2007. Estimation of the corrosion thickness of a disposal container for high-level radioactive wastes in a wet bentonite. J. Ind. Eng. Chem. 13, 959-964.

King, F., 2005. Overview of the corrosion behavior of copper and steel used fuel containers in a deep geologic repository in the sedimentary rock of the Michigan Basin, Ontario: Ontario Power Generation, Nuclear Waste Management Division Report.

King, F., 2007. Status of the understanding of used fuel container corrosion processes – Summary of current knowledge and gap analysis (NWMO TR-2007-09): Canada, NWMO. 104.

King, F., Ahonen, L., Taxen, C., Vuorinen, U., Werme, L., 2002. Copper corrosion under expected conditions in a deep geological repository. POSIVA OY, Helsinki, Finland. 185

King, F., Lilja, C., Pedersen, K., Pitkänen, P., Vähänen, M., 2010. An update of the state-of-the-art report on the corrosion of copper under expected conditions in a deep geologic repository. Swedish Nuclear Fuel and Waste Management Co. (SKB), Technical Report TR-10-67, 180.

King, F., Lilja, C., 2011. Scientific basis for corrosion of copper in water and implications for canister lifetimes: Corr. Eng. Sci. Tech. 46, no. 2, 153-158.

King, F., Lilja, C., Vähänen, M., 2013. Progress in the understanding of the long-term corrosion behavior of copper canisters: J. Nucl. Mater. 438, no. 1, 228-237.

King, F., Litke, C.D., Ryan, S.R., 1992. A mechanistic study on the uniform corrosion of copper in compacted Na-montmorillonite/sand mixtures. Corr. Sci. 33, 1979-1995.

Kloprogge J.T., Evans, R., Hickey, L., Frost, R., 1999. Characterization and Al-pillaring of smectites from Miles, Queensland (Australia). Applied Clay Science V20. Issue 4-5 January 2002, 157-163

Kohyama, N., Shimoda, S., and Sudo, T. (1973) Iron-rich saponite (ferrous and ferric forms). Clays and Clay Minerals, 21, 229-237.

Kumplulainen, S., Kiviranta, L., Carlsson, T., Muurinen, A., Svensson, D., Sasamoto, H., Yui, M., Wersin, P., Rosch, D., 2011. Long-term alteration of bentonite in the presence of metallic iron. POSIVA OY, Eurajoki, Finland. Report 2010-71

Liuo, J.G. (1970) Synthesis and stability relations of Wairakite, CaAl2Si4O12 2H2O. Cont. Min. Pet., 27, 259-282

Macdonald DD, Sharifi-Asl S. 2011. Is copper immune to corrosion when in contact with water and aqueous solutions? Swedish Radiation Safety Authority, SSM, Report. 2011:09

Madsen, F.T. (1998) Clay mineralogical investigations related to nuclear waste disposal. Clay Minerals, 33, 109-129.

Meunier, A., Velde, B., and Griffault, L. (1998) The Reactivity of Bentonites: a Review. An Application to Clay Barrier Stability for Nuclear Waste Storage. Clay Minerals, 33, 187-196.

Moore, D. M. and Reynolds, R.C. (1997) X-ray Diffraction and the Identification and Analysis of Clay Minerals. Oxford University Press, New York, New York, pp. 377.

Mosser-Ruck, R., Cathelineau, M., Guillaume, D., Charpentier, D., Rousset, D., Barres, O., and Michau, N. (2010) Effects of Temperature, pH, and Iron/Clay and Liquid/Clay Ratios on Experimental Conversion of Dioctahedral Smectite to Berthierine, Chlorite, Vermiculite, or Saponite. Clays and Clay Minerals, 58, 280-291

Necib, S., Linard, Y., Crusset, D., Michau, N., Daumas, S., Burger, E., Romaine, A., and Schlegel, M.L. (2016) Corrosion at the carbon steel–clay borehole water and gas interfaces at 85 ◦C under anoxic and transient acidic conditions, Corros. Sci. http://dx.doi.org/10.1016/j.corsci.2016.04.039

Nunez, L., Reguera, E., Corvo, F., Gonzalez, E., Vazquez, C., 2005. Corrosion of copper in seawater and its aerosols in a tropical island. Corr. Sci. 47, 461-484

Nutt, M. Voegele, M., Jové-Colón, C.F., Wang, Y., Howard, R., Blink, J., Liu, H.H., Hardin, E., and Jenni, K. (2011) Used fuel disposition campaign disposal research and development road map (Fuel cycle research and development). Sandia National Laboratory, FCRD-USED-2011-000065, 1-121.

Pederson, K., 2010. Analysis of copper corrosion in compacted bentonite clay as a function of clay density and growth conditions for sulfate-reducing bacteria. J. Appl. Microbiol. 108, 1094-1104

Pearson, F.J., Arcos, D., Bath, A., Boisson, J.-Y., Fernandez, A.M., Gabler, H.-E., Gaucher, E., Gautschi, A., Griffault, L., Hernan, P., and Waber, H.N. (2003) Mont Terri Project-Geochemistry of water in the Opalinus Clay Formation at the Mont Terri Rock Laboratory. – Reports of the Federal Office for Water and Geology (FOWG), Geology Series No. 5.

Pouchou, J.L. and Pichoir, F. (1985) “PAP” □(□z) correction proced
quantitative microanalysis. Microbeam Analysis. Ed. Armstrong, J.T. San Francisco Press, pp. 104-106.

Pusch, R. (1979) Highly compacted sodium bentonite for isolating rock-deposited radioactive waste products. Nuclear Technology, 45, 153-157.

Rosborg, B., Pan, J., Leygraf, C., 2005. Tafel slopes used in monitoring of copper corrosion in a bentonite/groundwater environment. Corr. Sci. 47, 3267-3279.

Rosborg, B., Kosec, T., Kranjc, A., Pan, J., Legat, A., 2011. Electrochemical impedance spectroscopy of pure copper exposed in bentonite under oxic conditions. Electrochem. Acta. 56, 7862-7870.

Sandberg, J., Wallinder, I.O., Leygraf, C., Le Bozec, N., 2006. Corrosion-induced copper runoff from naturally and pre-patinated copper in a marine environment. Corr. Sci. 48, 4316-4338.

Schwartz, M. O., 2008. High-level waste disposal, ethics and thermodynamics. Env. Geol. 54, no. 7, 1485-1488.

Seyfried, J.R., Janecky, D.R., and Berndt, M.E. (1987) Rocking autoclaves for hydrothermal experiments II. The flexible reaction-cell system. Hydrothermal Experimental Techniques. Eds. Ulmer, G.C. and Barnes, H.L. John Wiley & Sons, pp. 216 – 239.

Środoń, J. (1980) Precise identification of illite/smectite interstratifications by X-ray powder diffraction. Clays and Clay Minerals, 28, 401-411.

Taniguchi, N., Kawasaki, M., 2008. Influence of sulfide concentration on the corrosion behavior of pure copper in synthetic seawater. J Nucl. Mater. 379, 154-161

Wersin, P., Johnson, L.H., and McKinley, I.G. (2007) Performance of the bentonite barrier at temperatures beyond 100°C: A critical review. Physics and Chemistry of the Earth, 32, 780-788.

Appendix A
Methods and mineral characterization

a. Experimental Setup

The bentonite used in this experimental work is mined from a reducing horizon in Colony, Wyoming. The bentonite was pulverized and sieved to < 3 mm and used with a free moisture of ~15.5 wt. %. The groundwater solution was prepared using reagent grade materials dissolved in double deionised water. NaOH and HCl were added to adjust the initial solution pH. This solution was then filtered through a 0.45 μm filter and sparged with He before each experiment. The salt solution was added at 9:1 water: bentonite ratio. Initial components for wall rock experiments have been summarized in Table 1 of text.

A second series of experiments were performed to examine the bentonite system with host rock inclusion. Host-rock experiments focused on Opalinus Clay from the Swiss Underground Research Laboratory located at Mont Terri. The core was collected from BFE-A10 drill core (interval from 11 to 12 m and interval from 33 to 34 m from the borehole head). A portion of the Opalinus Clay was crushed and sieved with 10 mesh (~2 mm). Opalinus Clay to be used in experiments was reconstituted at 80 wt. % -10 mesh and 20 wt. % +10 mesh. Synthetic groundwater was chosen to replicate the groundwater composition that represents Opalinus Clay pore water (Table 2 of text, Pearson et al., 2003). The salt solution was added at 9:1 water: rock ratio.

The redox conditions for each system were buffered using a 1:1 mixture (by mass) of Fe_3O_4 and Fe° added at 0.07 wt. % of the bentonite mass. Approximately 7 wt. % (of total solids mass) 304 stainless steel (NIST SRM 101g), 316 stainless steel (NIST SRM 160b), Cu-foil, and low-carbon steel (provided by Sandia National Laboratory) were added to the experiments to mimic the presence of a waste canister.

Reactants were loaded into either a flexible gold or titanium bag and fixed into a 500 mL Gasket Confined Closure reactor (Seyfried et al. 1987). Experiments were pressurized to 150 - 160 bar and were heated isothermally at 300 °C for 6 weeks Reaction liquids were extracted during the experiments and analyzed to investigate the aqueous geochemical evolution in relationship to mineralogical alterations. The sampled reaction liquids were split three-ways producing aliquots for unfiltered anion, unfiltered cation, and filtered (0.45 μm syringe filter) cation determination. All aliquots were stored in a refrigerator at 1°C until analysis.

b. Mineral Characterization

X-ray diffraction (XRD) analyses of experimental materials determined mineral compositions. Each sample was ground with 20 wt. % corundum (Al_2O_3) for quantitative XRD analysis of the bulk rock (Chung 1974). XRD measurements were conducted with a Siemens D500 diffractometer using Cu-Kα radiation. Data were collected from 2 to 70 °2θ with a 0.02 º2θ step-size and count times of 8 to 12 seconds per step. To better analyze the non-clay and clay fractions, the < 2 μm particles were separated via sedimentation in DI H_2O. An aliquot of the < 2 μm suspension was dropped on a zero-background quartz plate and dried. This oriented mount was X-rayed from 2 to 40 °2θ at 8 to 12 s per step. The oriented mount was

then saturated with ethylene glycol in a 60 °C oven for 24 hours and XRD analysis was repeated. A portion of the > 2 μm particles was ground with a mortar/pestle, deposited on a zero-background quartz plate, and X-rayed under the same parameters as the bulk powder material. The remaining > 2 μm portion was used for electron microscopy. Mineral identification and unit-cell parameters analysis was performed using Jade© 9.5 X-ray data evaluation program with ICDD PDF-4 database. Quantitative phase analysis (QXRD) was performed using FULLPAT (Chipera and Bish 2002). Illite-smectite composition of higher-ordered (R1-3) illite-smectites were modeled via ClayStrat+ (developed by Hongji Yuan and David Bish). Expandable component abundances for the disordered illite-smectites were calculated via the Δ°2Θ method (Środoń 1980; Eberl et al. 1993; Moore and Reynolds 1997). A regression from calculated data were used to calculate the % expandable (%Exp) component in each untreated and reacted bentonite. The equations are:

$$\%Exp = 973.76 - 323.45\Delta + 38.43\Delta^2 - 1.62\Delta^3$$ (Eberl et al. 1993, Eq. 3, R^2=0.99),

with Δ corresponding to Δ°2Θ between the 002 and 003 peak positions for the oriented, ethylene glycol saturated samples.

Analytical electron microscopy was performed using a FEI™ Inspect F scanning electron microscope (SEM). All samples were Au/Pd-coated prior to SEM analysis. Imaging with the SEM was performed using a 5.0 kV accelerating voltage and 1.5 spot size. Energy dispersive X-ray spectroscopy (EDX) was performed at 30 kV and a 3.0 spot size.

Electron microprobe (EMP) analyses were performed at the University of Oklahoma using a Cameca SX50 electron microprobe equipped with five wavelength-dispersive spectrometers and PGT PRISM 2000 energy-dispersive X-ray detector. Petrographic characterization was performed by backscattered electron imaging coupled with energy-dispersive X-ray analysis, using beam conditions of 20 kV acceleration and 20 nA sample current. Quantitative analysis was performed by wavelength-dispersive spectrometry using 20 kV accelerating voltage, 20 nA beam current, and 2 μm spot size. Matrix corrections employed the PAP algorithm (Pouchou and Pichoir 1985), with oxygen content calculated by stoichiometry. Counting times were 30 seconds on peak for all elements, yielding minimum levels of detection (calculated at 3-σ above mean background) in the range of 0.01 to 0.03 wt. % of the oxides for all components except F (0.16 wt. %). All standards for elements in the silicates were analyzed using 30 second count times on peak, using K-alpha emissions. The standards and oxide detection limits are presented in Appendix A, with analytical data presented in Appendix B.

c. Aqueous Geochemical Analyses

Major cations and trace metals were analyzed via inductively coupled plasma-optical emission spectrometry (Perkin Elmer Optima 2100 DV) and inductively coupled plasma-mass spectrometry (Elan 6100) utilizing EPA methods 200.7 and 200.8. Ultra-high purity nitric acid was used in sample and calibration preparation prior to sample analysis. Internal standards (Sc, Ge, Bi, and In) were added to samples and standards to correct for matrix effects. Standard Reference Material

(SRM) 1643e Trace Elements in Water was used to check the accuracy of the multi-element calibrations. Inorganic anion samples were analyzed by ion chromatography (IC) following EPA method 300 on a Dionex DX-600 system. Aqueous geochemical results are presented in Appendix C.

Appendix B
Water Chemistry
Sample EBS-18

Lab ID	Date analyzed	Date Sampled	Al	B	Ba	Ca	Cl	Fe	K	Li	Mg	Mn
EBS-18 REACTION VESSEL	4/5/2016	2/17/2016	<0.02	<0.04	0.02	22	860	21	17	0.3	0.03	0.38
EBS 18 F	05/2/16	1/14/2016	1.1	3.25	0.18	17	---	<0.2	78	2	<0.2	0.02
EBS 18 F	05/2/16	1/28/2016	0.1	3.91	0.36	29	---	<0.2	96	1	9.8	0.06
EBS-18 F	4/5/2016	2/4/2016	<0.02	2.65	0.12	14	---	<0.2	62	1.5	<0.2	<0.02
EBS-18 F	4/5/2016	2/16/2016	<0.02	0.82	0.11	284	---	8	20	1.1	1.61	0.31
EBS-18-POST RUN F	4/5/2016	2/17/2016	<0.02	0.70	0.13	308	---	2	24	1.3	5.40	0.32

EBS 18 UF	05/2/16	1/14/2016	1.8	3.60	0.19	17	3761	<0.2	75	2	<0.2	0.03
EBS 18 UF	05/2/16	1/28/2016	0.2	4.73	0.35	28	4544	<0.2	97	1	9.7	0.06
EBS-18 UF	4/5/2016	2/4/2016	<0.02	3.10	0.13	14	2684	<0.2	66	1.6	0.21	0.04
EBS-18 UF	4/5/2016	2/16/2016	<0.02	0.71	0.11	290	1377	7	20	1.1	1.90	0.31
EBS-18-POST RUN UF	4/5/2016	2/17/2016	<0.02	0.57	0.13	309	1435	2	24	1.3	5.60	0.31

Lab ID	Date analyzed	Date Sampled	Na	Si	SiO2	SO4	Sr	Zn	TDS	Cation	Anion	Balance
EBS-18 REACTION VESSEL	4/5/2016	2/17/2016	511	70	150	45	0.10	<0.02	1628	25	25	0.00
EBS 18 F	05/2/16	1/14/2016	2109	99	211	---	0.2	0.19	2421	95	0	1.00
EBS 18 F	05/2/16	1/28/2016	2572	215	461	---	0.2	0.24	3174	116	0	1.00
EBS-18 F	4/5/2016	2/4/2016	1559	75	161	---	0.12	<0.02	1800	70	0	1.00
EBS-18 F	4/5/2016	2/16/2016	907	117	250	---	1.70	<0.02	1475	55	0	1.00
EBS-18-POST RUN F	4/5/2016	2/17/2016	1028	90	194	---	1.76	<0.02	1565	61	0	1.00

EBS 18 UF	05/2/16	1/14/2016	2165	84	179	16.95	0.2	0.24	6221	97	106	-0.05
EBS 18 UF	05/2/16	1/28/2016	2609	103	219	57.6	0.2	0.30	7571	117	129	-0.05
EBS-18 UF	4/5/2016	2/4/2016	1568	196	419	28	0.14	<0.02	4788	71	76	-0.04
EBS-18 UF	4/5/2016	2/16/2016	918	104	222	957	1.72	<0.02	3797	55	59	-0.03
EBS-18-POST RUN UF	4/5/2016	2/17/2016	999	80	170	1054	1.79	<0.02	4006	60	62	-0.02

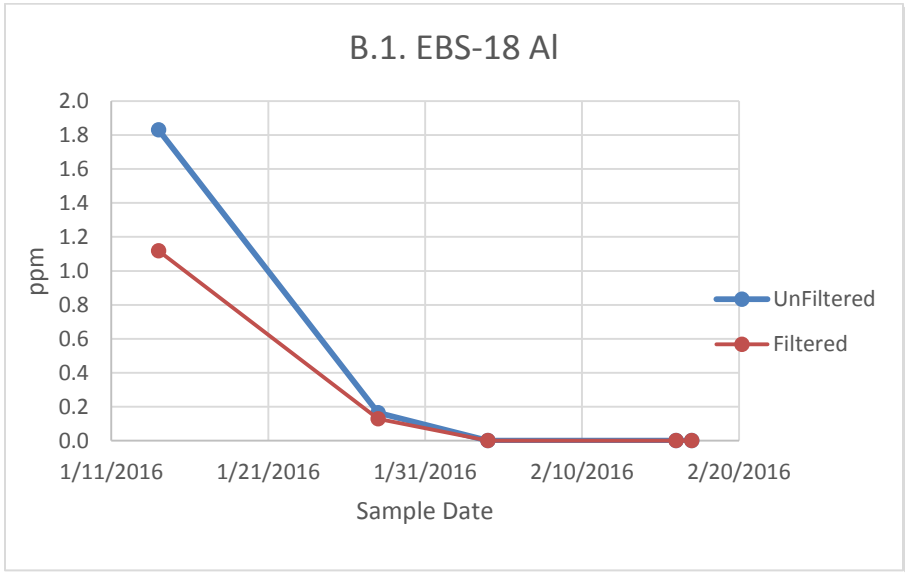
B.1. EBS-18 Al
2.0
1.8
1.6
1.4
1.2
1.0
0.8
0.6
0.4
0.2
0.0
ppm
1/11/2016
1/21/2016
1/31/2016
2/10/2016
2/20/2016
Sample Date
UnFiltered
Filtered

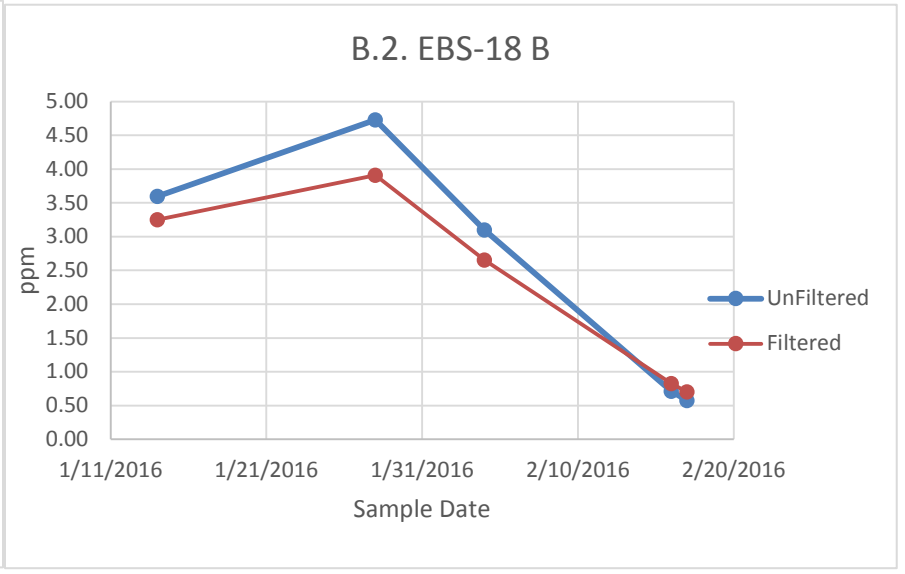
B.2. EBS-18 B
5.00
4.50
4.00
3.50
3.00
2.50
2.00
1.50
1.00
0.50
0.00
ppm
1/11/2016
1/21/2016
1/31/2016
2/10/2016
2/20/2016
Sample Date
UnFiltered
Filtered

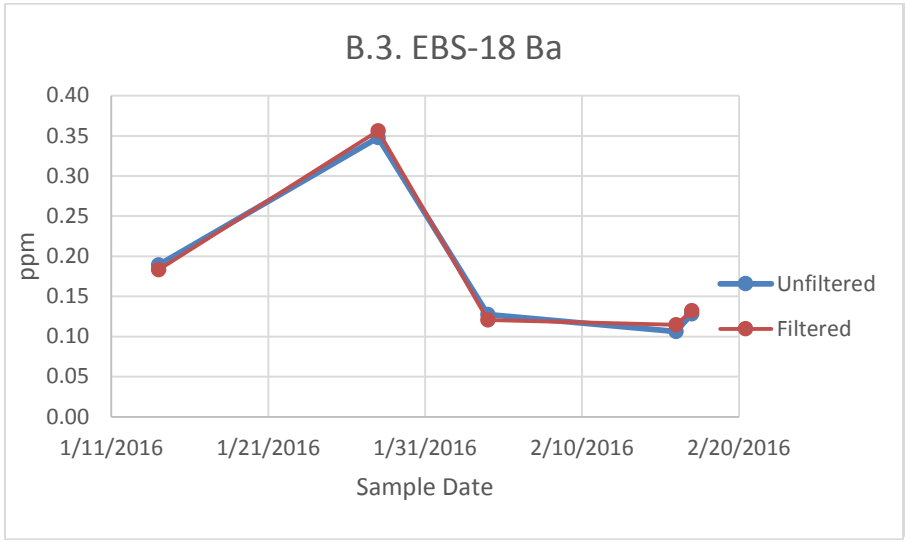
B.3. EBS-18 Ba
0.40
0.35
0.30
0.25
0.20
0.15
0.10
0.05
0.00
ppm
1/11/2016
1/21/2016
1/31/2016
2/10/2016
2/20/2016
Sample Date
Unfiltered
Filtered

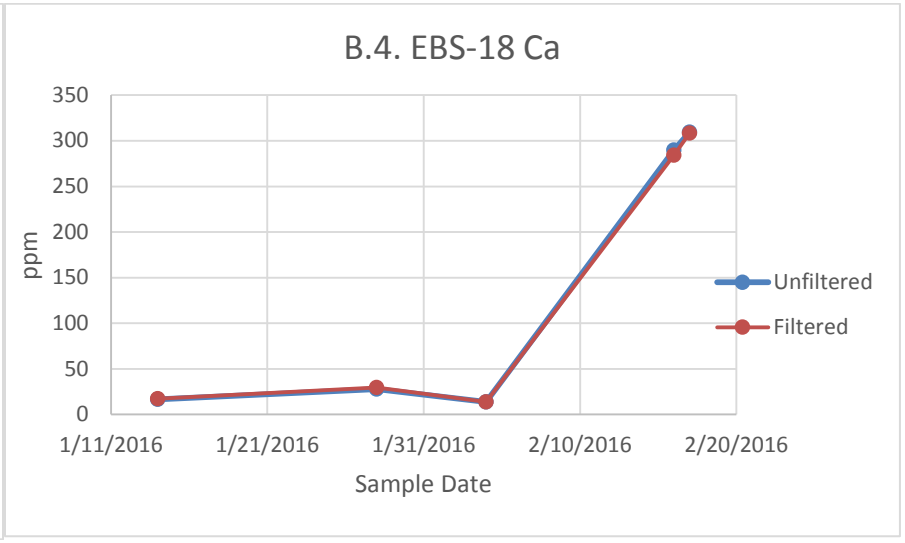
B.4. EBS-18 Ca
350
300
250
200
150
100
50
0
ppm
1/11/2016
1/21/2016
1/31/2016
2/10/2016
2/20/2016
Sample Date
Unfiltered
Filtered

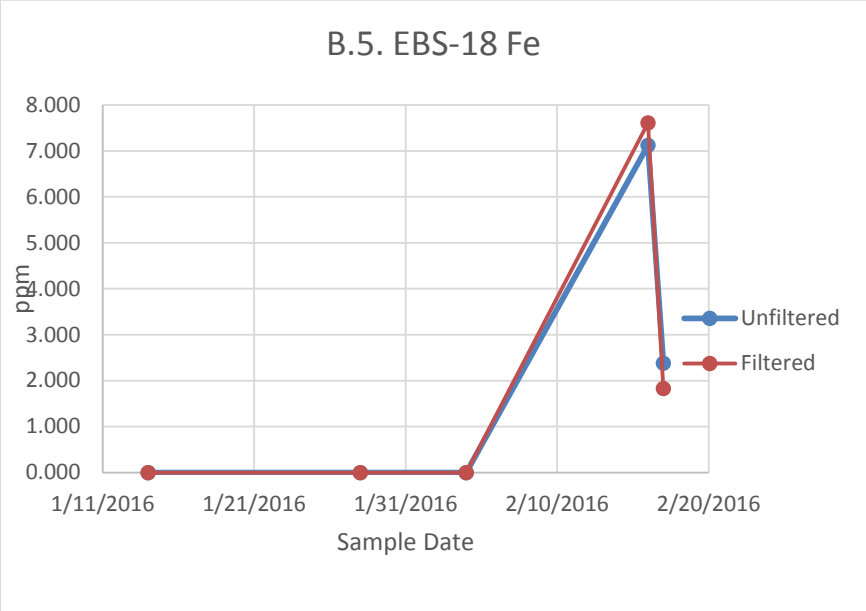
B.5. EBS-18 Fe
8.000
7.000
6.000
5.000
4.000
3.000
2.000
1.000
0.000
ppm
1/11/2016
1/21/2016
1/31/2016
2/10/2016
2/20/2016
Sample Date
Unfiltered
Filtered

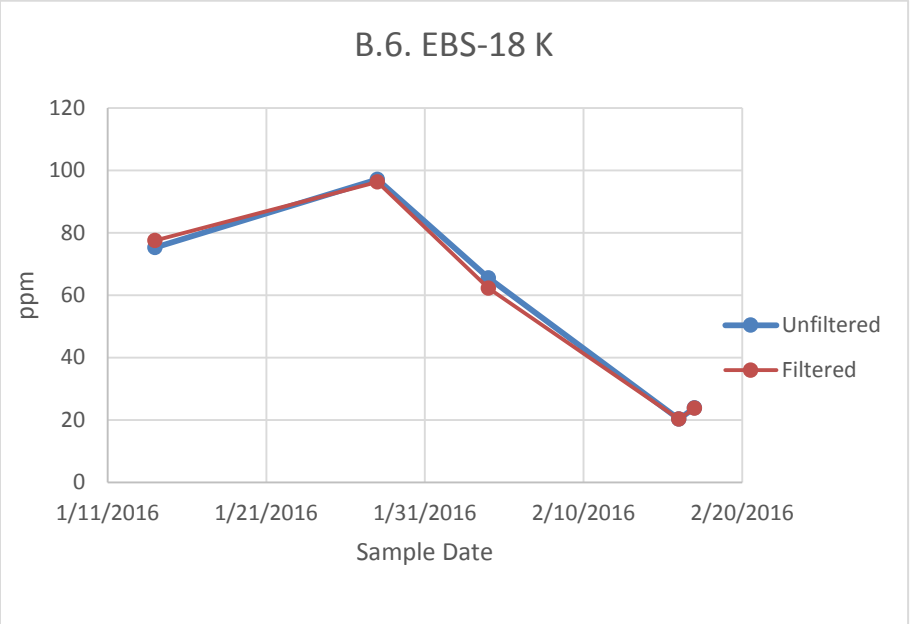
B.6. EBS-18 K
120
100
80
60
40
20
0
ppm
1/11/2016
1/21/2016
1/31/2016
2/10/2016
2/20/2016
Sample Date
Unfiltered
Filtered

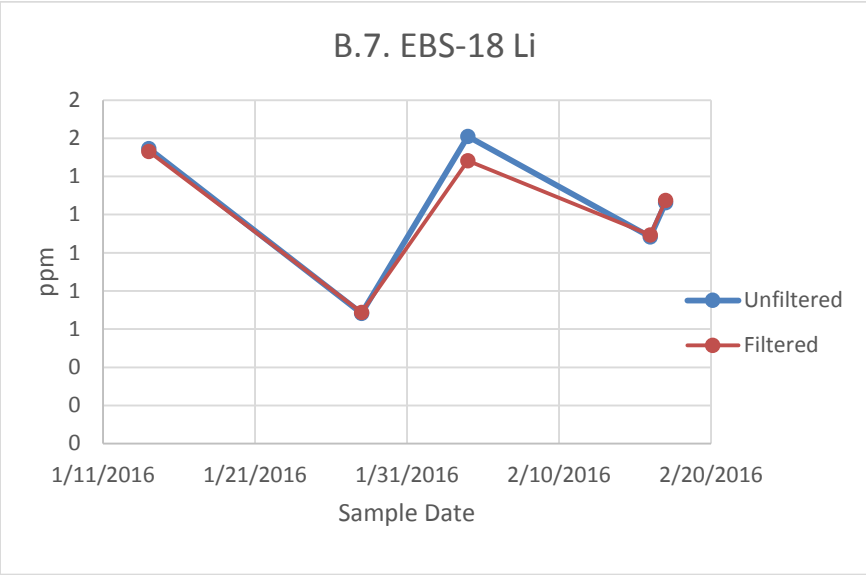
B.7. EBS-18 Li
2
2
1
1
1
1
1
0
0
0
ppm
1/11/2016
1/21/2016
1/31/2016
2/10/2016
2/20/2016
Sample Date
Unfiltered
Filtered

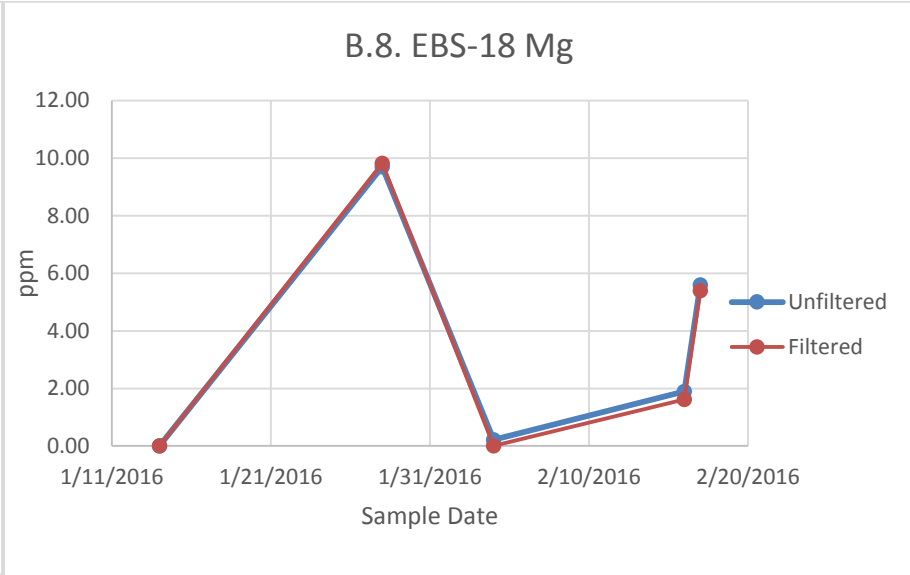
B.8. EBS-18 Mg
12.00
10.00
8.00
6.00
4.00
2.00
0.00
ppm
1/11/2016
1/21/2016
1/31/2016
2/10/2016
2/20/2016
Sample Date
Unfiltered
Filtered

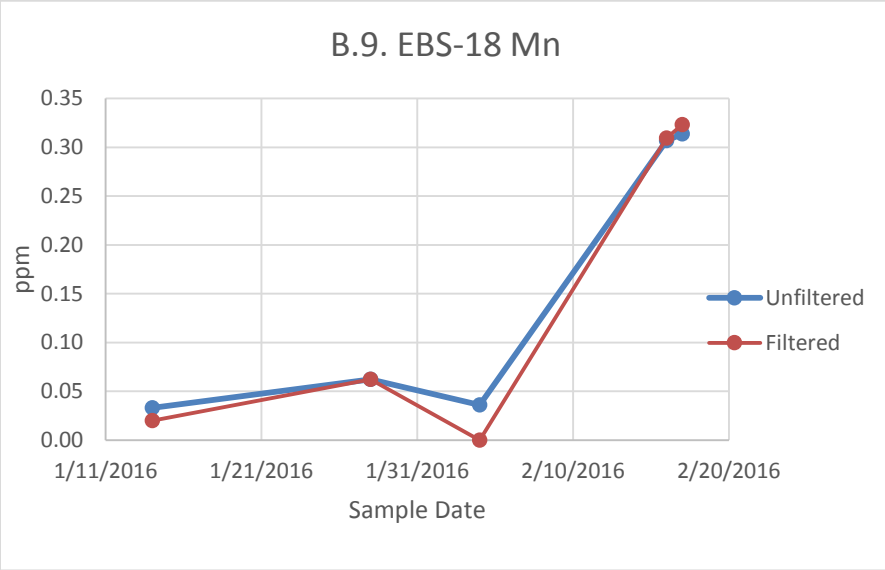
B.9. EBS-18 Mn
0.35
0.30
0.25
0.20
0.15
0.10
0.05
0.00
ppm
1/11/2016
1/21/2016
1/31/2016
2/10/2016
2/20/2016
Sample Date
Unfiltered
Filtered

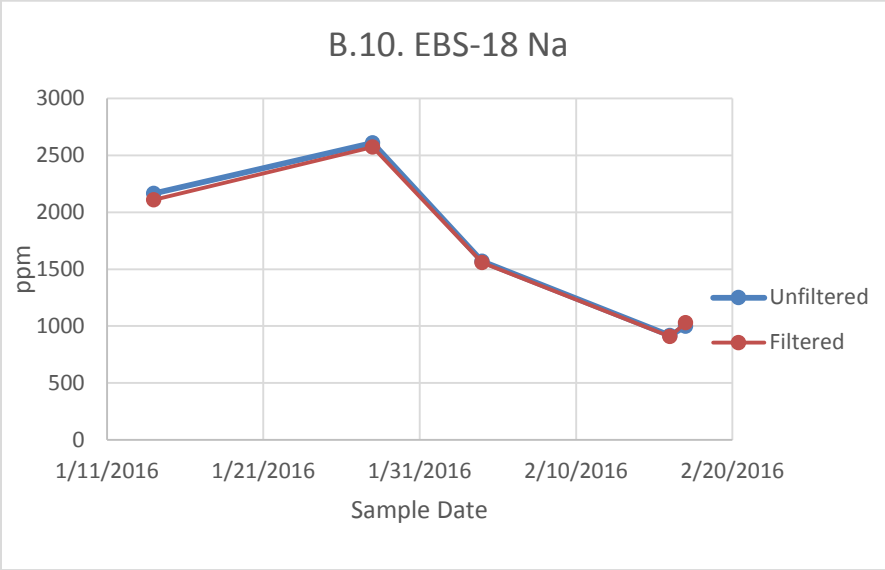
B.10. EBS-18 Na
3000
2500
2000
1500
1000
500
0
ppm
1/11/2016
1/21/2016
1/31/2016
2/10/2016
2/20/2016
Sample Date
Unfiltered
Filtered

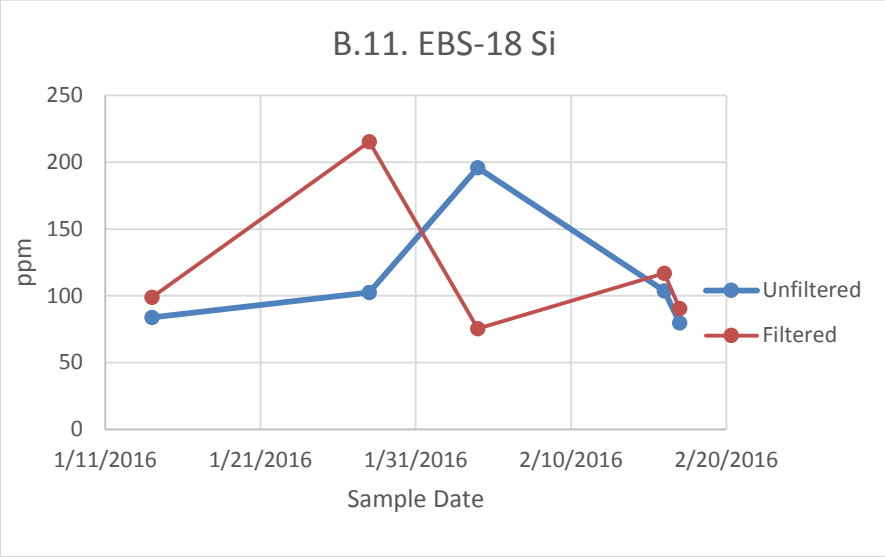
B.11. EBS-18 Si
250
200
150
100
50
0
ppm
1/11/2016
1/21/2016
1/31/2016
2/10/2016
2/20/2016
Sample Date
Unfiltered
Filtered

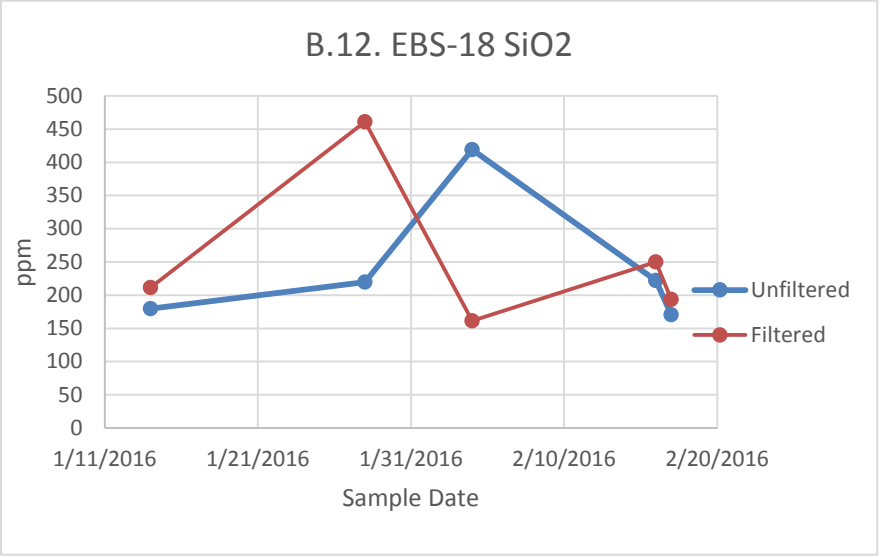
B.12. EBS-18 SiO2
500
450
400
350
300
250
200
150
100
50
0
ppm
1/11/2016
1/21/2016
1/31/2016
2/10/2016
2/20/2016
Sample Date
Unfiltered
Filtered

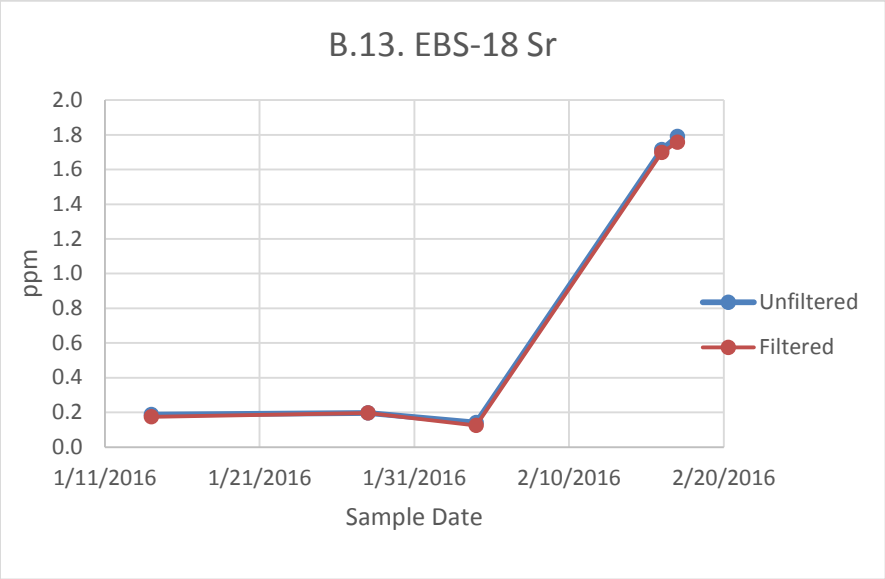
B.13. EBS-18 Sr
2.0
1.8
1.6
1.4
1.2
1.0
0.8
0.6
0.4
0.2
0.0
ppm
1/11/2016
1/21/2016
1/31/2016
2/10/2016
2/20/2016
Sample Date
Unfiltered
Filtered

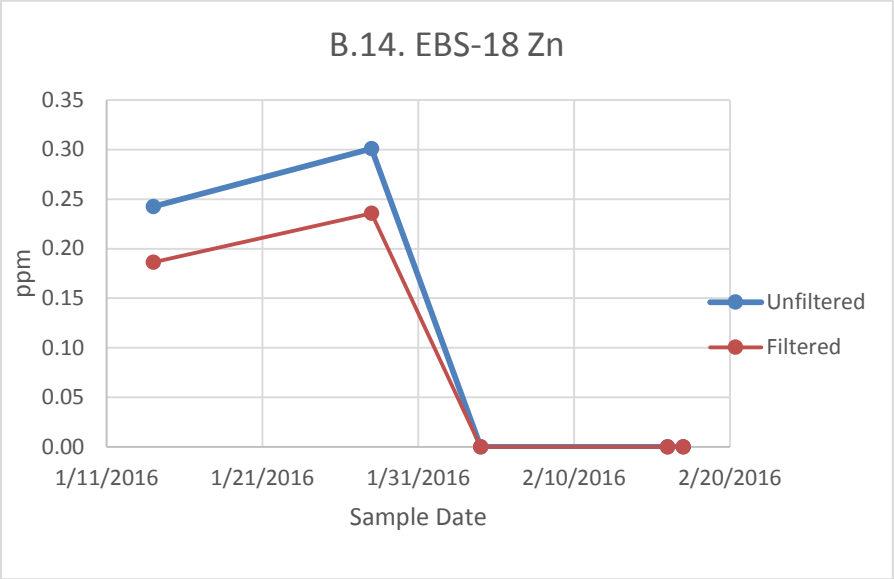
B.14. EBS-18 Zn
0.35
0.30
0.25
0.20
0.15
0.10
0.05
0.00
ppm
1/11/2016
1/21/2016
1/31/2016
2/10/2016
2/20/2016
Sample Date
Unfiltered
Filtered

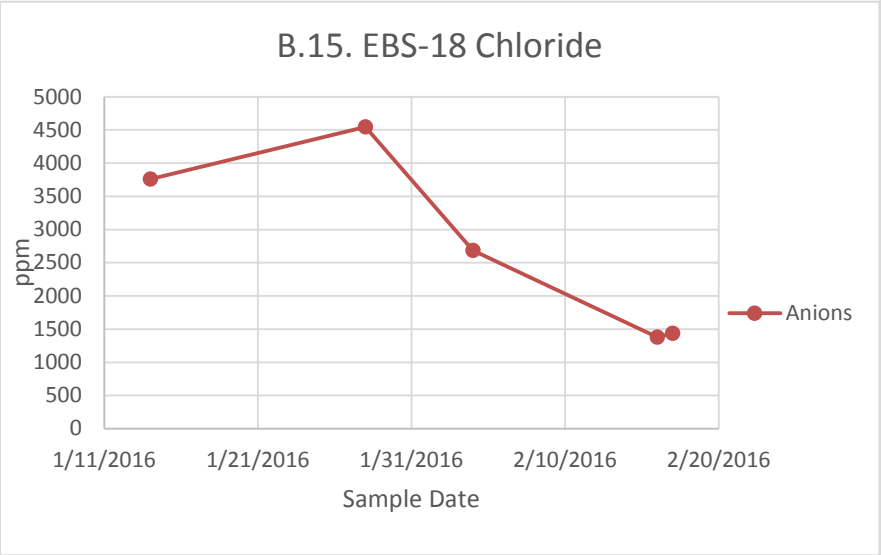
B.15. EBS-18 Chloride
5000
4500
4000
3500
3000
2500
2000
1500
1000
500
0
ppm
1/11/2016
1/21/2016
1/31/2016
2/10/2016
2/20/2016
Sample Date
Anions

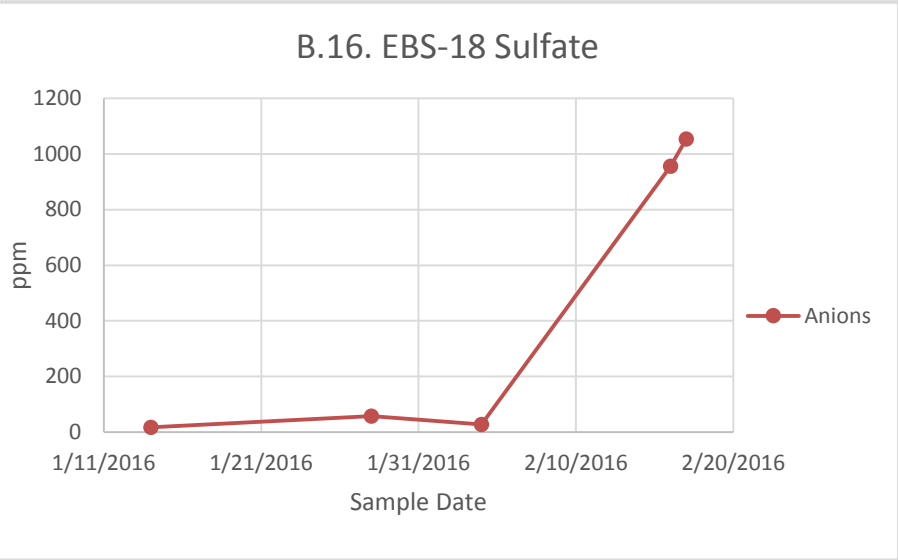
B.16. EBS-18 Sulfate
1200
1000
800
600
400
200
0
ppm
1/11/2016
1/21/2016
1/31/2016
2/10/2016
2/20/2016
Sample Date
Anions

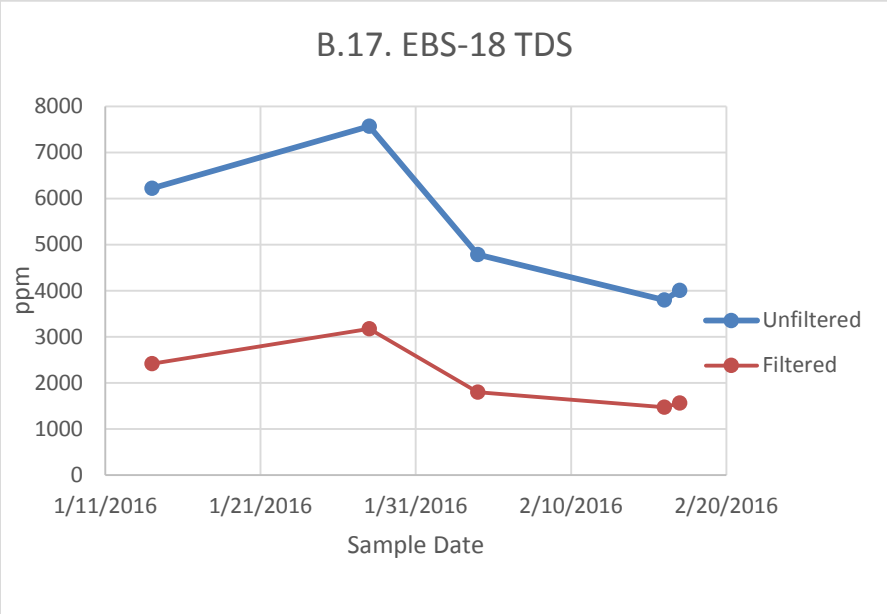
B.17. EBS-18 TDS
8000
7000
6000
5000
4000
3000
2000
1000
0
ppm
1/11/2016
1/21/2016
1/31/2016
2/10/2016
2/20/2016
Sample Date
Unfiltered
Filtered

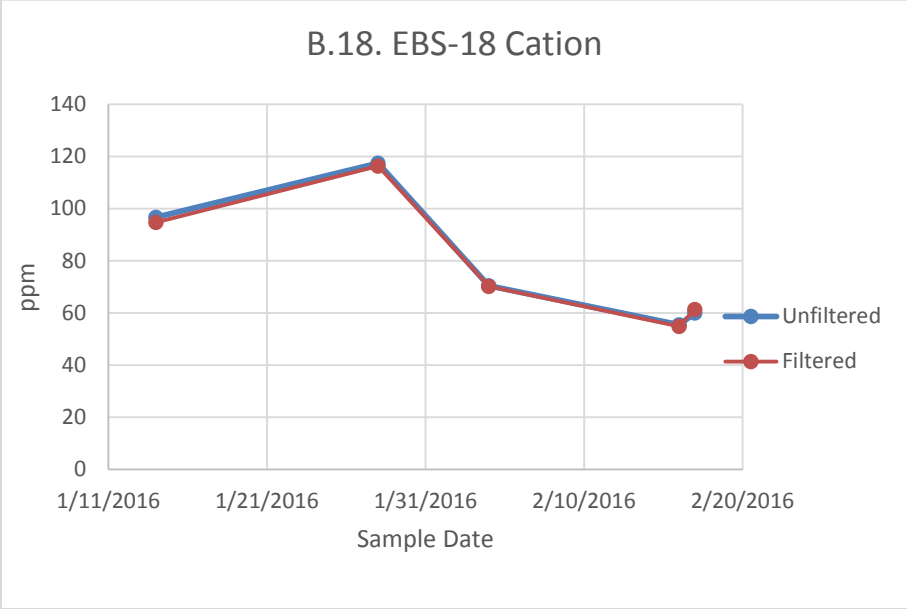
B.18. EBS-18 Cation
140
120
100
80
60
40
20
0
ppm
1/11/2016
1/21/2016
1/31/2016
2/10/2016
2/20/2016
Sample Date
Unfiltered
Filtered

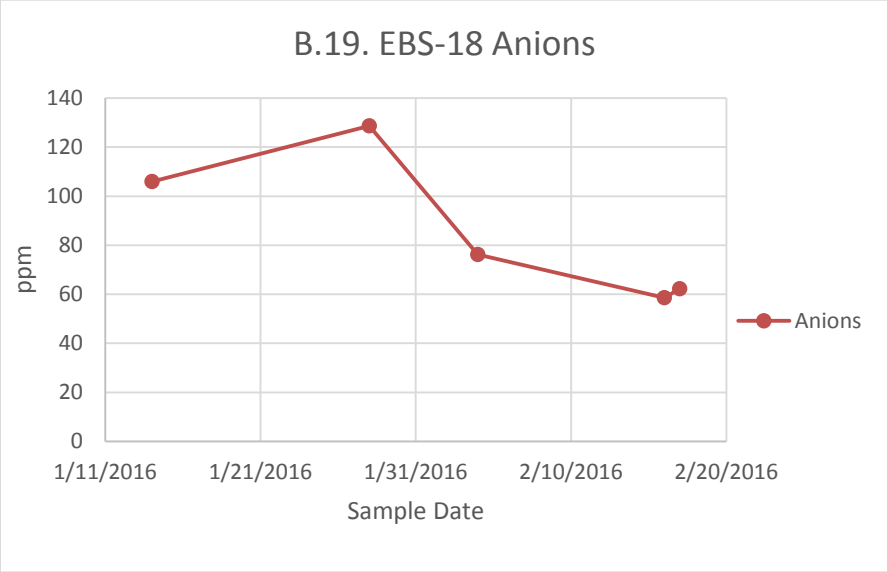
B.19. EBS-18 Anions
140
120
100
80
60
40
20
0
ppm
1/11/2016
1/21/2016
1/31/2016
2/10/2016
2/20/2016
Sample Date
Anions

Appendix C
X-Ray Powder Diffraction Data

EBS-18

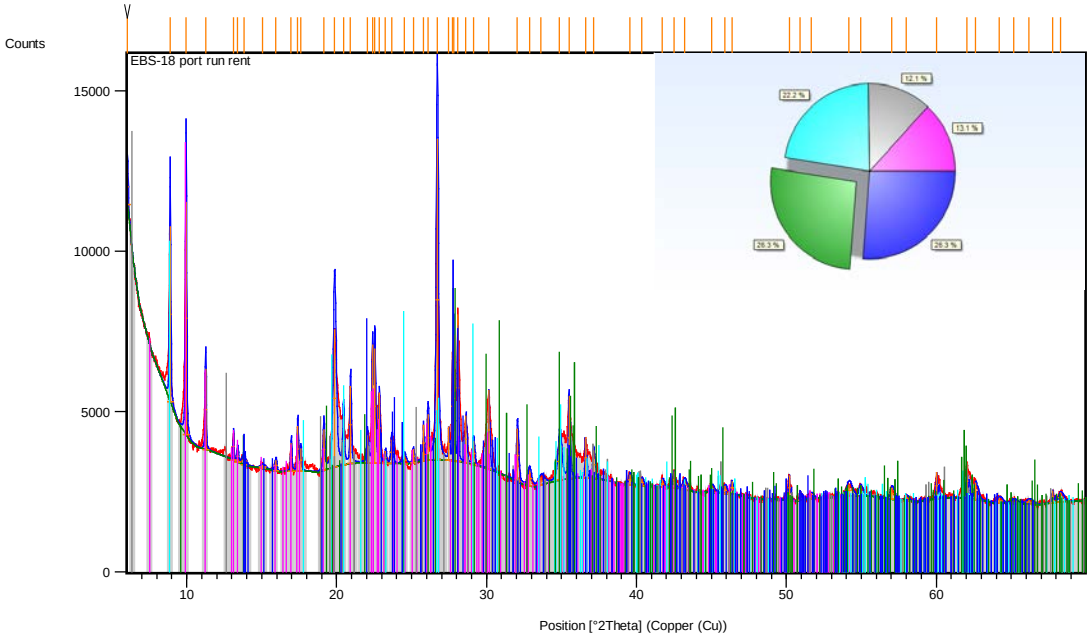

C.1. Semi quantitative analysis of EBS-18 matrix material

QXRD

Mineral Phase	Volume percentage
clinoptilolite	**13**
albite	**26**
ferrosilite	**26**
muscovite	**23**
chlorite	**12**

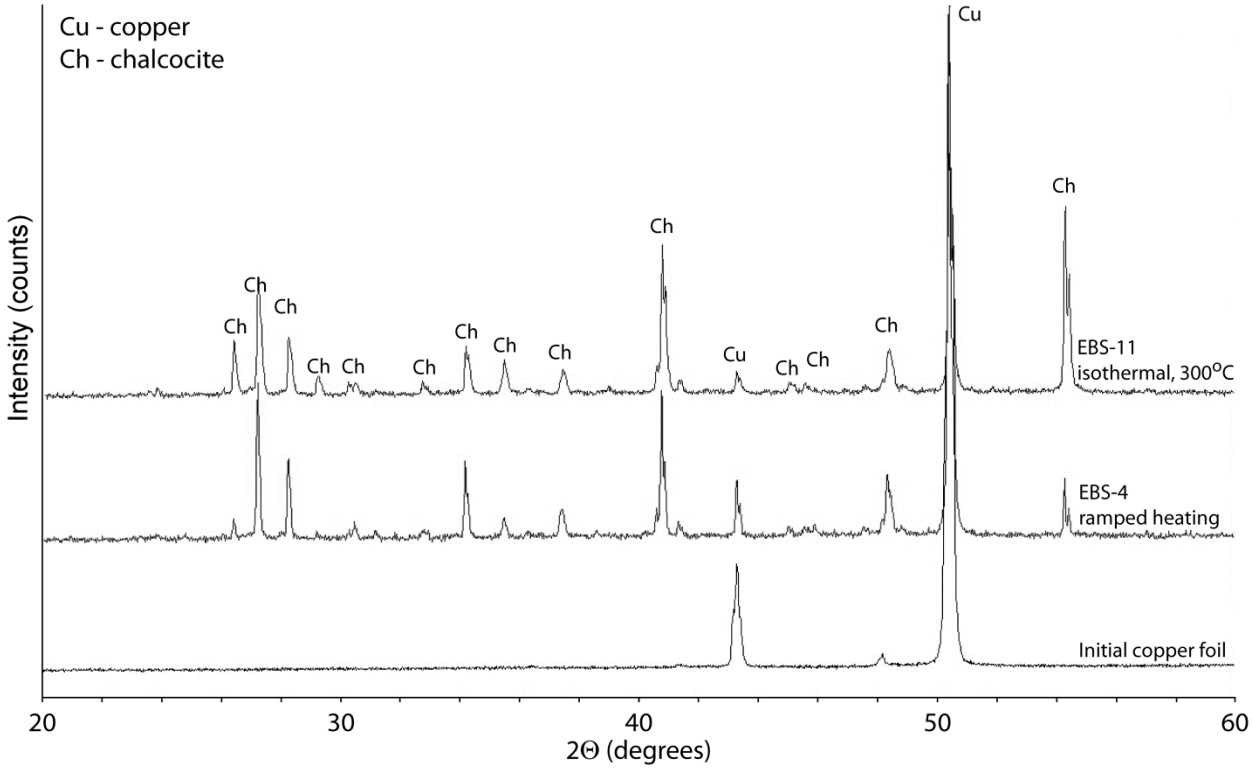

C.2. XRD plots for corrosion products on the copper foils used in the ramped heating (EBS-4) and six week, 300°C heating (EBS-11) experiments. Chalcocite (Cu_2S) is the principal corrosion phase.

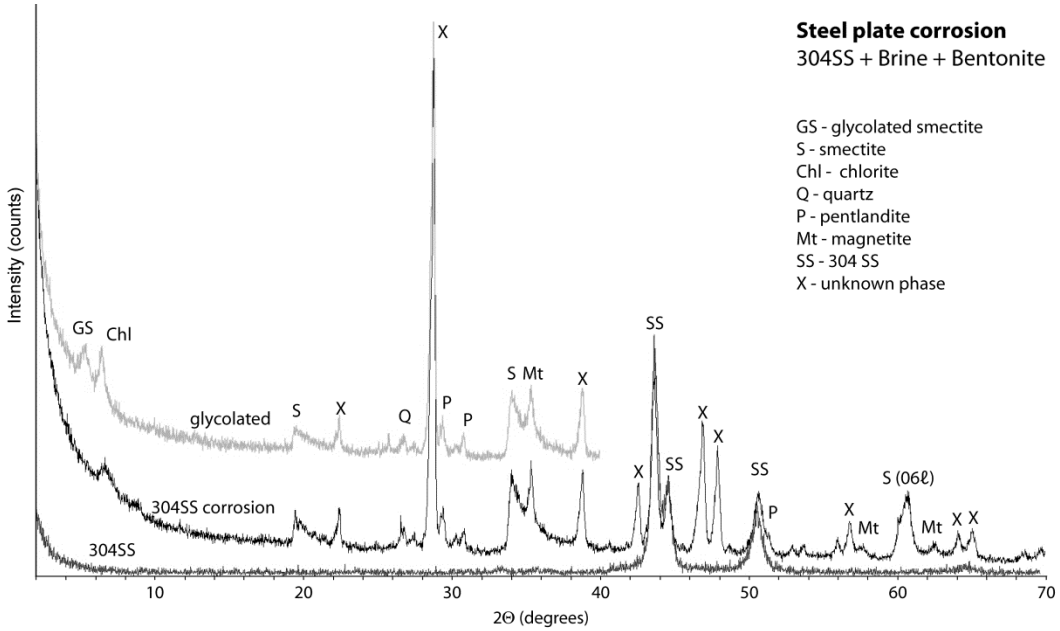

C.3. XRD patterns of the air-dried and ethylene glycol saturated corrosion products on the 304 SS plate used in the EBS-2 experiment. Smectite, chlorite, and a pentlandite-like material are the dominant interface reaction phases. Starting 304SS XRD plot is also shown for comparison.

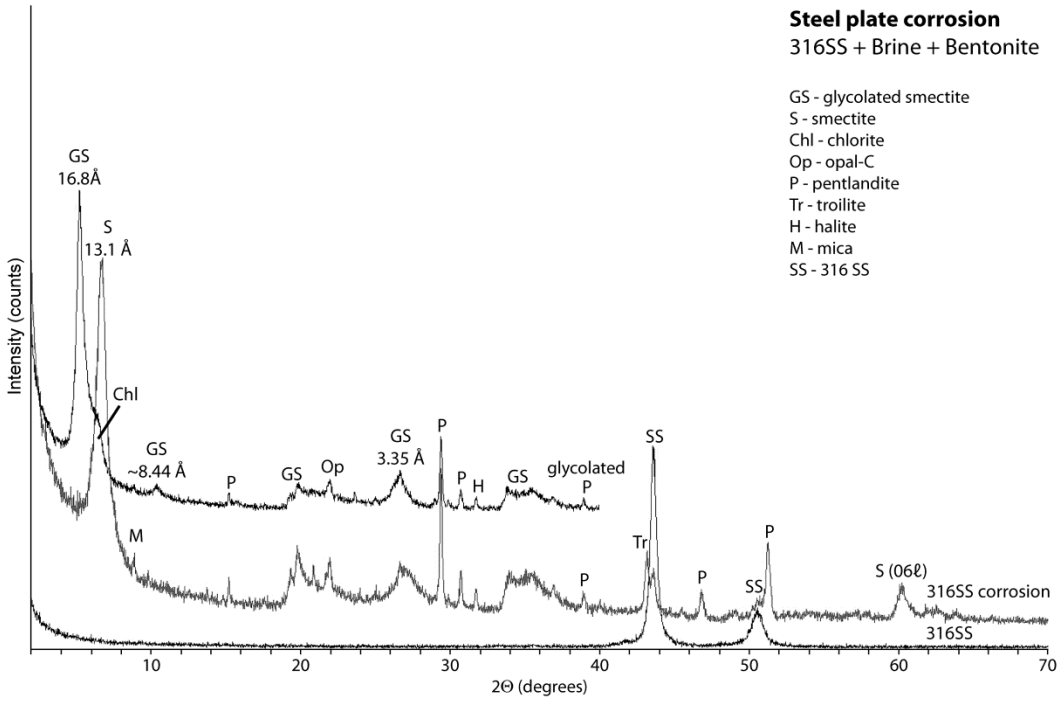

C.4. XRD patterns of the air-dried and ethylene glycol saturated interface reaction products on the 316SS plate used in the EBS-3 experiment. Smectite, chlorite, and a pentlandite-like material are the dominant corrosion phases. Starting 316SS XRD plot is also shown for comparison.

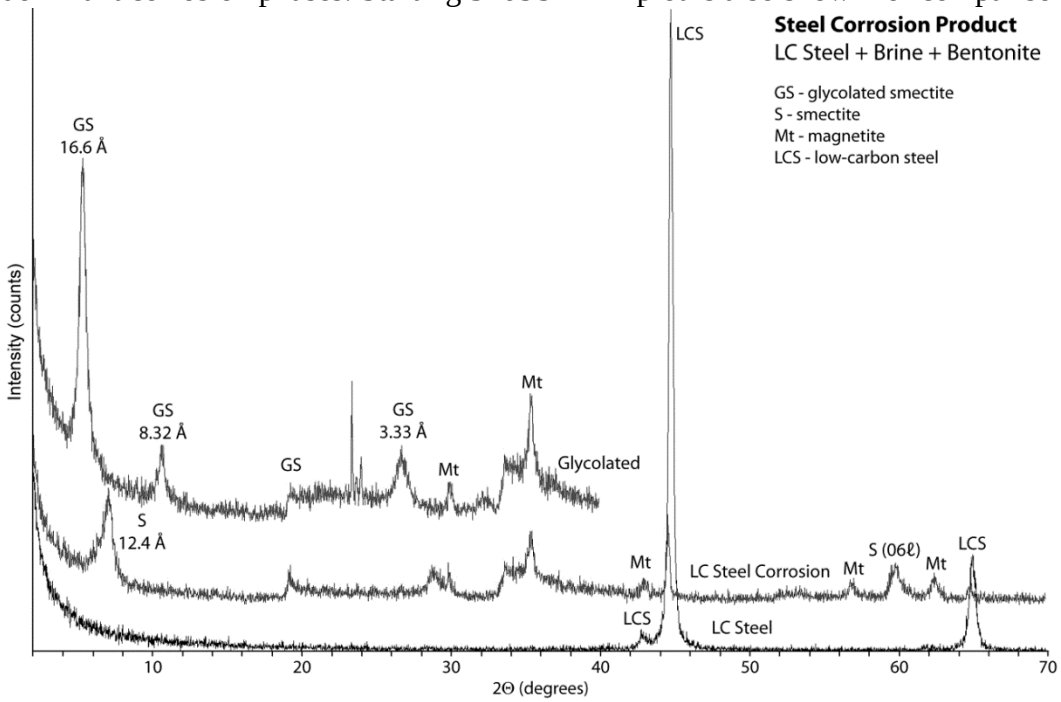

C.5. XRD patterns of the air-dried and ethylene glycol saturated interface reaction products on the low-carbon steel plate used in the EBS-6 experiment. Smectite is the dominant interface reaction phase. Magnetite is most likely from the starting magnetite materials used to control redox conditions. Initial low-carbon steel XRD plot is also shown for comparison.

Appendix D
Electron Microprobe data

		Weight Percent														
SAMPLE	**Pt#**	**SiO2**	**TiO2**	**Al2O3**	**Cr2O3**	**FeO**	**NiO**	**MnO**	**MgO**	**CaO**	**Na2O**	**K2O**	**Cl**	**F**	**O=Hal**	**TOTAL**
CLINOPTILOLITE																
EBS-18 Clinop	1	58.65	0.02	21.06	0.02	0.99	0.00	0.01	0.39	4.48	3.16	0.23	0.02	0.00	-0.01	89.03
EBS-18 Clinop	2	60.56	0.03	22.70	0.00	0.50	0.00	0.01	0.58	5.68	2.71	1.36	0.01	0.07	-0.03	94.21
EBS-18 Clinop	3	59.96	0.20	20.98	0.03	2.13	0.00	0.03	0.77	4.15	2.07	0.55	0.04	0.04	-0.03	90.95
EBS-18 Clinop	4	72.82	0.29	15.08	0.02	1.84	0.00	0.04	0.66	2.17	1.35	0.95	0.05	0.11	-0.06	95.37
EBS-18 Clinop	5	57.26	0.21	21.26	0.01	4.54	0.02	0.05	1.75	2.98	1.58	1.13	0.08	0.00	-0.02	90.87
AVE.		**61.85**	**0.15**	**20.22**	**0.01**	**2.00**	**0.00**	**0.03**	**0.83**	**3.89**	**2.17**	**0.84**	**0.04**	**0.04**	**-0.03**	**92.09**
Std Dev		**6.26**	**0.12**	**2.95**	**0.01**	**1.56**	**0.01**	**0.02**	**0.53**	**1.36**	**0.76**	**0.45**	**0.03**	**0.05**	**0.02**	**2.62**
	18 Atoms per formula unit (sum excludes F & Cl)															
		Si	**Ti**	**Al**	**Cr**	**Fe**	**Ni**	**Mn**	**Mg**	**Ca**	**Na**	**K**	**Cl**	**F**		**Sum**
EBS-18 Clinop	1	6.437	0.001	2.724	0.002	0.090	0.000	0.001	0.065	0.526	0.673	0.032	0.004	0.000		10.552
EBS-18 Clinop	2	6.332	0.002	2.797	0.000	0.043	0.000	0.001	0.091	0.636	0.549	0.182	0.002	0.024		10.633
EBS-18 Clinop	3	6.459	0.016	2.663	0.002	0.192	0.000	0.003	0.124	0.479	0.433	0.076	0.007	0.014		10.447
EBS-18 Clinop	4	7.300	0.022	1.782	0.001	0.155	0.000	0.003	0.098	0.233	0.262	0.121	0.009	0.034		9.978
EBS-18 Clinop	5	6.272	0.017	2.744	0.001	0.416	0.001	0.005	0.286	0.350	0.335	0.158	0.015	0.000		10.585
AVE.		**6.560**	**0.012**	**2.542**	**0.001**	**0.179**	**0.000**	**0.003**	**0.133**	**0.445**	**0.450**	**0.114**	**0.008**	**0.014**		**10.439**
Std Dev		**0.42**	**0.01**	**0.43**	**0.00**	**0.14**	**0.00**	**0.00**	**0.09**	**0.16**	**0.16**	**0.06**	**0.01**	**0.01**		**0.27**
ANALCIME																
EBS-18 Anl	1	67.08	0.03	20.90	0.00	0.66	0.00	0.00	0.16	3.91	1.10	0.03	0.02	0.23	-0.10	94.12
EBS-18 Anl	2	62.99	0.02	20.17	0.00	0.80	0.01	0.00	0.17	3.98	2.22	0.06	0.03	0.06	-0.03	90.50
EBS-18 Anl	4	64.68	0.09	20.56	0.00	0.33	0.01	0.02	0.07	4.65	1.67	0.19	0.01	0.00	0.00	92.29
EBS-18 Anl	5	62.40	0.03	19.92	0.00	0.33	0.00	0.01	0.04	4.92	0.62	0.21	0.02	0.00	0.00	88.51
AVE.		**64.29**	**0.04**	**20.39**	**0.00**	**0.53**	**0.00**	**0.01**	**0.11**	**4.37**	**1.40**	**0.12**	**0.02**	**0.07**	**-0.03**	**91.35**

Std Dev		**2.10**	**0.03**	**0.43**	**0.00**	**0.24**	**0.01**	**0.01**	**0.07**	**0.50**	**0.70**	**0.09**	**0.01**	**0.11**	**0.04**	**2.41**
	6 Atoms per formula unit (sum excludes F & Cl)															
		Si	**Ti**	**Al**	**Cr**	**Fe**	**Ni**	**Mn**	**Mg**	**Ca**	**Na**	**K**	**Cl**	**F**		**Sum**
EBS-18 Anl	1	2.271	0.001	0.834	0.000	0.019	0.000	0.000	0.008	0.142	0.072	0.001	0.001	0.024		3.348
EBS-18 Anl	2	2.236	0.000	0.844	0.000	0.024	0.000	0.000	0.009	0.151	0.153	0.003	0.002	0.007		3.420
EBS-18 Anl	4	2.244	0.002	0.841	0.000	0.010	0.000	0.001	0.003	0.173	0.112	0.009	0.001	0.000		3.394
EBS-18 Anl	5	2.250	0.001	0.847	0.000	0.010	0.000	0.000	0.002	0.190	0.043	0.010	0.001	0.000		3.352
AVE.		**2.250**	**0.001**	**0.841**	**0.000**	**0.015**	**0.000**	**0.000**	**0.006**	**0.164**	**0.095**	**0.006**	**0.001**	**0.008**		**3.379**
Std Dev		**0.02**	**0.00**	**0.01**	**0.00**	**0.01**	**0.00**	**0.00**	**0.00**	**0.02**	**0.05**	**0.00**	**0.00**	**0.01**		**0.03**
SAMPLE	**Pt#**	**SiO2**	**TiO2**	**Al2O3**	**Cr2O3**	**FeO**	**NiO**	**MnO**	**MgO**	**CaO**	**Na2O**	**K2O**	**Cl**	**F**	**O=Hal**	**TOTAL**
Fe-Oxides (Goethite)																
EBS-18 Alt-1	1	1.03	0.00	0.24	0.67	70.38	0.53	0.78	0.00	0.03	0.09	0.00	6.66	0.00	-1.50	80.41
EBS-18 Alt-2	1	0.51	0.01	0.69	0.35	77.51	0.09	0.81	0.06	0.21	2.72	0.07	0.07	0.00	-0.02	83.09
EBS-18 Alt-2	2	8.28	0.01	2.61	0.61	64.35	0.44	0.32	0.38	2.11	1.20	0.08	0.17	0.00	-0.04	80.56
EBS-18 Alt-3	1	8.35	0.01	2.72	0.67	68.62	0.50	0.55	0.59	3.35	0.92	0.09	0.13	0.06	-0.05	86.54
EBS-18 Alt-4	4	5.08	0.03	0.84	0.41	62.09	0.56	0.38	0.15	7.95	0.37	0.01	0.14	0.00	-0.03	78.00
AVE.		**4.65**	**0.01**	**1.42**	**0.54**	**68.59**	**0.43**	**0.57**	**0.24**	**2.73**	**1.06**	**0.05**	**1.43**	**0.01**	**-0.33**	**81.72**
Std Dev		**3.78**	**0.01**	**1.16**	**0.15**	**5.98**	**0.19**	**0.23**	**0.25**	**3.23**	**1.02**	**0.04**	**2.92**	**0.03**	**0.66**	**3.24**
	22 Atoms per formula unit (sum excludes F & Cl)															
		Si	**Ti**	**Al**	**Cr**	**Fe**	**Ni**	**Mn**	**Mg**	**Ca**	**Na**	**K**	**Cl**	**F**		**Sum**
EBS-18 Alt-1	1	0.357	0.000	0.099	0.184	20.442	0.149	0.231	0.000	0.009	0.063	0.000	3.919	0.000		21.534

EBS-18 Alt-2	1	0.156	0.003	0.253	0.086	20.017	0.023	0.212	0.026	0.069	1.626	0.028	0.036	0.000		22.499
EBS-18 Alt-2	2	2.265	0.002	0.841	0.133	14.727	0.097	0.074	0.156	0.619	0.637	0.027	0.079	0.000		19.578
EBS-18 Alt-3	1	2.136	0.002	0.820	0.135	14.684	0.103	0.118	0.226	0.919	0.456	0.028	0.056	0.046		19.626
EBS-18 Alt-4	4	1.510	0.006	0.294	0.096	15.445	0.134	0.095	0.068	2.534	0.211	0.004	0.071	0.000		20.396
AVE.		**1.285**	**0.003**	**0.461**	**0.127**	**17.063**	**0.101**	**0.146**	**0.095**	**0.830**	**0.599**	**0.017**	**0.832**	**0.009**		**20.727**
Std Dev		**0.98**	**0.00**	**0.35**	**0.04**	**2.91**	**0.05**	**0.07**	**0.09**	**1.03**	**0.62**	**0.01**	**1.73**	**0.02**		**1.27**
Fe interface																
Fe-saponite																
EBS-18 Alt-1	2	29.55	0.03	13.18	0.27	44.29	0.02	0.16	1.61	0.05	0.16	0.02	0.33	0.06	-0.10	89.74
EBS-18 Alt-1	3	29.13	0.05	12.46	0.17	42.98	0.03	0.23	1.50	0.06	0.20	0.03	0.06	0.03	-0.03	86.95
EBS-18 Alt-2	3	22.66	0.04	10.52	0.13	50.31	0.03	0.52	1.26	1.63	1.08	0.08	0.28	0.01	-0.07	88.55
EBS-18 Alt-2	4	24.77	0.02	12.14	0.00	47.06	0.01	0.33	1.35	0.32	0.38	0.07	0.16	0.00	-0.04	86.62
EBS-18 Alt-3	2	14.90	0.00	6.55	0.65	52.17	0.53	0.38	1.28	1.86	0.39	0.04	0.11	0.00	-0.03	78.86
EBS-18 Alt-3	3	14.73	0.02	6.49	0.48	58.08	0.42	0.39	1.29	0.87	0.42	0.06	0.11	0.00	-0.02	83.35
EBS-18 Alt-4	1	17.99	0.00	8.14	0.64	55.76	0.15	1.25	1.37	0.33	0.14	0.03	0.13	0.00	-0.03	85.93
EBS-18 Alt-4	2	30.95	0.01	13.67	0.04	37.48	0.02	0.22	2.53	0.69	0.02	0.02	0.13	0.02	-0.04	85.79
EBS-18 Alt-4	3	16.42	0.00	7.25	0.15	58.50	0.05	0.60	1.34	0.57	0.10	0.01	0.04	0.00	-0.01	85.03
EBS-18 Alt-6	1	16.79	0.01	7.58	0.45	55.51	0.33	0.64	1.05	1.78	1.56	0.08	0.12	0.00	-0.03	85.92
EBS-18 Alt-6	2	18.31	0.01	9.68	0.07	55.43	0.02	0.54	1.36	1.53	0.67	0.04	0.14	0.02	-0.04	87.80
EBS-18 Alt-6	3	20.59	0.00	10.68	0.03	51.95	0.02	0.40	1.73	1.15	0.43	0.09	0.07	0.00	-0.02	87.14
EBS-18 Alt-6	4	27.24	0.05	9.58	0.00	35.68	0.03	0.28	1.13	0.94	0.37	0.13	0.60	0.01	-0.14	76.03
AVE.		**21.85**	**0.02**	**9.84**	**0.24**	**49.63**	**0.13**	**0.46**	**1.45**	**0.91**	**0.45**	**0.05**	**0.17**	**0.01**	**-0.04**	**85.21**

Std Dev		**4.61**	**0.02**	**1.30**	**0.21**	**9.46**	**0.16**	**0.16**	**0.31**	**0.38**	**0.55**	**0.04**	**0.25**	**0.01**	**0.06**	**5.52**
	22 Atoms per formula unit (sum excludes F & Cl)															
Fe-saponite		**Si**	**Ti**	**Al**	**Cr**	**Fe**	**Ni**	**Mn**	**Mg**	**Ca**	**Na**	**K**	**Cl**	**F**		**Sum**
EBS-18 Alt-1	2	5.304	0.004	2.787	0.038	6.648	0.003	0.025	0.431	0.010	0.057	0.004	0.100	0.034		15.310
EBS-18 Alt-1	3	5.374	0.007	2.709	0.025	6.631	0.004	0.035	0.413	0.012	0.072	0.008	0.019	0.020		15.292
EBS-18 Alt-2	3	4.476	0.006	2.449	0.020	8.310	0.004	0.087	0.370	0.346	0.413	0.020	0.094	0.008		16.499
EBS-18 Alt-2	4	4.803	0.003	2.775	0.000	7.632	0.002	0.054	0.391	0.066	0.142	0.017	0.052	0.000		15.886
EBS-18 Alt-3	2	3.610	0.000	1.868	0.124	10.568	0.104	0.079	0.462	0.482	0.184	0.013	0.046	0.000		17.492
EBS-18 Alt-3	3	3.444	0.003	1.789	0.089	11.361	0.079	0.077	0.450	0.218	0.191	0.018	0.043	0.000		17.718
EBS-18 Alt-4	1	3.900	0.000	2.080	0.110	10.107	0.026	0.230	0.441	0.077	0.059	0.008	0.046	0.000		17.038
EBS-18 Alt-4	2	5.572	0.001	2.900	0.006	5.642	0.003	0.033	0.679	0.134	0.006	0.004	0.039	0.009		14.980
EBS-18 Alt-4	3	3.686	0.000	1.917	0.027	10.981	0.008	0.114	0.449	0.138	0.042	0.002	0.015	0.002		17.364
EBS-18 Alt-6	1	3.702	0.002	1.969	0.079	10.232	0.059	0.120	0.344	0.420	0.668	0.022	0.045	0.000		17.617
EBS-18 Alt-6	2	3.837	0.001	2.390	0.011	9.714	0.004	0.095	0.426	0.343	0.270	0.010	0.049	0.010		17.101
EBS-18 Alt-6	3	4.187	0.000	2.559	0.005	8.835	0.003	0.069	0.525	0.252	0.169	0.024	0.025	0.000		16.628
EBS-18 Alt-6	4	5.723	0.009	2.371	0.000	6.269	0.005	0.050	0.354	0.211	0.151	0.035	0.213	0.004		15.176
AVE.		**4.432**	**0.003**	**2.351**	**0.041**	**8.687**	**0.023**	**0.082**	**0.441**	**0.208**	**0.186**	**0.014**	**0.061**	**0.007**		**16.469**
Std Dev		**0.93**	**0.00**	**0.25**	**0.04**	**1.76**	**0.03**	**0.03**	**0.08**	**0.09**	**0.24**	**0.01**	**0.09**	**0.00**		**1.05**
STIPNOMELANE on iron strip																
EBS-18 Stilp	1	34.47	0.04	15.25	0.00	31.11	0.00	0.08	2.12	2.33	0.61	0.01	0.21	0.00	-0.05	86.22
EBS-18 Stilp	2	35.44	0.02	14.40	0.00	33.80	0.00	0.12	2.10	2.60	0.08	0.01	0.20	0.01	-0.05	88.79
EBS-18 Stilp	3	34.63	0.03	14.16	0.01	32.71	0.01	0.10	1.95	2.68	0.43	0.01	0.26	0.05	-0.08	87.03
EBS-18 Stilp	4	36.03	0.03	14.87	0.00	31.76	0.00	0.11	2.32	1.94	0.28	0.02	0.11	0.00	-0.02	87.47

EBS-18 Stilp	5	36.59	0.03	14.22	0.01	31.48	0.00	0.11	2.31	1.89	0.32	0.01	0.27	0.00	-0.06	87.24
Average		**35.43**	**0.03**	**14.58**	**0.01**	**32.17**	**0.00**	**0.10**	**2.16**	**2.29**	**0.34**	**0.01**	**0.21**	**0.01**	**-0.05**	**87.35**
Std Dev		**0.90**	**0.01**	**0.47**	**0.01**	**1.09**	**0.00**	**0.01**	**0.16**	**0.37**	**0.19**	**0.01**	**0.07**	**0.02**	**0.02**	**0.93**
	8 Atoms per formula unit (sum excludes F & Cl)															
		Si	**Ti**	**Al**	**Cr**	**Fe**	**Ni**	**Mn**	**Mg**	**Ca**	**Na**	**K**	**Cl**	**F**		**Sum**
EBS-18 Stilp	1	2.149	0.002	1.121	0.000	1.622	0.000	0.004	0.197	0.156	0.074	0.000	0.022	0.000		5.326
EBS-18 Stilp	2	2.169	0.001	1.039	0.000	1.730	0.000	0.006	0.192	0.170	0.010	0.000	0.021	0.002		5.316
EBS-18 Stilp	3	2.164	0.001	1.043	0.001	1.710	0.000	0.005	0.182	0.180	0.052	0.001	0.028	0.011		5.339
EBS-18 Stilp	4	2.202	0.001	1.072	0.000	1.624	0.000	0.006	0.212	0.127	0.033	0.001	0.011	0.000		5.278
EBS-18 Stilp	5	2.242	0.001	1.027	0.001	1.613	0.000	0.006	0.211	0.124	0.038	0.001	0.028	0.000		5.263
Average		**2.19**	**0.00**	**1.06**	**0.00**	**1.66**	**0.00**	**0.01**	**0.20**	**0.15**	**0.04**	**0.00**	**0.02**	**0.00**		**5.30**
Std Dev		**0.04**	**0.00**	**0.04**	**0.00**	**0.06**	**0.00**	**0.00**	**0.01**	**0.03**	**0.02**	**0.00**	**0.01**	**0.00**		**0.03**
SAMPLE	**Pt#**	**SiO2**	**TiO2**	**Al2O3**	**Cr2O3**	**FeO**	**NiO**	**MnO**	**MgO**	**CaO**	**Na2O**	**K2O**	**Cl**	**F**	**O=Hal**	**TOTAL**
EBS-18 Steel Alteration (transects)																
EBS-18 Alt-1	1	1.03	0.00	0.24	0.67	70.38	0.53	0.78	0.00	0.03	0.09	0.00	6.66	0.00	-1.50	80.41
EBS-18 Alt-1	2	29.55	0.03	13.18	0.27	44.29	0.02	0.16	1.61	0.05	0.16	0.02	0.33	0.06	-0.10	89.74
EBS-18 Alt-1	3	29.13	0.05	12.46	0.17	42.98	0.03	0.23	1.50	0.06	0.20	0.03	0.06	0.03	-0.03	86.95
Ave		**19.90**	**0.03**	**8.63**	**0.37**	**52.55**	**0.19**	**0.39**	**1.04**	**0.05**	**0.15**	**0.02**	**2.35**	**0.03**	**-0.54**	**85.70**
Std Dev		**16.35**	**0.03**	**7.27**	**0.26**	**15.45**	**0.29**	**0.34**	**0.90**	**0.02**	**0.05**	**0.02**	**3.73**	**0.03**	**0.83**	**4.79**
	22 Atoms per formula unit (sum excludes F & Cl)															
		Si	**Ti**	**Al**	**Cr**	**Fe**	**Ni**	**Mn**	**Mg**	**Ca**	**Na**	**K**	**Cl**	**F**		**Sum**
EBS-18 Alt-1	1	0.357	0.000	0.099	0.184	20.442	0.149	0.231	0.000	0.009	0.063	0.000	3.919	0.000		21.534
EBS-18 Alt-1	2	5.304	0.004	2.787	0.038	6.648	0.003	0.025	0.431	0.010	0.057	0.004	0.100	0.034		15.310
EBS-18 Alt-1	3	5.374	0.007	2.709	0.025	6.631	0.004	0.035	0.413	0.012	0.072	0.008	0.019	0.020		15.292
Ave		**3.68**	**0.00**	**1.87**	**0.08**	**11.24**	**0.05**	**0.10**	**0.28**	**0.01**	**0.06**	**0.00**	**1.35**	**0.02**		**17.38**

Std Dev		**2.88**	**0.00**	**1.53**	**0.09**	**7.97**	**0.08**	**0.12**	**0.24**	**0.00**	**0.01**	**0.00**	**2.23**	**0.02**		**3.60**
EBS-18 Alt-2	1	0.51	0.01	0.69	0.35	77.51	0.09	0.81	0.06	0.21	2.72	0.07	0.07	0.00	-0.02	83.09
EBS-18 Alt-2	2	8.28	0.01	2.61	0.61	64.35	0.44	0.32	0.38	2.11	1.20	0.08	0.17	0.00	-0.04	80.56
EBS-18 Alt-2	3	22.66	0.04	10.52	0.13	50.31	0.03	0.52	1.26	1.63	1.08	0.08	0.28	0.01	-0.07	88.55
EBS-18 Alt-2	4	24.77	0.02	12.14	0.00	47.06	0.01	0.33	1.35	0.32	0.38	0.07	0.16	0.00	-0.04	86.62
Ave		**14.05**	**0.02**	**6.49**	**0.27**	**59.81**	**0.14**	**0.49**	**0.76**	**1.07**	**1.34**	**0.07**	**0.17**	**0.00**	**-0.04**	**84.70**
Std Dev		**11.63**	**0.01**	**5.68**	**0.27**	**13.98**	**0.20**	**0.23**	**0.64**	**0.95**	**0.98**	**0.00**	**0.09**	**0.01**	**0.02**	**3.57**
	22 Atoms per formula unit (sum excludes F & Cl)															
		Si	**Ti**	**Al**	**Cr**	**Fe**	**Ni**	**Mn**	**Mg**	**Ca**	**Na**	**K**	**Cl**	**F**		**Sum**
EBS-18 Alt-2	1	0.156	0.003	0.253	0.086	20.017	0.023	0.212	0.026	0.069	1.626	0.028	0.036	0.000		22.499
EBS-18 Alt-2	2	2.265	0.002	0.841	0.133	14.727	0.097	0.074	0.156	0.619	0.637	0.027	0.079	0.000		19.578
EBS-18 Alt-2	3	4.476	0.006	2.449	0.020	8.310	0.004	0.087	0.370	0.346	0.413	0.020	0.094	0.008		16.499
EBS-18 Alt-2	4	4.803	0.003	2.775	0.000	7.632	0.002	0.054	0.391	0.066	0.142	0.017	0.052	0.000		15.886
Ave		**2.93**	**0.00**	**1.58**	**0.06**	**12.67**	**0.03**	**0.11**	**0.24**	**0.27**	**0.70**	**0.02**	**0.07**	**0.00**		**18.62**
Std Dev		**2.16**	**0.00**	**1.22**	**0.06**	**5.85**	**0.04**	**0.07**	**0.18**	**0.26**	**0.65**	**0.01**	**0.03**	**0.00**		**3.05**
EBS-18 Alt-3	1	8.35	0.01	2.72	0.67	68.62	0.50	0.55	0.59	3.35	0.92	0.09	0.13	0.06	-0.05	86.54
EBS-18 Alt-3	2	14.90	0.00	6.55	0.65	52.17	0.53	0.38	1.28	1.86	0.39	0.04	0.11	0.00	-0.03	78.86
EBS-18 Alt-3	3	14.73	0.02	6.49	0.48	58.08	0.42	0.39	1.29	0.87	0.42	0.06	0.11	0.00	-0.02	83.35
Ave		**12.66**	**0.01**	**5.25**	**0.60**	**59.62**	**0.49**	**0.44**	**1.05**	**2.03**	**0.58**	**0.06**	**0.12**	**0.02**	**-0.03**	**82.92**
Std Dev		**3.73**	**0.01**	**2.19**	**0.10**	**8.33**	**0.06**	**0.09**	**0.40**	**1.25**	**0.30**	**0.02**	**0.01**	**0.03**	**0.02**	**3.86**
	22 Atoms per formula unit (sum excludes F & Cl)															
		Si	**Ti**	**Al**	**Cr**	**Fe**	**Ni**	**Mn**	**Mg**	**Ca**	**Na**	**K**	**Cl**	**F**		**Sum**
EBS-18 Alt-3	1	2.136	0.002	0.820	0.135	14.684	0.103	0.118	0.226	0.919	0.456	0.028	0.056	0.046		19.626
EBS-18 Alt-3	2	3.610	0.000	1.868	0.124	10.568	0.104	0.079	0.462	0.482	0.184	0.013	0.046	0.000		17.492

EBS-18 Alt-3	3	3.444	0.003	1.789	0.089	11.361	0.079	0.077	0.450	0.218	0.191	0.018	0.043	0.000		17.718
Ave		**3.06**	**0.00**	**1.49**	**0.12**	**12.20**	**0.10**	**0.09**	**0.38**	**0.54**	**0.28**	**0.02**	**0.05**	**0.02**		**18.28**
Std Dev		**0.81**	**0.00**	**0.58**	**0.02**	**2.18**	**0.01**	**0.02**	**0.13**	**0.35**	**0.16**	**0.01**	**0.01**	**0.03**		**1.17**
EBS-18 Alt-4	1	17.99	0.00	8.14	0.64	55.76	0.15	1.25	1.37	0.33	0.14	0.03	0.13	0.00	-0.03	85.93
EBS-18 Alt-4	2	30.95	0.01	13.67	0.04	37.48	0.02	0.22	2.53	0.69	0.02	0.02	0.13	0.02	-0.04	85.79
EBS-18 Alt-4	3	16.42	0.00	7.25	0.15	58.50	0.05	0.60	1.34	0.57	0.10	0.01	0.04	0.00	-0.01	85.03
EBS-18 Alt-4	4	5.08	0.03	0.84	0.41	62.09	0.56	0.38	0.15	7.95	0.37	0.01	0.14	0.00	-0.03	78.00
Ave		**17.61**	**0.01**	**7.47**	**0.31**	**53.46**	**0.19**	**0.61**	**1.35**	**2.39**	**0.15**	**0.02**	**0.11**	**0.00**	**-0.03**	**83.69**
Std Dev		**10.59**	**0.01**	**5.26**	**0.27**	**10.96**	**0.25**	**0.45**	**0.97**	**3.71**	**0.15**	**0.01**	**0.05**	**0.01**	**0.01**	**3.81**
	22 Atoms per formula unit (sum excludes F & Cl)															
		Si	**Ti**	**Al**	**Cr**	**Fe**	**Ni**	**Mn**	**Mg**	**Ca**	**Na**	**K**	**Cl**	**F**		**Sum**
EBS-18 Alt-4	1	3.900	0.000	2.080	0.110	10.107	0.026	0.230	0.441	0.077	0.059	0.008	0.046	0.000		17.038
EBS-18 Alt-4	2	5.572	0.001	2.900	0.006	5.642	0.003	0.033	0.679	0.134	0.006	0.004	0.039	0.009		14.980
EBS-18 Alt-4	3	3.686	0.000	1.917	0.027	10.981	0.008	0.114	0.449	0.138	0.042	0.002	0.015	0.002		17.364
EBS-18 Alt-4	4	1.510	0.006	0.294	0.096	15.445	0.134	0.095	0.068	2.534	0.211	0.004	0.071	0.000		20.396
Ave		**3.67**	**0.00**	**1.80**	**0.06**	**10.54**	**0.04**	**0.12**	**0.41**	**0.72**	**0.08**	**0.00**	**0.04**	**0.00**		**17.44**
Std Dev		**1.67**	**0.00**	**1.09**	**0.05**	**4.02**	**0.06**	**0.08**	**0.25**	**1.21**	**0.09**	**0.00**	**0.02**	**0.00**		**2.23**
EBS-18 Alt-5	1	11.80	0.02	4.57	0.68	62.53	0.34	1.11	0.96	0.70	0.44	0.03	0.24	0.04	-0.07	83.46
EBS-18 Alt-5	2	49.89	0.16	14.91	0.04	20.43	0.01	0.16	2.25	0.51	0.27	1.53	0.23	0.03	-0.07	90.41
EBS-18 Alt-5	3	42.21	0.63	22.20	0.00	16.20	0.00	0.15	2.84	0.47	0.14	3.47	0.13	0.17	-0.10	88.63
Ave		**34.63**	**0.27**	**13.89**	**0.24**	**33.05**	**0.12**	**0.48**	**2.02**	**0.56**	**0.29**	**1.68**	**0.20**	**0.08**	**-0.08**	**87.50**
Std Dev		**20.14**	**0.32**	**8.86**	**0.38**	**25.62**	**0.19**	**0.55**	**0.96**	**0.12**	**0.15**	**1.73**	**0.06**	**0.08**	**0.02**	**3.61**
	22 Atoms per formula unit (sum excludes F & Cl)															
		Si	**Ti**	**Al**	**Cr**	**Fe**	**Ni**	**Mn**	**Mg**	**Ca**	**Na**	**K**	**Cl**	**F**		**Sum**
EBS-18 Alt-5	1	2.928	0.004	1.337	0.134	12.975	0.068	0.234	0.355	0.185	0.213	0.008	0.100	0.030		18.443

EBS-18 Alt-5	2	7.377	0.017	2.599	0.005	2.526	0.001	0.020	0.496	0.081	0.078	0.288	0.057	0.016		13.487
EBS-18 Alt-5	3	6.388	0.072	3.958	0.000	2.049	0.000	0.020	0.642	0.077	0.042	0.670	0.034	0.082		13.918
Ave		**5.56**	**0.03**	**2.63**	**0.05**	**5.85**	**0.02**	**0.09**	**0.50**	**0.11**	**0.11**	**0.32**	**0.06**	**0.04**		**15.28**
Std Dev		**2.34**	**0.04**	**1.31**	**0.08**	**6.18**	**0.04**	**0.12**	**0.14**	**0.06**	**0.09**	**0.33**	**0.03**	**0.04**		**2.75**
EBS-18 Alt-6	1	16.79	0.01	7.58	0.45	55.51	0.33	0.64	1.05	1.78	1.56	0.08	0.12	0.00	-0.03	85.92
EBS-18 Alt-6	2	18.31	0.01	9.68	0.07	55.43	0.02	0.54	1.36	1.53	0.67	0.04	0.14	0.02	-0.04	87.80
EBS-18 Alt-6	3	20.59	0.00	10.68	0.03	51.95	0.02	0.40	1.73	1.15	0.43	0.09	0.07	0.00	-0.02	87.14
EBS-18 Alt-6	4	27.24	0.05	9.58	0.00	35.68	0.03	0.28	1.13	0.94	0.37	0.13	0.60	0.01	-0.14	76.03
Ave		**20.73**	**0.02**	**9.38**	**0.14**	**49.64**	**0.10**	**0.46**	**1.32**	**1.35**	**0.76**	**0.08**	**0.23**	**0.01**	**-0.05**	**84.22**
Std Dev		**4.61**	**0.02**	**1.30**	**0.21**	**9.46**	**0.16**	**0.16**	**0.31**	**0.38**	**0.55**	**0.04**	**0.25**	**0.01**	**0.06**	**5.52**
	22 Atoms per formula unit (sum excludes F & Cl)															
		Si	**Ti**	**Al**	**Cr**	**Fe**	**Ni**	**Mn**	**Mg**	**Ca**	**Na**	**K**	**Cl**	**F**		**Sum**
EBS-18 Alt-6	1	3.702	0.002	1.969	0.079	10.232	0.059	0.120	0.344	0.420	0.668	0.022	0.045	0.000		17.617
EBS-18 Alt-6	2	3.837	0.001	2.390	0.011	9.714	0.004	0.095	0.426	0.343	0.270	0.010	0.049	0.010		17.101
EBS-18 Alt-6	3	4.187	0.000	2.559	0.005	8.835	0.003	0.069	0.525	0.252	0.169	0.024	0.025	0.000		16.628
EBS-18 Alt-6	4	5.723	0.009	2.371	0.000	6.269	0.005	0.050	0.354	0.211	0.151	0.035	0.213	0.004		15.176
Ave		**4.36**	**0.00**	**2.32**	**0.02**	**8.76**	**0.02**	**0.08**	**0.41**	**0.31**	**0.31**	**0.02**	**0.08**	**0.00**		**16.63**
Std Dev		**0.93**	**0.00**	**0.25**	**0.04**	**1.76**	**0.03**	**0.03**	**0.08**	**0.09**	**0.24**	**0.01**	**0.09**	**0.00**		**1.05**

Appendix E

SEM images EBS-18

Copper and Steel corrosion images

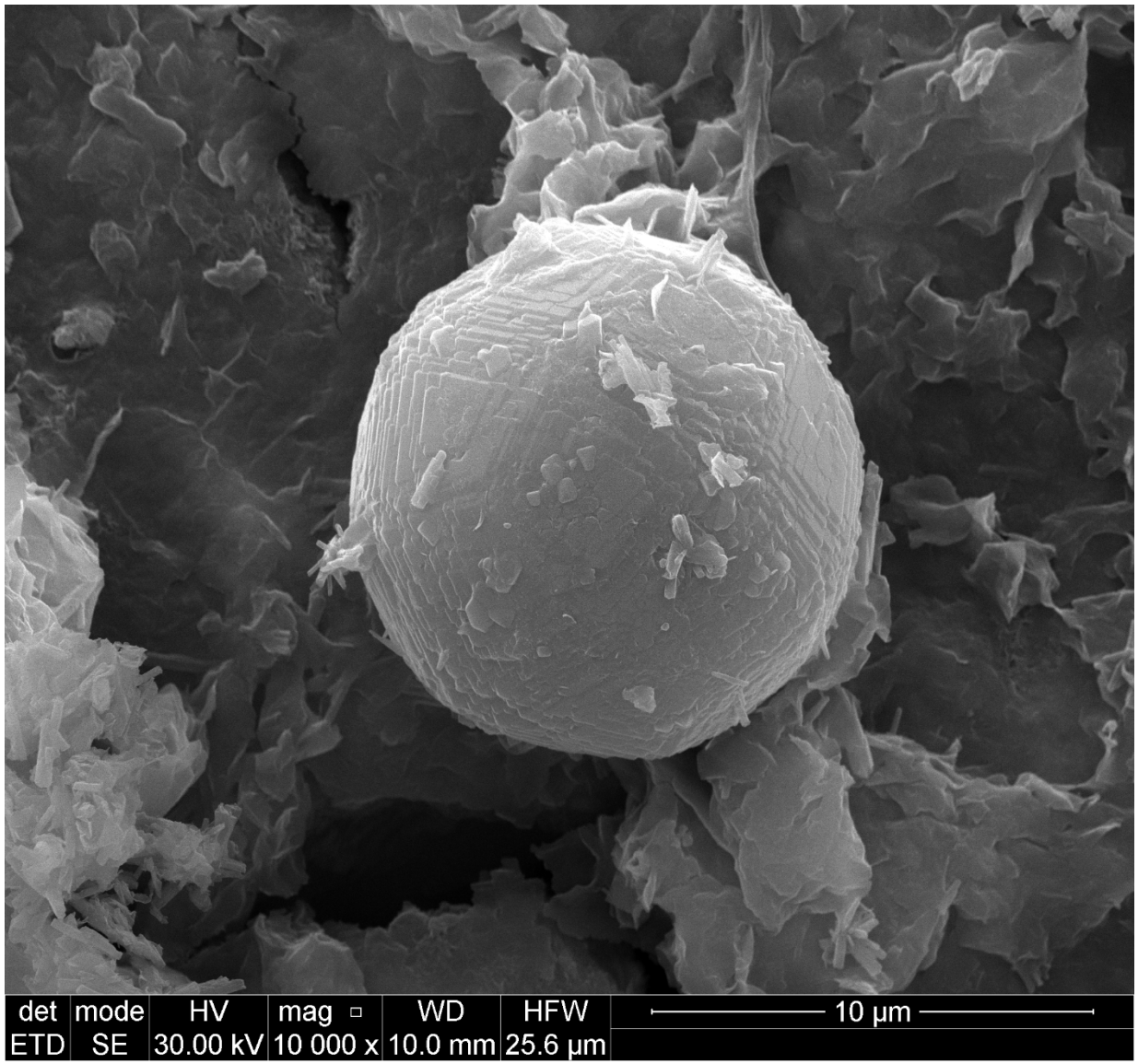

Figure E.1. Analcime – Wairakite zeolite in smectite matrix.

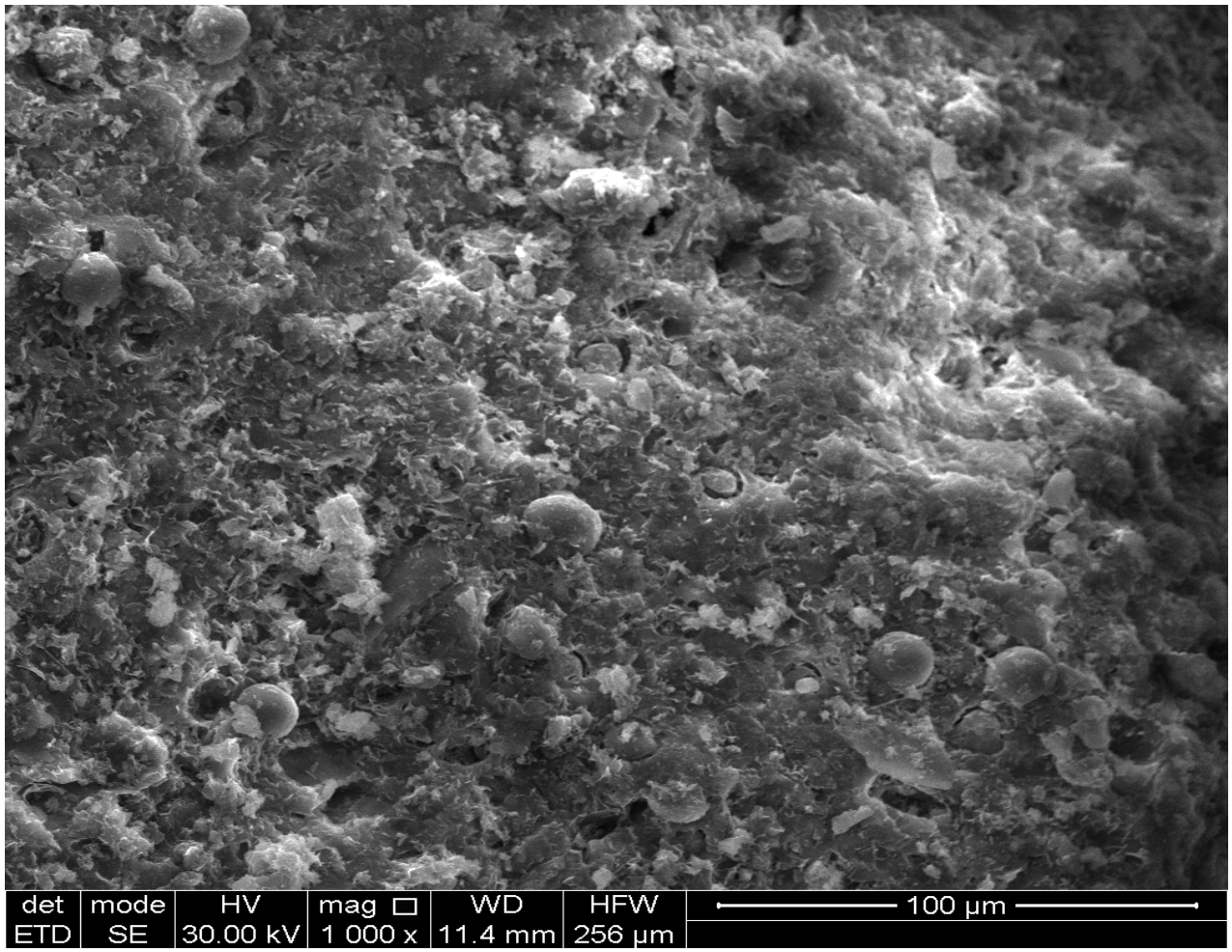

Figure E.2 Analcime – wairakite embedded in smectite groundmass**.**

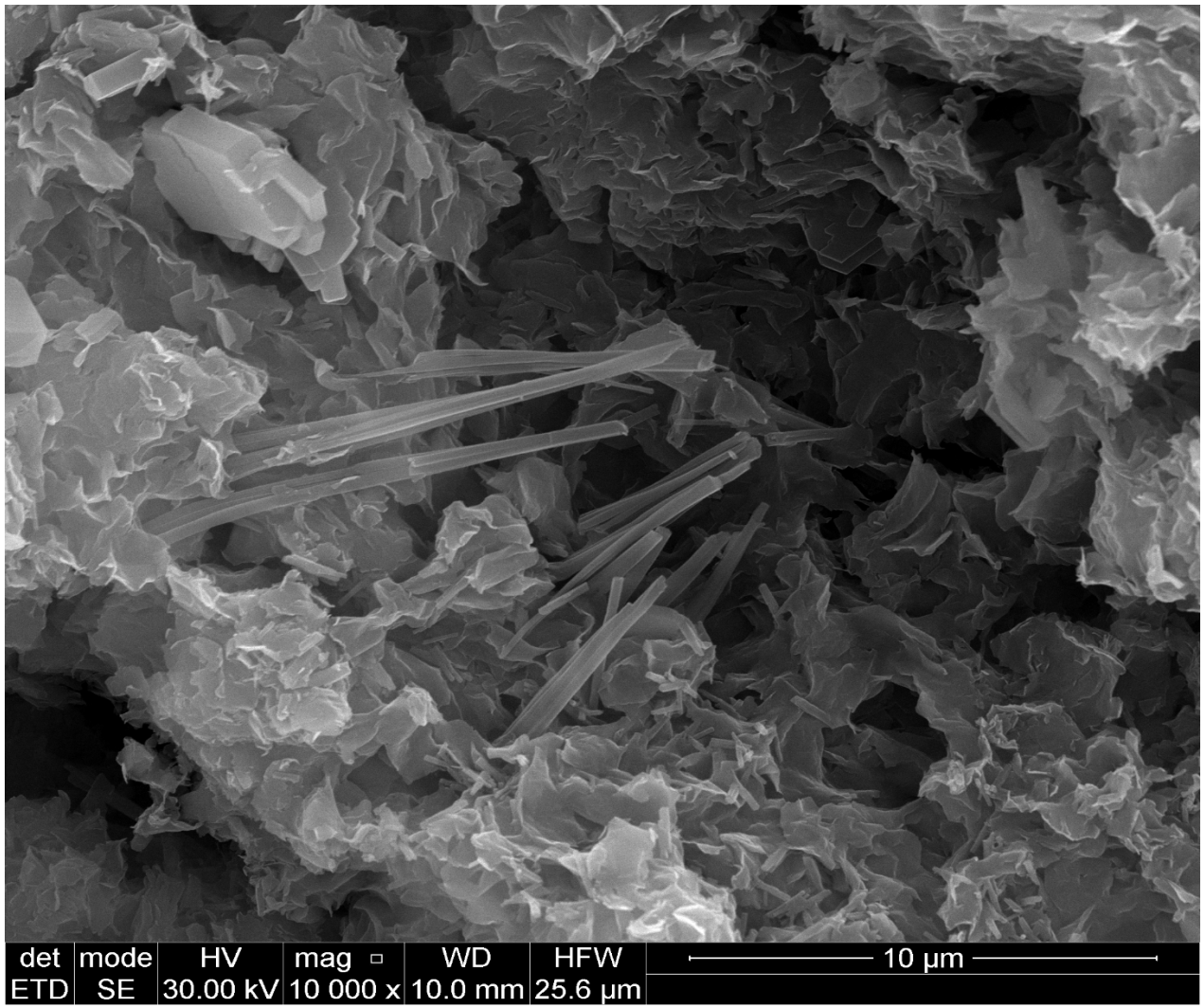

Figure E.3. Acicular clinoptilolite in smectite

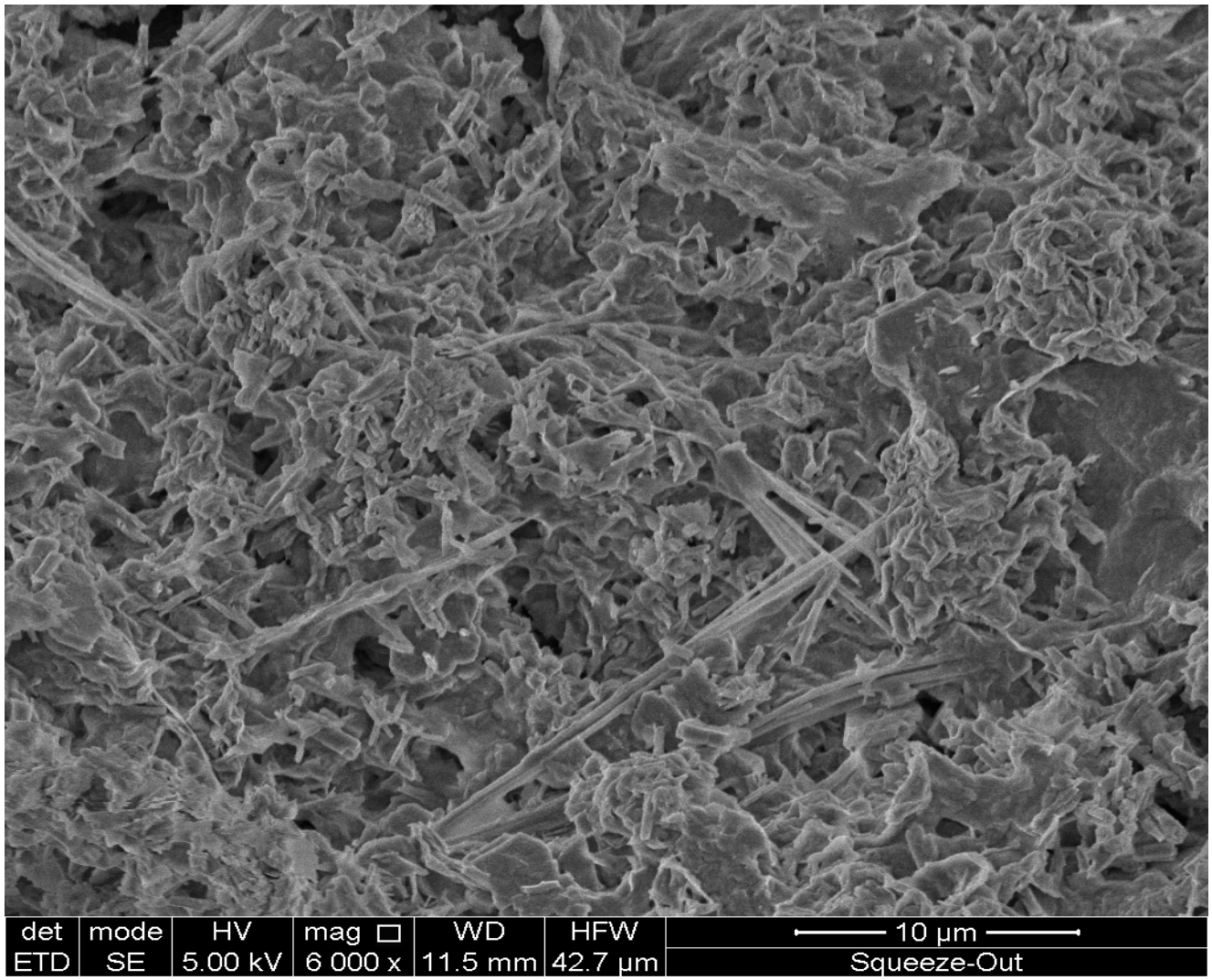

Figure E.4. Fibrous clinoptilolite and smectite

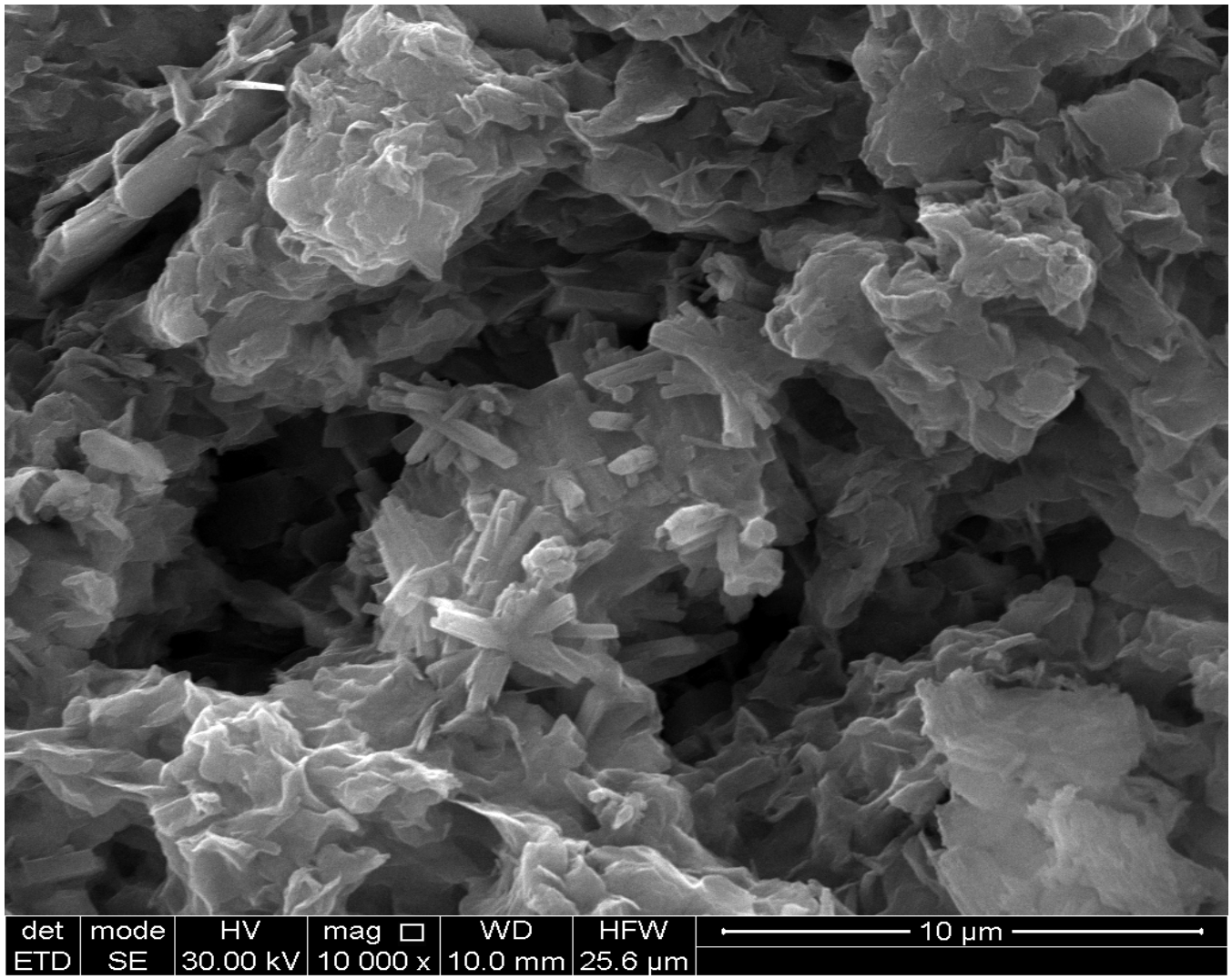

Figure E.5. Radial growth authigenic plagioclase

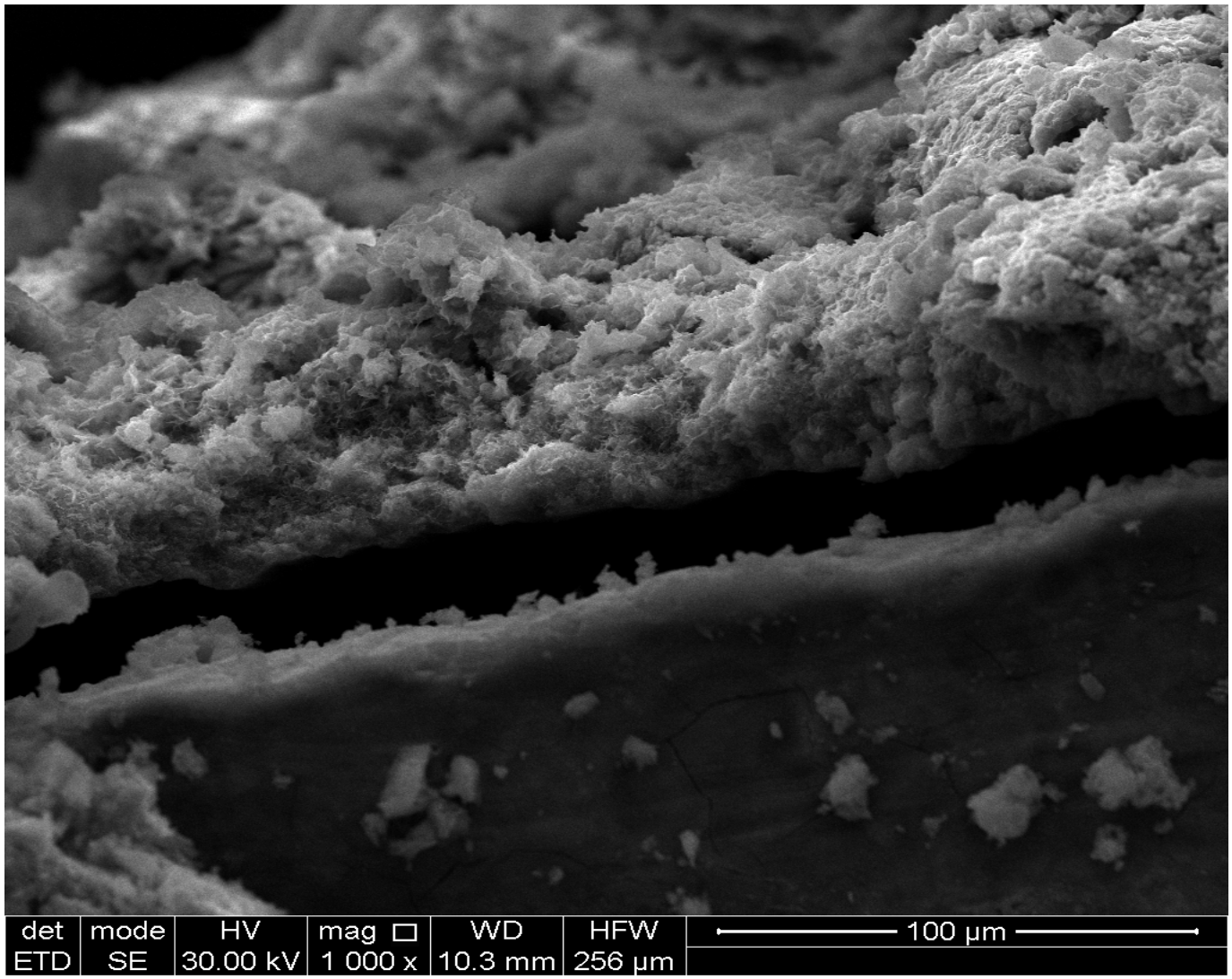

Figure E.6. Fe-saponite (fine grained material above black zone) grown on low carbon steel (lower grey mass).

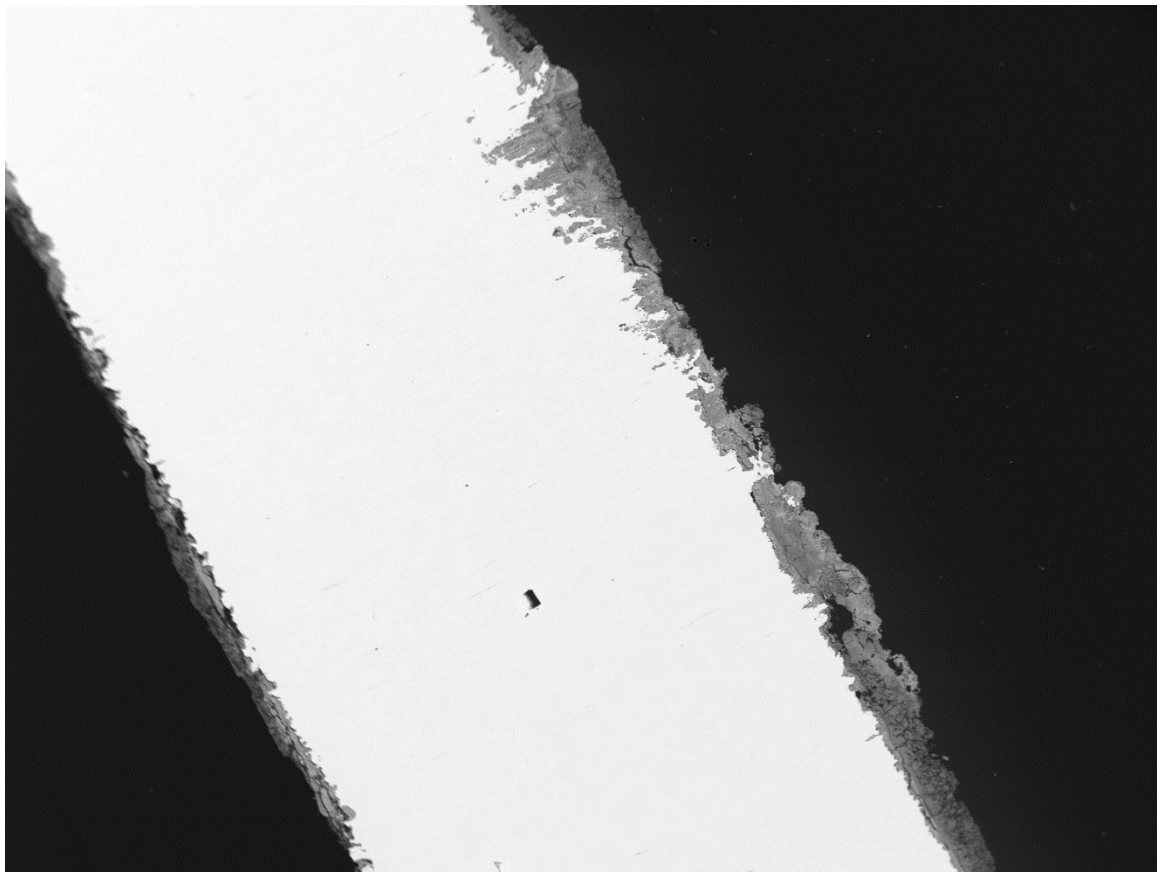

Figure E.7. Note abundant pit corrosion in upper right region of low carbon steel sample.

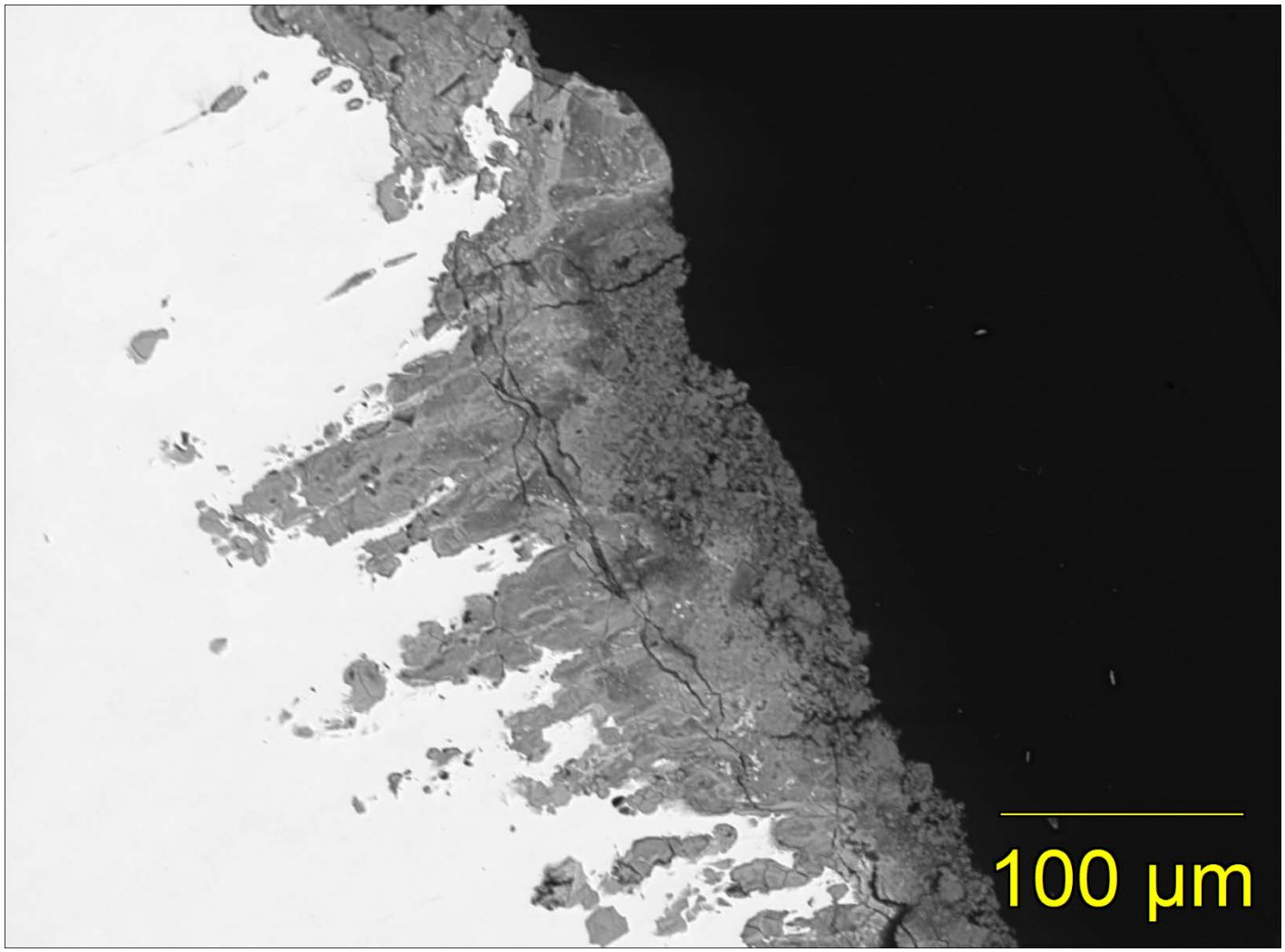

Figure E.8. Pit corrosion of low carbon steel in experiment EBS-18. Depth exceeds 100 micron maximum and width is approximately 50 micron.

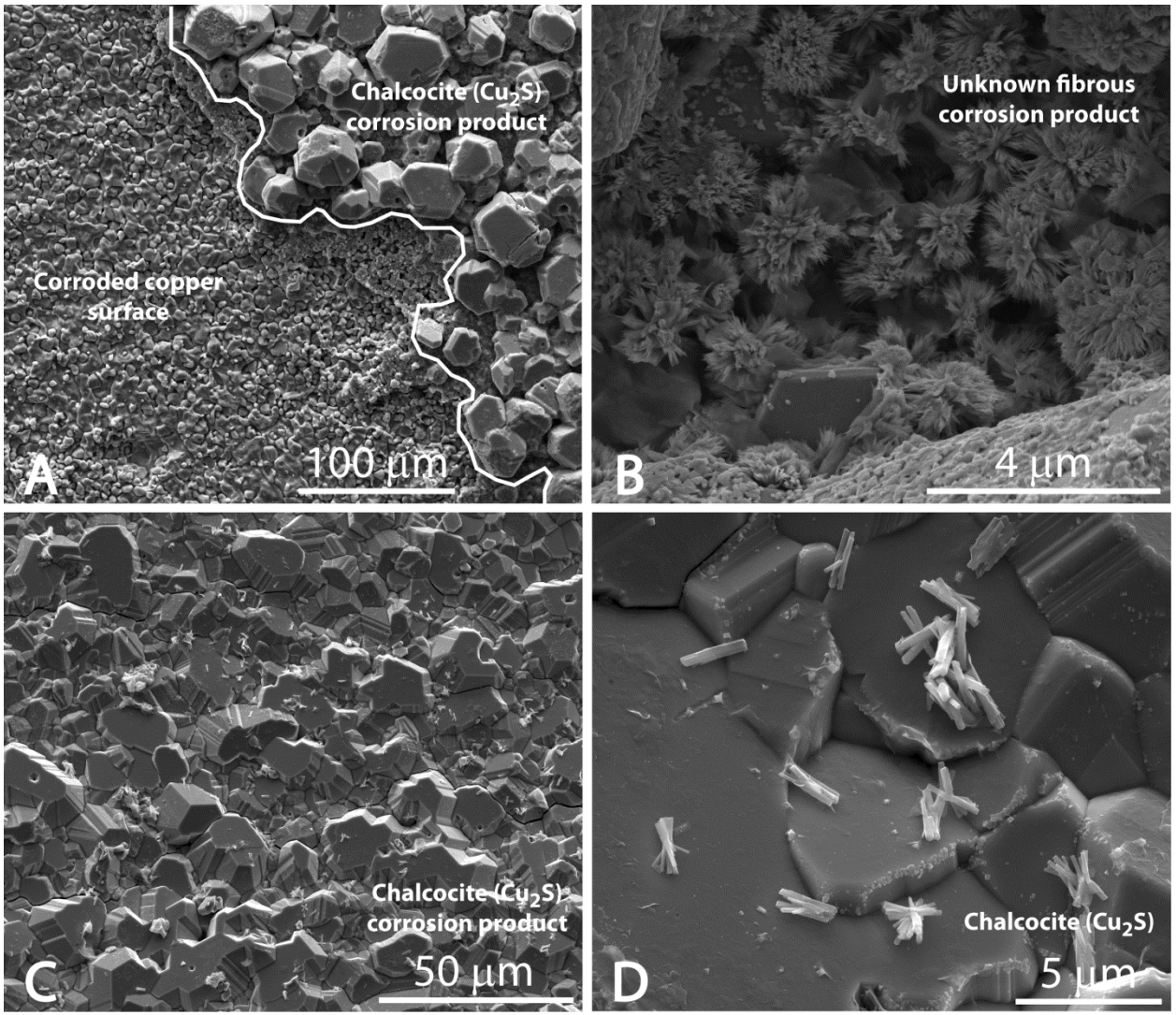

Figure E.9. SEM image (plan view) of copper surface showing corroded copper surfaces and various interface reaction products from both ramped (EBS-4) and isothermal, 300°C (EBS-8) heating profiles. A) Boundary between the corroded copper surface and chalcocite (Cu_2S) from EBS-4. B) Unknown fibers occurring on the copper surface in between chalcocite growths from EBS-4. These fibers might be a late-stage oxide or chloride corrosion product upon depletion of sulfide. C) Intergrown chalcocite from EBS-8. D) Atacamite (orthorhombic laths) resting on top of chalcocite crystals. Their growth is due to late stage scavenging of Cl from the brine.

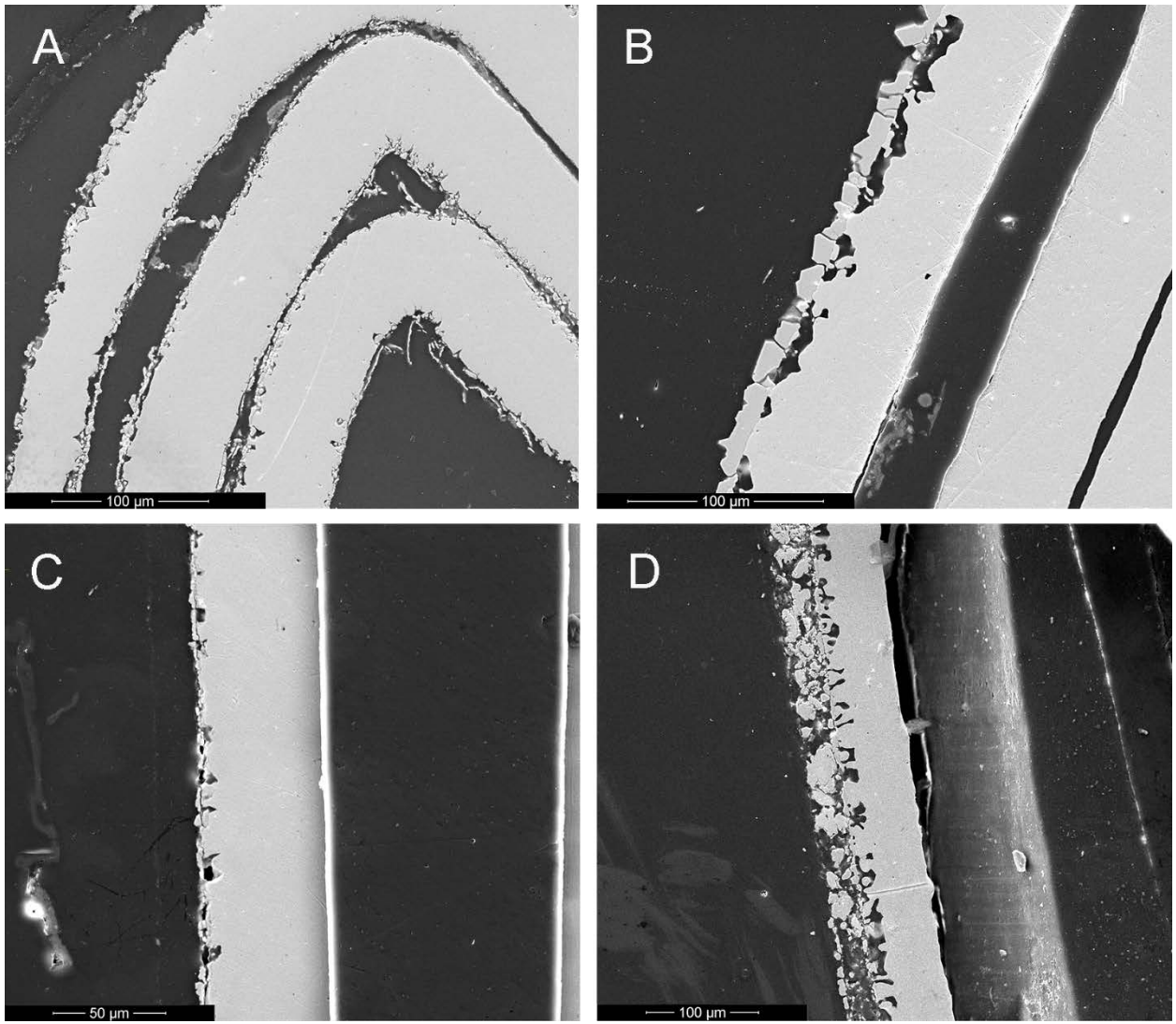

Figure E.10. SEM images from runs EBS-4 (A), EBS-11 (B), EBS-16 (C) and EBS-17(D). The overall thicknesses of the copper foils are ~ 63 µm. Surfaces within the rolled copper foil were relatively protected from sulfide attack.

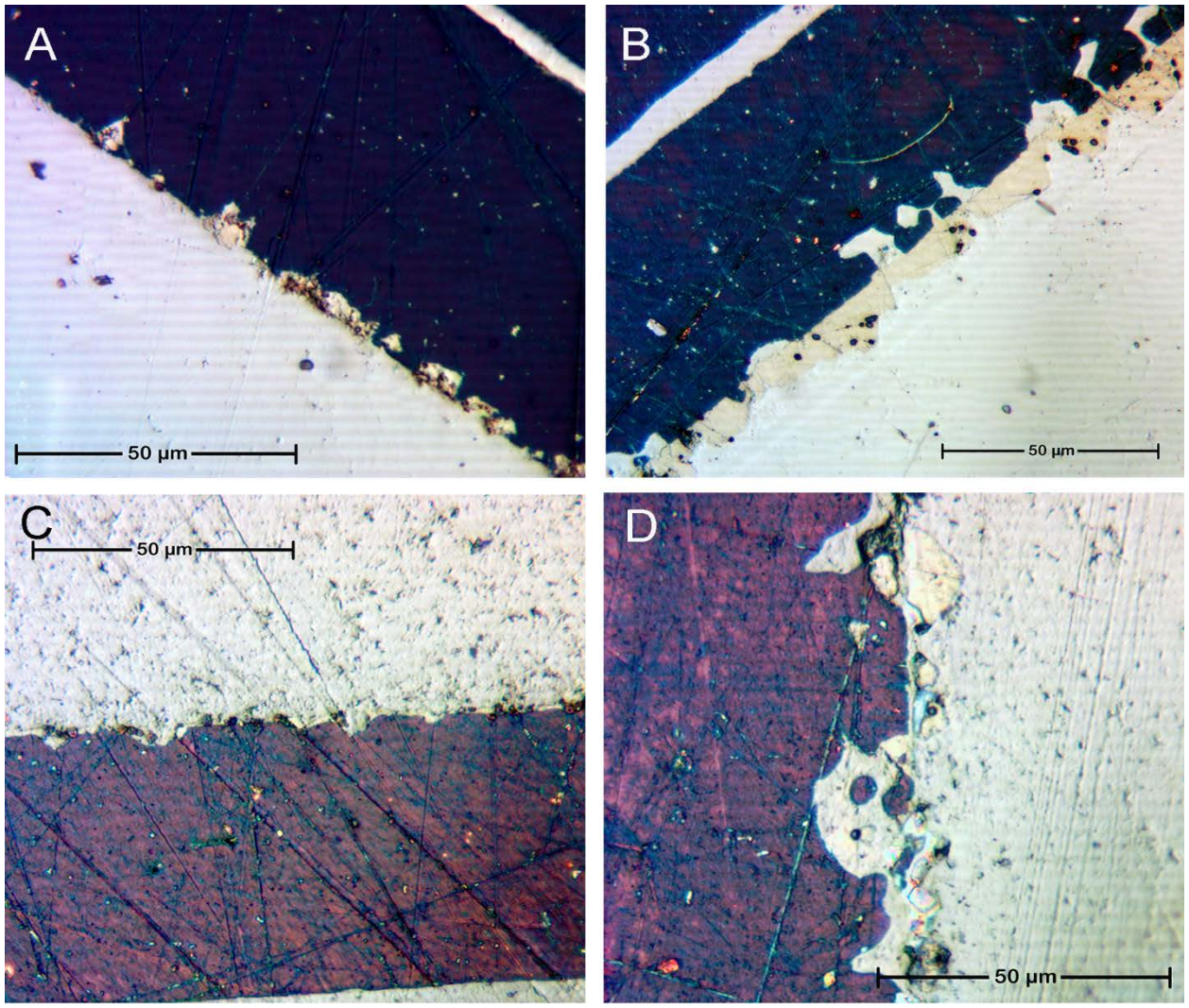

Figure E.11. Reflected light images of Cu corrosion. EBS-4 (A), EBS-11 (B), EBS-16 (C) and EBS-17 (D) with chalcocite layer (pale yellow). Copper color for images A and B, dark blue/black, images C and D, orange brown.

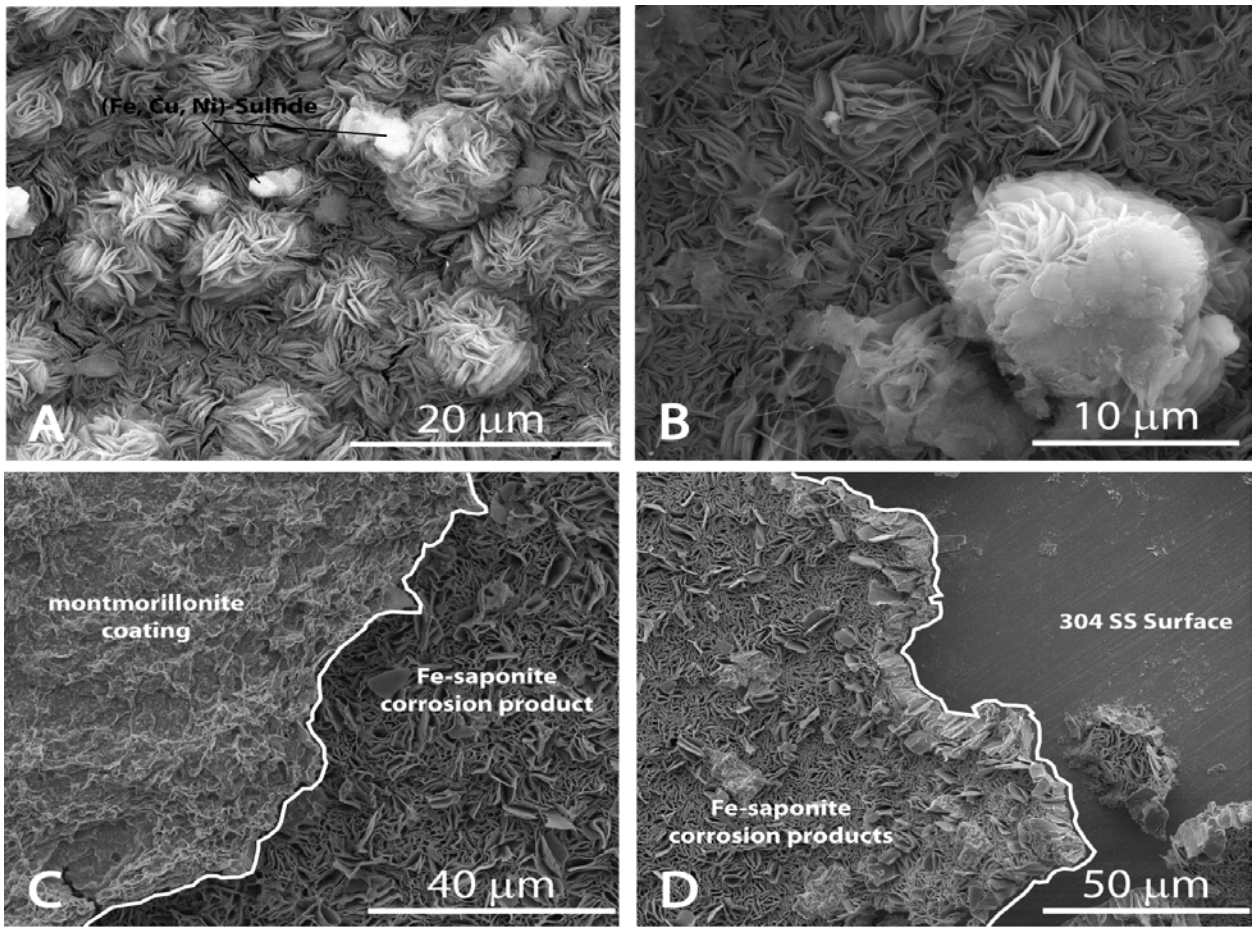

Figure E.12. SEM image (plan view) of Fe-phyllosilicates (saponite and chlorite) using 304 SS as a growth substrate from both ramped (EBS-2) and isothermal, 300°C (EBS-5) heating profiles. A) Fe-saponite and chlorite growths with later-stage pentlandite-like ((Fe, Cu, Ni)-sulfide) material from EBS-2. B) Unknown fibers overlaying rose-like Fe-saponite and chlorite interface reaction products from EBS-2. C) Montmorillonite coating on Fe-saponite showing the distinct morphology between the two smectites from EBS-5. D) Boundary between the Fe-saponite interface reaction product and 304 SS surface from EBS-5.

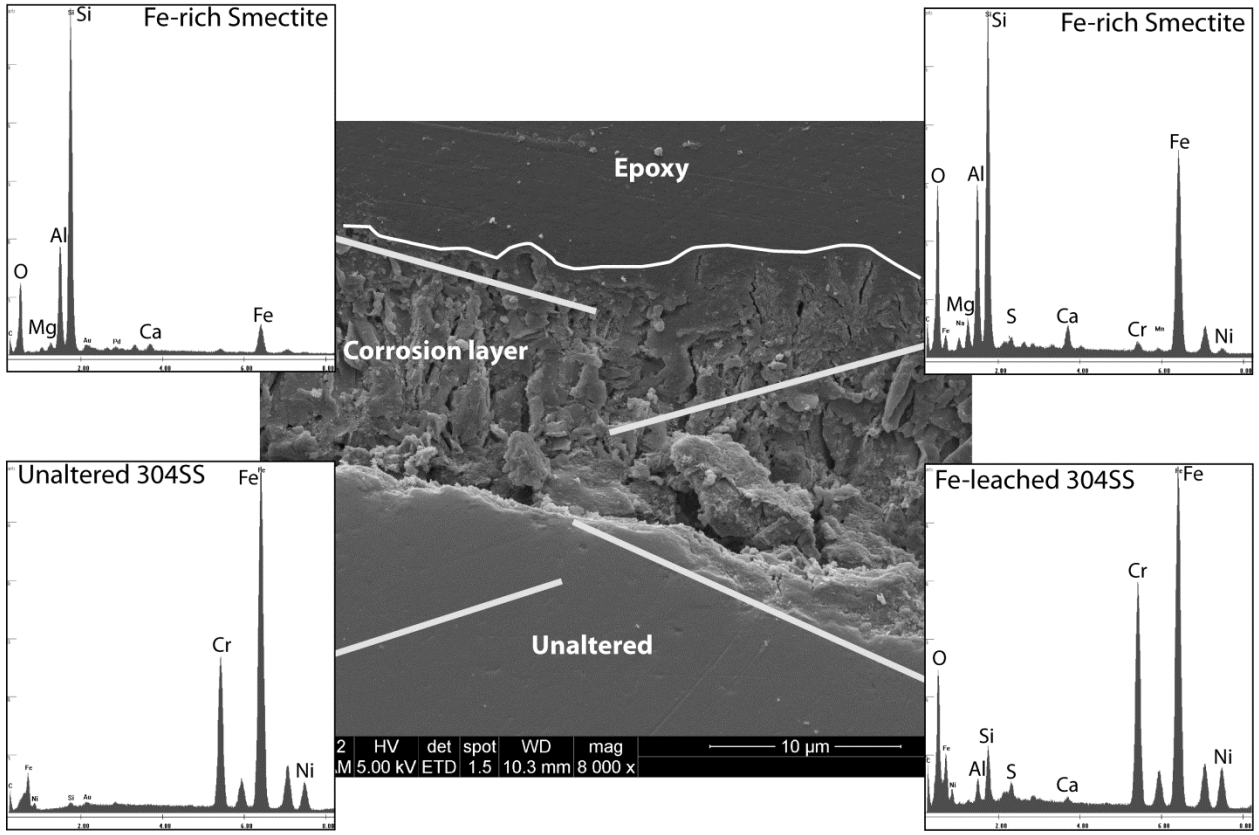

Figure E.13. SEM image of 304 SS cross-section showing Fe-saponite interface reaction products using steel surface as a growth substrate. EDX analyses of post-reaction 304SS and interface reaction products indicates Fe is leached from the 304SS forming a slightly Cr-enriched steel outer layer and an Fe-rich aluminosilicate (Fe-saponite/chlorite) coating. Uniform corrosion of the 304SS does not appear to develop significant incongruent dissolution.

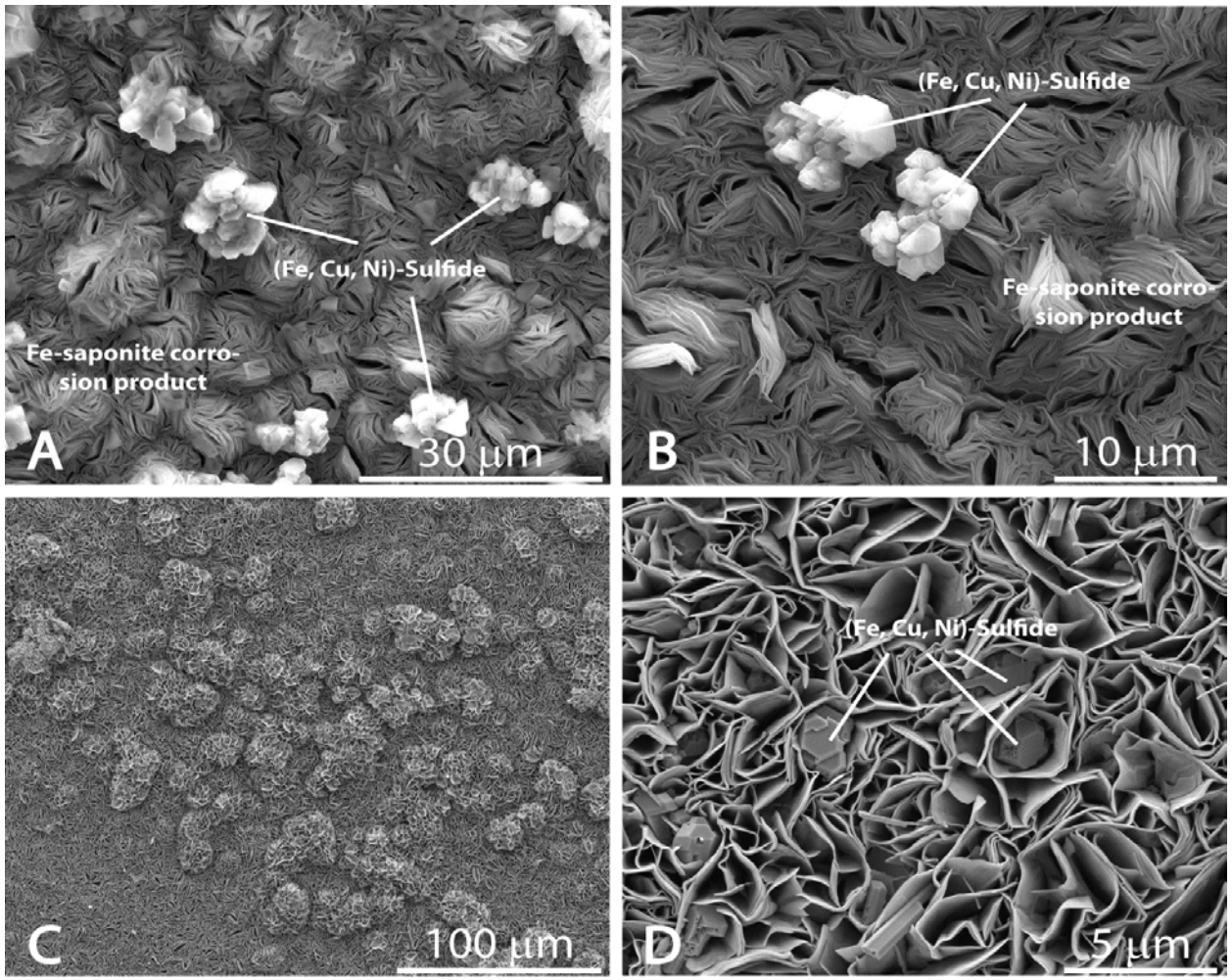

Figure E.14. SEM image (plan view) of Fe-saponite using 316SS as a growth substrate from both ramped (EBS-3) and isothermal, 300°C (EBS-10) heating profiles. A) Dense growth of Fe-saponite and chlorite with late-stage pentlandite-like ((Fe, Cu, Ni)-sulfide) material from EBS-3. B) Close-up of pentlandite-like ((Fe, Cu, Ni)-sulfide) material on Fe-phyllosilicates from EBS-3. C) Honeycomb and rose-like textures associated with Fe-saponite interface reaction products from EBS-10. D) Fe-saponite rose-like texture with pentlandite-like materials occurring between Fe-saponite foils from EBS-10.

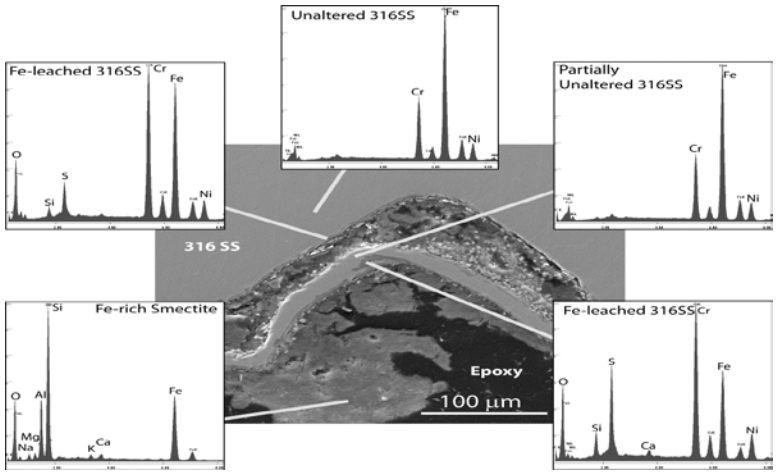

Figure E.15. SEM (secondary electron) image of 316SS cross-section showing Fe-saponite/chlorite growth due to exfoliation corrosion from EBS-3. Chemical analyses of post-reaction 316SS and interface reaction products indicates there was significant Fe leaching from the 316SS forming a Cr-enriched steel outer layer up to 4 µm thick.

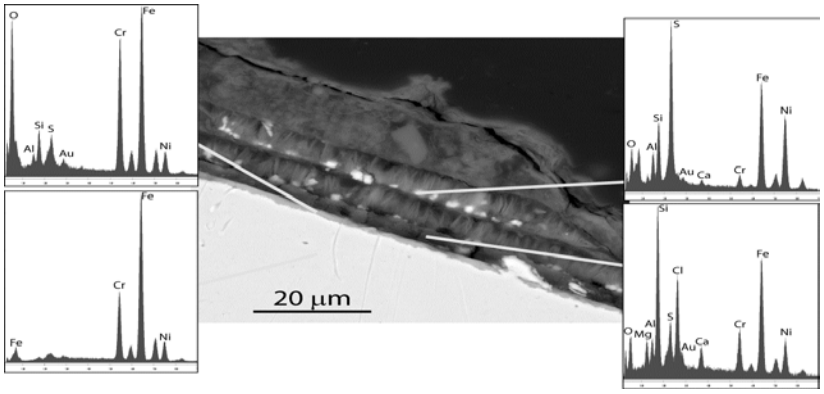

Figure E.16. SEM (back scatter) image of 316SS cross-section showing Fe-saponite/chlorite growth due to exfoliation corrosion from EBS-3. Chemical analyses of post-reaction 316SS and interface reaction products indicates there was significant Fe leaching from the 316SS forming a Cr-enriched steel outer layer up to 4 µm thick.

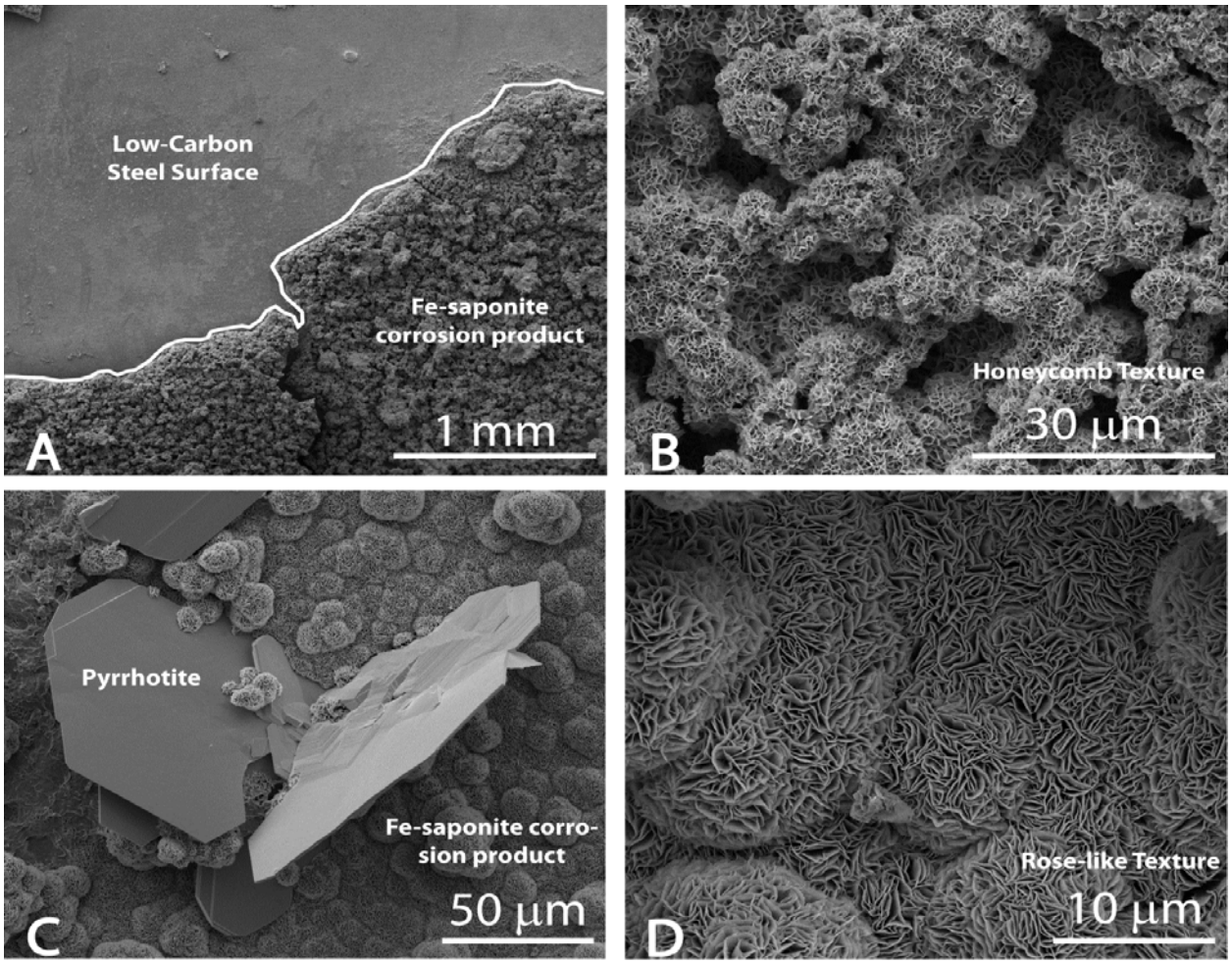

Figure E.17. SEM image (plan view) of Fe-saponite growth on low-carbon steel from the ramped (EBS-6) heating experiment. A) Boundary between the Fe-saponite interface reaction product and low-carbon steel surface. B) Honeycombed Fe-saponite. C) Botryoidal Fe-saponite interface reaction product with pyrrhotite platelets from EBS-6. D) Rose-like texture of Fe-saponite.

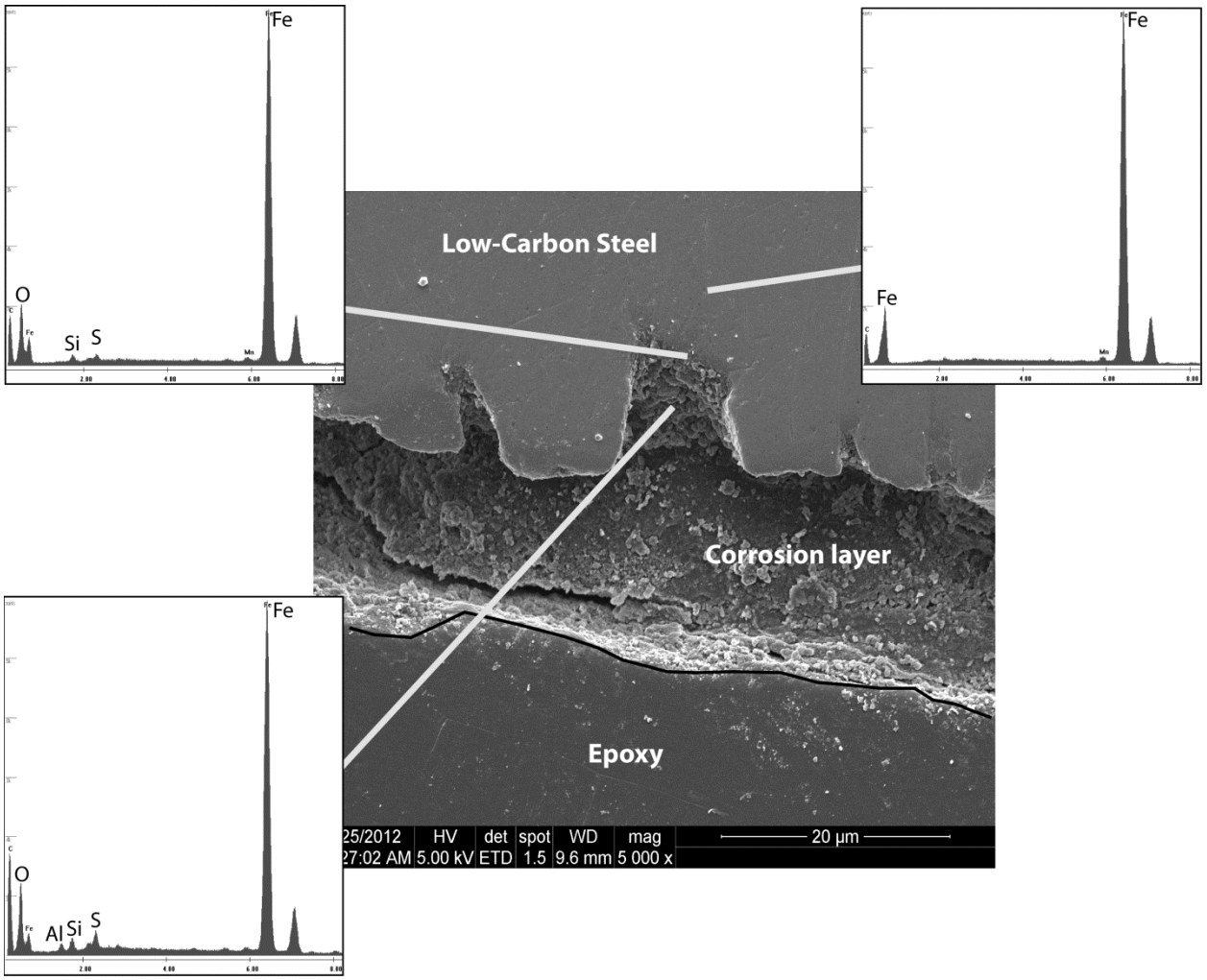

Figure E 18. SEM image of low-carbon steel cross-section showing Fe-saponite reaction products using steel surface as a growth substrate. EDX analyses of post-reaction low-carbon steel and interface reaction n surfaces show a slight oxidation and sulfidation of the surface (probably due to oxide and sulfide precipitates). EDX composition of the reaction product was not collected due to erosion of Fe-saponite during sample preparation. Extensive pitting corrosion of the low-carbon steel occurs during the ramped experiments (EBS-6).

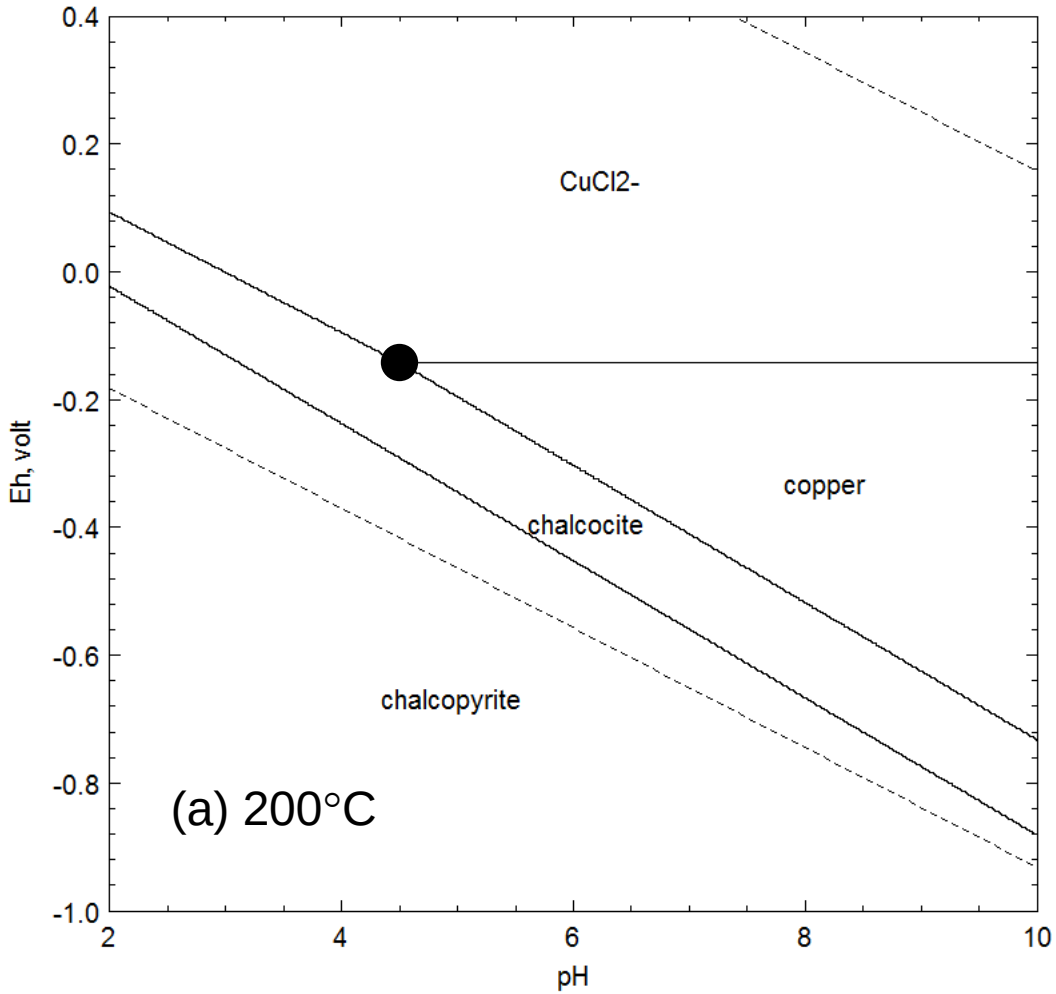
0.4
0.2
0.0
-0.2
-0.4
-0.6
-0.8
-1.0
Eh, volt
2
4
6
8
10
pH
CuCl2-
copper
chalcocite
chalcopyrite
(a) 200°C

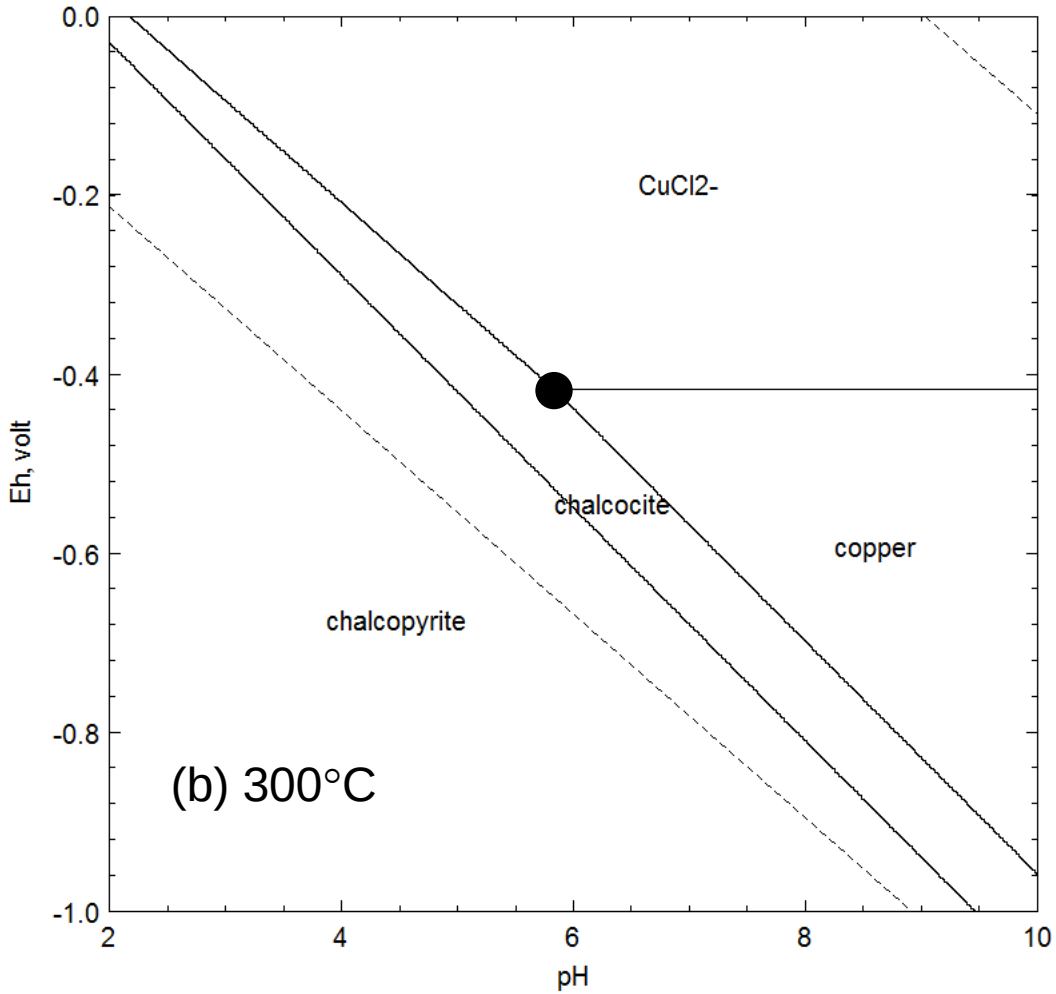

Figure E.19. Eh-pH diagram for the Cu-S-Cl-H_2O system at (a) 200 and (b) 300°C (see text). Dotted lines denote the stability of H_2O. The black dot represent the invariant points for copper-$Cu_2S_{(s)}$- $CuCl_2^-$ equilibrium

Appendix F
Miscellaneous tables

	Chalcocite Thickness (um)	Pit Depth (um)	Corrosion rate (um/day)
EBS-4	3.0(0.1)	5.7(0.2)	0.16(0.6)
EBS-11	8.2(0.4)	13.5(0.6)	0.32(0.2)
EBS-16	2.6(0.1)	4.3(10.)	0.024(0.01)
EBS-17	5.6(0.4)	13.1(0.6)	0.31(0.1)

Table F.1. Chalcocite thickness, pit depth and corrosion rate. Standard deviation in parentheses.

	SiO_2	Al_2O_3	Cr_2O_3	FeO*	MnO	MgO	NiO	CaO	Na_2O	K_2O	Total
EBS-2	33.47	13.14	1.25	31.03	0.38	1.98	1.26	1.31	1.60	0.62	86.04

Table F.2. Bulk chemical composition from the 304 SS corrosion layer developed from the ramped heating cycle (EBS-2)

	SiO_2	Al_2O_3	Cr_2O_3	FeO*	MnO	MgO	NiO	CaO	Na_2O	K_2O	Total
EBS-6	36.00	12.80	0.02	33.75	0.22	0.83	0.01	0.64	1.02	0.35	85.63

Table F.3. Bulk chemical composition (EMPA) from the low-carbon corrosion layer developed from the ramped heating cycle (EBS-6).